

AD-A106 065

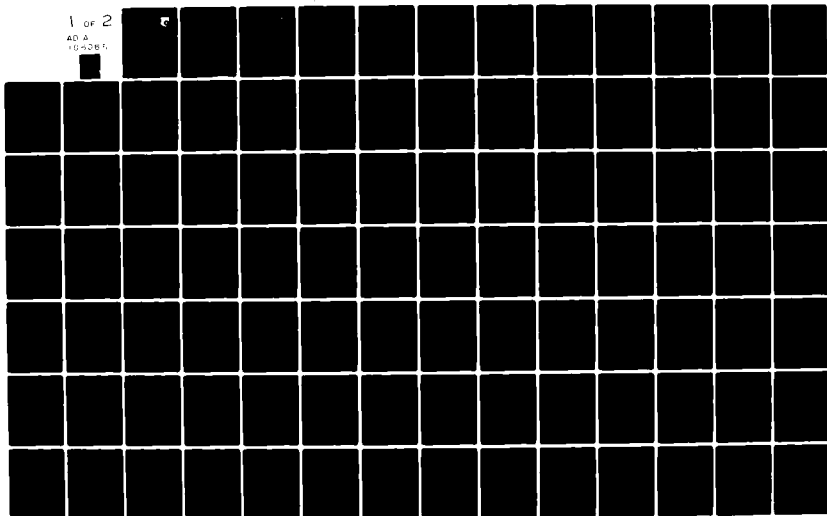
AIR FORCE WRIGHT AERONAUTICAL LABS WRIGHT-PATTERSON AFB OH F/G 20/4
EVALUATION OF USSAERO AND HABP COMPUTER CODES FOR AERODYNAMIC P--ETC(U)
SEP 81 J I FLAHERTY
AFWAL-TR-81-3035

UNCLASSIFIED

NL

1 of 2

AD-A
10-5287



AFWAL-TR-81-3035

LEVEL 1

2



EVALUATION OF USSAERO AND HABP COMPUTER CODES
FOR AERODYNAMIC PREDICTIONS FOR SLENDER BODIES

Jack I. Flaherty

High Speed Aero Performance Branch
Aeromechanics Division

DTIC
ELECTE
S OCT 23 1981 D
E

September 1981

Final Report for Period October 1979 - July 1980

Approved for public release; distribution unlimited.

FLIGHT DYNAMICS LABORATORY
AIR FORCE WRIGHT AERONAUTICAL LABORATORIES
AIR FORCE SYSTEMS COMMAND
WRIGHT-PATTERSON AIR FORCE BASE, OHIO 45433

81 10 22

AD A106065

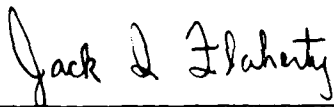
FILE COPY

NOTICE

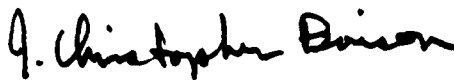
When Government drawings, specifications, or other data are used for any purpose other than in connection with a definitely related Government procurement operation, the United States Government thereby incurs no responsibility nor any obligation whatsoever; and the fact that the government may have formulated, furnished, or in any way supplied the said drawings, specifications, or other data, is not to be regarded by implication or otherwise as in any manner licensing the holder or any other person or corporation, or conveying any rights or permission to manufacture use, or sell any patented invention that may in any way be related thereto.

This report has been reviewed by the Office of Public Affairs (ASD/PA) and is releasable to the National Technical Information Service (NTIS). At NTIS, it will be available to the general public, including foreign nations.

This technical report has been reviewed and is approved for publication.

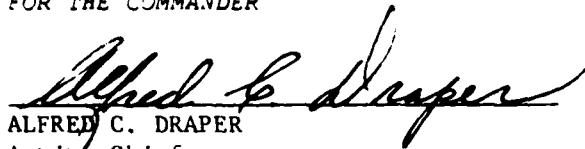


JACK I. FLAHERTY, Project Engineer
High Speed Aerodynamics Group



J. CHRISTOPHER BOISON
Chief, High Speed Aero Performance Branch
Aeromechanics Division

FOR THE COMMANDER



ALFRED C. DRAPER
Acting Chief
Aeromechanics Division

"If your address has changed, if you wish to be removed from our mailing list, or if the addressee is no longer employed by your organization please notify AFWAL/FIMG, W-PAFB, OH 45433 to help us maintain a current mailing list".

Copies of this report should not be returned unless return is required by security considerations, contractual obligations, or notice on a specific document.

SECURITY CLASSIFICATION OF THIS PAGE (When Data Entered)

REPORT DOCUMENTATION PAGE		READ INSTRUCTIONS BEFORE COMPLETING FORM
1. REPORT NUMBER 14 AFWAL-TR-81-3435	2. GOVT ACCESSION NO. AD-A406065	3. RECIPIENT'S CATALOG NUMBER 065
4. TITLE (and Subtitle) 6 EVALUATION OF USSAERO AND HABP COMPUTER CODES FOR AERODYNAMIC PREDICTIONS FOR SLENDER BODIES.		5. TYPE OF REPORT & PERIOD COVERED Final Report. October 1979-July 1980
7. AUTHOR(s) 10 Jack I. Flaherty		8. CONTRACT OR GRANT NUMBER(s) 17 071
9. PERFORMING ORGANIZATION NAME AND ADDRESS Aeromechanics Division Flight Dynamics Laboratory Air Force Wright Aeronautical Laboratories Wright-Patterson Air Force Base, Ohio 45433		10. PROGRAM ELEMENT, PROJECT, TASK AREA & WORK UNIT NUMBERS Program Element 62201F 2404-0730
11. CONTROLLING OFFICE NAME AND ADDRESS Flight Dynamics Laboratory Air Force Wright Aeronautical Laboratories Air Force Systems Command Wright-Patterson Air Force Base, Ohio 45433		12. REPORT DATE September 1981
14. MONITORING AGENCY NAME & ADDRESS (if different from Controlling Office)		13. NUMBER OF PAGES 104 12 205
		15. SECURITY CLASS (of this Report) UNCLASSIFIED
		15a. DECLASSIFICATION DOWNGRADING SCHEDULE N/A
16. DISTRIBUTION STATEMENT (of this Report) Approved for public release; distribution unlimited.		
17. DISTRIBUTION STATEMENT (of the abstract entered in Block 20, if different from Report)		
18. SUPPLEMENTARY NOTES		
19. KEY WORDS (Continue on reverse side if necessary and identify by block number) SLENDER BODIES MISSILES FLOW FIELDS SUBSONIC/SUPERSONIC AERODYNAMICS AERODYNAMIC PREDICTIONS USSAERO HABP		
20. ABSTRACT (Continue on reverse side if necessary and identify by block number) This study has been conducted to evaluate the merits and limitations of a subsonic and a supersonic analysis method used frequently in Government and Industry for predicting aerodynamic characteristics. Specifically the Unified Subsonic-Supersonic Aerodynamic Computer Program (USSAERO) was evaluated at Mach 0.4 for the subsonic case. The Supersonic-Hypersonic Arbitrary Body Program (HABP) was evaluated for the supersonic case beginning at a low Mach number of 1.50 and systematically increasing to Mach 4.63.		

392663

Model geometries have been restricted to simple axisymmetric ogive forebody cylindrical afterbody combinations to aid in the relative comparison of the method capabilities. For the supersonic comparisons a data base was selected that featured a wide variety of nose bluntness and fineness ratios to determine their impact on the analysis capabilities. Specific limitations of the methods are identified from comparisons with detailed body pressure coefficient data.

FOREWORD

This report describes an in-house assessment by the author for the High Speed Aero Performance Branch, Aeromechanics Division, Air Force Wright Aeronautical Laboratories (AFWAL/FIMG). The work was performed under Project 2404, "Aeromechanics," Task 24040730, "Aerodynamic Prediction Methods."

The evaluation reported herein used methodology developed by the Aerophysics Research Corporation, authored by F. A. Woodward and by the McDonnell Douglas Corporation, authored by A. E. Gentry, D. N. Smith, and W. R. Oliver. The experimental data necessary to evaluate these methodologies were extracted from technical reports published by the Air Force Armament Laboratory, authored by C. B. Butler, E. S. Sears, and S. G. Pallas; NASA, authored by E. J. Landrom; and AEDC, authored by D. C. Baker and D. E. Reichenau. The evaluation reported herein was conducted between October 1979 and July 1980.

Accession For	
NTIS GRA&I	<input checked="" type="checkbox"/>
DTIC TAB	<input type="checkbox"/>
Unannounced	<input type="checkbox"/>
Justification	
By	
Distribution/	
Availability Codes	
Dist	Avail and/or Special
A	

TABLE OF CONTENTS

SECTION	PAGE
I INTRODUCTION	1
II MODEL DESCRIPTIONS	2
1. N2B1 (from MX tests)	2
2. CAC and BNC (from NASA tests)	2
3. AFATL Models	3
III METHODOLOGY OVERVIEW	4
1. Unified Subsonic Supersonic Aerodynamics Program (USSAERO)	4
2. Supersonic Hypersonic Arbitrary Body Program (HABP)	5
a. Newtonian Compression Method	7
b. Approximate Cone Compression Method	7
c. Modified Dahlem/Buck Compression Method	8
d. Newtonian Expansion Method	9
e. Prandtl-Meyer Expansion Method	9
f. Van Dyke Unified Expansion Method	10
IV COMPARISONS OF ANALYSIS WITH EXPERIMENT	11
1. USSAERO - MX Data	11
2. HABP - NASA Pressures	13
3. HABP - AFATL Force and Moments	15
V CONCLUSIONS	17
APPENDIX DETAILED FORMULATION OF METHODS	19
1. USSAERO/Distributed Sources	19
2. HABP/Hammitt-Murthy	21
3. HABP-Prandtl-Meyer Expansion	25
REFERENCES	28

PRECEDING PAGE BLANK-NOT FILMED

LIST OF ILLUSTRATIONS

FIGURE		PAGE
1	Model Geometry and Pressure Orifice Locations for USSAERO Comparisons	29
	(a) Model Overall Dimensions	29
	(b) Ogive Nose Details	29
	(c) Orifice Locations	30
2	Model Geometries and Pressure Orifice Locations for HABP Pressure Prediction Comparisons	31
3	Model Geometries for HABP Force and Moment Comparisons	32
4	Axis and Coefficient Nomenclature	33
5	Comparison of USSAERO with Experiment for a Typical Ogive Nose Geometry	34
6	Effect of Adding an Afterbody on the USSAERO Comparisons with Experiment	35
7	Comparison of Pressure Coefficient Data with the HABP Analytical Results. Effects of Mach Number and Nose Bluntness, $\alpha = -4$ Degrees.	36
	(a) $X/L = 0.075$ to 0.225	36
	(b) $X/L = 0.325$ to 0.475	37
	(c) $X/L = 0.575$ to 0.775	38
	(d) $X/L = 0.875$ to 0.975	39
8	Integrated HABP Comparisons with Experiment for Distributed Local Force and Moment Results, $\alpha = -4$ Degrees	40
9	HABP Pressure Comparisons at $\alpha = 0$ Degrees	41
	(a) $X/L = 0.075$ to 0.225	41
	(b) $X/L = 0.325$ to 0.475	42
	(c) $X/L = 0.575$ to 0.775	43
	(d) $X/L = 0.875$ to 0.975	44
10	Integrated HABP Local Force and Moment Distribution, $\alpha = 0$ Degrees	45
11	HABP Pressure Comparisons for $\alpha = 4$ Degrees	46
	(a) $X/L = 0.075$ to 0.225	46
	(b) $X/L = 0.325$ to 0.475	47
	(c) $X/L = 0.575$ to 0.775	48
	(d) $X/L = 0.875$ to 0.975	49
12	Integrated HABP Local Force and Moment Distribution, $\alpha = 4$ Degrees	50
13	HABP Pressure Prediction Comparisons at $\alpha = 8$ Degrees	51
	(a) $X/L = 0.075$ to 0.225	51
	(b) $X/L = 0.325$ to 0.475	52
	(c) $X/L = 0.575$ to 0.775	53
	(d) $X/L = 0.875$ to 0.975	54

LIST OF ILLUSTRATIONS (CONTINUED)

FIGURE		PAGE
14	Integrated HABP Local Force and Moment Distribution, Alpha = 8 Degrees.	55
15	HABP Pressure Prediction Comparisons at Alpha = 12 Degrees	56
	(a) $X/L = 0.075$ to 0.225	56
	(b) $X/L = 0.325$ to 0.475	57
	(c) $X/L = 0.575$ to 0.775	58
	(d) $X/L = 0.875$ to 0.975	59
16	Integrated HABP Local Force and Moment Distribution, Alpha = 12 Degrees	60
17	HABP Pressure Comparisons at Alpha = 16 Degrees	61
	(a) $X/L = 0.075$ to 0.225	61
	(b) $X/L = 0.325$ to 0.475	62
	(c) $X/L = 0.575$ to 0.775	63
	(d) $X/L = 0.875$ to 0.975	64
18	Integrated HABP Local Force and Moment Distribution, Alpha = 16 Degrees	65
19	Total Force and Moment HABP Comparisons with Experiment at Various Angles of Attack. Effect of Mach Number and Nose Bluntness	66
20	Effect of Nose Bluntness and Mach Number on Total Force and Moment HABP Comparisons. Nose Fineness Ratio = 1.0	67
	(a) $R_N/R_B = 0.0$ and 1.0 , $M = 1.5$ and 2.0	67
	(b) $R_N/R_B = 0.0$ and 1.0 , $M = 3.0$ and 4.0	68
21	HABP Force and Moment Comparisons for the 2.0 Nose Fineness Ratio Geometry. Effects of Nose Bluntness and Mach Number	69
	(a) $R_N/R_B = 0.0$ and 0.25 , $M = 1.5$ and 2.0	69
	(b) $R_N/R_B = 0.0$ and 0.25 , $M = 4.0$	70
	(c) $R_N/R_B = 0.0$ and 0.50 , $M = 1.5$ and 2.0	71
	(d) $R_N/R_B = 0.0$ and 0.50 , $M = 4.0$	72
	(e) $R_N/R_B = 0.0$ and 0.75 , $M = 1.5$ and 2.0	73
	(f) $R_N/R_B = 0.0$ and 0.75 , $M = 4.0$	74
22	HABP Force and Moment Comparisons for Nose Fineness Ratio = 2.25	75
	(a) $R_N/R_B = 0.0$ and 0.375 , $M = 1.5$ and 2.0	75
	(b) $R_N/R_B = 0.0$ and 0.375 , $M = 3.0$ and 4.0	76
	(c) $R_N/R_B = 0.0$ and 0.575 , $M = 1.5$ and 2.0	77
	(d) $R_N/R_B = 0.0$ and 0.575 , $M = 3.0$ and 4.0	78

LIST OF ILLUSTRATIONS (CONCLUDED)

FIGURE		PAGE
23	HABP Force and Moment Comparisons for the 2.5 Nose Fineness Ratio Geometry. Sharp Nose	79
24	HABP Force and Moment Comparisons for the Power Series Nose Geometry.	80
	(a) Mach = 1.5 and 3.0	80
	(b) Mach 4.0	81
25	HABP Force and Moment Comparisons for the 3.0 Fineness Ratio Nose	82
	(a) $R_N/R_B = 0.0$ and 0.25 , $M = 1.5$ and 2.0	82
	(b) $R_N/R_B = 0.0$ and 0.25 , $M = 3.0$ and 4.0	83
	(c) $R_N/R_B = 0.0$ and 0.50 , $M = 1.5$ and 2.0	84
	(d) $R_N/R_B = 0.0$ and 0.50 , $M = 3.0$ and 4.0	85
	(e) $R_N/R_B = 0.0$ and 0.75 , $M = 1.5$ and 2.0	86
	(f) $R_N/R_B = 0.0$ and 0.75 , $M = 3.0$ and 4.0	87
26	HABP Force and Moment Comparisons for the 4.0 Fineness Ratio Nose	88
	(a) $R_N/R_B = 0.0$ and 0.25 , $M = 1.5$ and 2.0	88
	(b) $R_N/R_B = 0.0$ and 0.25 , $M = 3.0$ and 4.0	89
	(c) $R_N/R_B = 0.0$ and 0.50 , $M = 1.5$ and 2.0	90
	(d) $R_N/R_B = 0.0$ and 0.50 , $M = 3.0$ and 4.0	91
	(e) $R_N/R_B = 0.0$ and 0.75 , $M = 1.5$ and 2.0	92
	(f) $R_N/R_B = 0.0$ and 0.75 , $M = 3.0$ and 4.0	93

LIST OF SYMBOLS

A_b	Model base area, reference area
A_p	Model planform area
a	(a) Tangent of body inclination angle δ ; (b) Lower transition limit of the unified similarity parameter $M_\infty \sin \delta_c$ (Equation A-20)
b	(a) Wing panel span (b) Upper transition limit of the unified similarity parameter (Equation A-20)
C_A	Forebody axial force coefficient, (forebody axial force)/ $q_\infty A_b$
C_{d_n}	Crossflow drag coefficient
C_N	Normal force coefficient, (normal force)/ $q_\infty A_b$
C_M	Pitching moment coefficient (pitching moment)/ $q_\infty A D$
C_p	Pressure coefficient $\frac{P - P_\infty}{q_\infty}$
D	Model base diameter, reference length
h	Radius connecting a point source within a body quadrilateral area with a point in the field
L	Model length
M	Mach number
m	Body panel edge slope
P	Pressure
q	Dynamic pressure, $\frac{\gamma}{2} \rho M^2$
Re	Reynolds number per unit length, $\rho V/\mu$
r	Body radius (Figure 2)
R_N	Model spherical nose radius
R_B	Model base radius
T	Temperature

LIST OF SYMBOLS (CONCLUDED)

\bar{V}	Local velocity vector with components V_x , V_y and V_z in the model coordinate system
X, Y, Z	Cartesian coordinate system with X parallel to the model axis and origin at model nose (Figure 4)
x, y, z	Cartesian coordinates relative to a panel corner point with y parallel to panel leading edge (Figure 4)
α, β, ϕ	Angles of attack, sideslip, and roll, respectively
β	$M_\infty^2 - 1$
γ	Ratio of specific heats
δ	Surface impact angle relative to freestream
η	Angle between surface normal vector and freestream
θ	Circumferential location of pressure orifices
θ_s	Shock angle
μ	(a) Mach angle (b) Absolute viscosity
ν	Prandtl-Meyer angle
η	Crossflow drag proportionality factor
ρ	Density
ψ	Perturbation velocity potential (Equation 3)
ξ, η	Point source coordinates relative to a coordinate system lying in the plane of the panel

SUBSCRIPTS

∞	Freestream conditions
s	Conditions just downstream of shock wave
c	Conditions on surface
T	Total conditions
i	(a) Index of panel control point (b) Iteration value

NOTE: Other symbols used as parameters in equations are defined in the text where they are used.

SECTION I

INTRODUCTION

An engineer is often faced with a difficult task in selecting the analysis method that will provide good and consistent results. One of the things that complicates the selection is model geometry complexities, such as irregular body shapes and control surfaces that lead to complex flow fields beyond the analysis capabilities of the more simplified analytical procedures. A relative comparison between analytical methods should be made with simple geometries so that under these relaxed conditions comparisons between various methods might lead to some insights into their relative capabilities and restrictions. Thus for the present study, slender ogive/cylindrical body combinations without control surfaces, nozzles, etc., were selected to study the relative merits of analysis methods that the Flight Dynamics Laboratory often uses to analyze more complex configurations. Low supersonic Mach numbers were selected for this study as well as a subsonic case because experience has shown that these two cases are the most difficult to predict. Selected for evaluation in this study were the Unified Subsonic-Supersonic Aerodynamic Computer Program (USSAERO) of Reference 1 and the Supersonic-Hypersonic Arbitrary Body Program (HABP) of Reference 2.

The objective of the present study is to take a detailed look at the capabilities of the above programs for predicting overall aerodynamic characteristics. Such things as detailed pressure coefficient predictions around the body are compared with the experimental data to determine where the analysis would benefit from improvement. Configuration geometry variables such as nose bluntness and fineness ratio are varied in the supersonic case to study their impact on the analysis. Comparisons are made at a subsonic Mach number of 0.4 and supersonic Mach numbers beginning with a low value of 1.50 and progressively increasing to 4.6. The comparisons in the present study have been restricted to the merits of the inviscid methods because inclusion of the viscous analysis techniques would have complicated the evaluation and perhaps led to confusion in interpreting the results contained herein.

SECTION II

MODEL DESCRIPTIONS

1. N2B1 (FROM MX TESTS)

A large number of missile configurations were used in the present investigation for the data/theory comparisons. Complete descriptions of these models and their instrumentation can be found in References 3, 4, and 5. A brief description is repeated here for completeness. For the subsonic comparisons, the configuration was the N2B1 configuration (Reference 3). The model had an ogive nose with a fineness ratio, L_N/D , of 2.545 fineness ratio and an aft body of 7.754 fineness ratio for a combined fineness ratio of 10.3. The bluntness ratio R_N/R_B , was .03. Figure 1 shows a sketch of the model geometry and pressure orifice locations.

2. CAC AND BNC (FROM NASA TESTS)

For the supersonic pressure prediction comparisons, two models from Reference 4 were selected. They are the circular-arc-cylinder (designated CAC in the present study) model and the blunt-nose-cylinder (designated BNC) model, with a bluntness ratio of 0.17. The geometrical description of these two configurations are as follows:

Circular-Arc-Cylinder (CAC)

$$r/L = \sqrt{(1.3125)^2 + (X/L)(0.9 - X/L)} - 1.3125 \quad (0 < X/L \leq 0.45)$$

$$r/L = 0.075 \quad (0.45 \leq X/L < 1.0)$$

Blunt-Nose-Cylinder (BNC)

$$r/L = 0.1118 (X/L)^{1/2} \quad (0 < X/L \leq 0.45)$$

$$r/L = 0.075 \quad (0.45 < X/L \leq 1.0)$$

A sketch of these two models showing model orifice locations is seen in Figure 2.

3. AFATL MODELS

For the force/moment comparisons at supersonic speeds a large selection of configurations were available from tests conducted by the Air Force Armament Test Laboratory (AFATL) as reported in Reference 5. The models selected for the present comparisons consisted of 20 nose geometries with fineness ratios varying from 1 to 4 and one aft body with a fineness ratio of 10. Bluntness ratios (R_N/R_B) varied from sharp 0.0 to 1.0. The geometrical description and designations of the models are presented in Figure 3.

SECTION III

METHODOLOGY OVERVIEW

1. UNIFIED SUBSONIC-SUPERSONIC AERODYNAMICS PROGRAM (USSAERO)

A complete description of the theory and computer program may be obtained from Reference 1. Presented here is a brief summary of the general theory used for body alone applications. Axis and coefficient nomenclature is presented in Figure 4.

The configuration surface is subdivided into a large number of panels, each of which contains an aerodynamic singularity distribution. A constant source distribution per unit area is used on each body panel. The position of the source within each panel relative to a coordinate system lying in the plane of the panel is denoted by $(\xi, \eta, 0)$. The radius connecting an arbitrarily located source within the quadrilateral with a point in the flow field $P(X, Y, Z)$ is given by

$$h = [(x - \xi)^2 + (y - \eta)^2 + z^2]^{1/2} \quad (1)$$

for incompressible flow applications. Details for the compressible flow case can be found in Reference 1 and will not be summarized here. The general approach, however, is to apply Gothert's rule to the incompressible velocity components described in this section. The incremental perturbation potential arising from an increment of area $(d\xi d\eta)$ located at the source point (ξ, η) is

$$d\phi = \frac{-1}{4\pi h} d\xi d\eta \quad (2)$$

Thus

$$\phi = \frac{-1}{4\pi} \iint_A \frac{d\xi d\eta}{[(x - \xi)^2 + (y - \eta)^2 + z^2]^{1/2}} \quad (3)$$

The general approach of the method is to calculate the velocity components at the centroid of each panel by partial differentiation of the potential

defined in Equation 3 with respect to x, y, z . The pressure coefficient at the centroid of the j th panel is then calculated as follows

$$C_{p_j} = 1 - q_j^2 \quad (4)$$

where

$$q_j^2 = (V_{x_j} + \cos\alpha)^2 + V_{y_j}^2 + (V_{z_j} + \sin\alpha)^2$$

The total force and moment coefficients are then obtained by summing the products of the pressure coefficient over the entire body geometry. Details of the mathematics required to obtain the velocity components on each of the panels are shown for the incompressible case in Section I of the Appendix.

2. SUPERSONIC-HYPERSONIC ARBITRARY BODY PROGRAM (HABP)

The Mark IV Supersonic-Hypersonic Arbitrary Body Program (HABP) is a computer program that is capable of calculating the aerodynamic characteristics of arbitrary complex three-dimensional shapes. A complete description of the program and its various pressure coefficient options is provided in Reference 2. Although the program is most accurate at hypersonic speeds, its capabilities have been extended down to supersonic speeds by use of slender body theory and empirical techniques that are described in this section. As with USSAERO the body is described by a large number of panels. Element area, centroid, and a unit normal are then calculated from the four points describing the quadrilateral surface. Before the program calculates the pressure on each surface element, it checks to see if the element is facing the flow (in an impact region). This is done by checking if the sign of the angle η between the freestream velocity and the outward directed unit normal vector to the surface is positive. If the sign is negative, the selected expansion method is used. The unit outward directed normal on each of the surface elements is

$$\vec{n} = n_x \vec{i} + n_y \vec{j} + n_z \vec{k} \quad (5)$$

where n_x , n_y , and n_z are the direction cosines of the surface element normal necessary to obtain the components of the force on each quadrilateral. The mathematical details for obtaining these direction cosines is outlined in Reference 2.

A common parameter necessary to all of the inviscid methods in HABP is the angle δ that a tangent to the element makes with the freestream velocity. Once the unit outward directed normal expressed in Equation 5 is obtained on a particular quadrilateral, the tangent angle is determined simply as follows:

$$\delta = \frac{\pi}{2} - \eta \quad (6)$$

where

$$\eta = \cos^{-1} \left(\frac{\vec{n} \cdot \vec{V}_{\infty}}{|\vec{V}_{\infty}|} \right)$$

There are 15 inviscid compression pressure methods and nine expansion pressure methods available as an option to HABP users. The selection of the proper method in a given application depends upon the vehicle component and flight condition and is selected on the basis of knowledge and experience in the use of each method.

For the present study, three combinations of compression/expansion inviscid pressure methods have been selected for comparison with data on the lower end of the Mach number range (Mach 1.5 to 4.63). They are as follows:

Compression Methods

- 1 - Newtonian
- 5 - Approximate Cone (Slender Body plus Hammitt-Murthy)
- 14 - Modified Dahlem/Buck

Expansion Methods

- 1 - Newtonian ($C_p = 0.$)
- 3 - Prandtl-Meyer
- 5 - Van Dyke Unified

In the comparisons with the data, a combination of a compression method and an expansion method is designated by a two-number sequence. The first number represents the impact method and the second number the expansion method.

a. Newtonian Compression Method

The Newtonian theory on the impact surfaces gives the pressure coefficient as a direct function of the tangent angle δ (Equation 6) as follows

$$C_p = K \sin^2 \delta \quad (7)$$

where

$$K = C_{p_{\max}} = \frac{\gamma + 3}{\gamma + 1} \left[1 - \frac{2}{\gamma + 3} M_\infty^{-2} \right]$$

b. Approximate Cone Compression Method

This method is used in HABP to improve the low Mach number pressure coefficient prediction capabilities. Three approximate cone techniques are used. Specifically, second-order slender body theory (Reference 6) is used in the low supersonic range and the technique described in Reference 7 is used in the higher supersonic range. In addition, an empirical tangent cone method described in Reference 2 is used for large incidences where the flow becomes detached.

The second-order slender body solution of Reference 6 is used whenever $(M_\infty \sin \delta) < a$ where $a = 0.2$ for freestream Mach numbers less than 3.0 and $a = 0.3$ for larger freestream Mach numbers. Then from Reference 6 the pressure coefficient is a function of δ and M_∞ and is determined as follows:

$$C_{p_{\text{cone}}(2\text{nd order})} = \tan^2 \delta \{ (2\xi - 1.0) + \tan^2 \delta [3(\beta\xi)^2 - (5M_\infty^2 - 1)\xi + A] \} \quad (8)$$

where δ is determined as in Equation 6 and

$$\xi = \ln \frac{2}{\beta \tan \beta}$$

$$\beta = \sqrt{M_\infty^2 - 1}$$

$$A = 3.25M_\infty^2 + 0.5 + (\gamma + 1) \left(\frac{M_\infty}{\beta} \right)^2$$

For the higher Mach number the Hammitt-Murthy solution of Reference 7 is used whenever $(M_\infty \sin \delta) > 0.325$. In this method the shock cone angle, θ_s , and surface Mach number, M_c , is first determined. Results from Reference 8 are then used to obtain the pressure ratio and local Mach number behind the shock. Isentropic relations between the shock and body are then used to obtain the pressure ratio on the surface, P_c/P_∞ . The pressure coefficient is then found as follows:

$$C_{p_{\text{cone}}(\text{Hammitt-Murthy})} = \frac{(P_c/P_\infty)_{\text{HM}} - 1.0}{1/2 \gamma M_\infty^2} \quad (9)$$

The mathematical details of the Hammitt-Murthy solution are presented in Section 2 of the Appendix. If the flow is detached a different procedure is used to obtain θ_s . Details are also found in Section 2 of the Appendix. If $(M_\infty \sin \delta)$ is between 0.3 and 0.325, a transition solution between the second-order results and the Hammitt-Murthy solution is determined. The details are found in Section 2 of the Appendix.

c. Modified Dahlem/Buck Compression Method

For high Mach number (≥ 20) this method uses an empirical relationship that approximates tangent-cone pressures at low impact angles and approaches Newtonian values at high impact angles. The relationship is

$$C_p = K \sin^2 \delta, \quad M_\infty \geq 20 \quad (10)$$

where

$$K = \left[\frac{1.0}{(\sin 4\delta)^{0.75}} + 1.0 \right] \quad \text{for } \delta \leq 22.5^\circ$$

and

$$= 2.0 \quad \text{for } \delta > 22.5^\circ$$

For small values of δ the upper limit of the bracketed term is not allowed to exceed 5.0. The method is extended to lower Mach numbers by assuming that the empirical pressure coefficient of Equation 10 varies with Mach number in the same manner as the pressure coefficient for a right circular cone.

This gives

$$C_{P_{MDB}} = C_{P_{(Eq\ 10)}} \left[\frac{C_{P_{cone(M_\infty = 20)}}}{C_{P_{cone(M_\infty = 20)}}} \right] \quad (11)$$

The term in brackets in Equation 11 was determined empirically in Reference 9 to be

$$\frac{C_{P_{cone(M_\infty < 20)}}}{C_{P_{cone(M_\infty = 20)}}} = \frac{a}{\delta^\eta}, \quad \delta \text{ in degrees} \quad (12)$$

where

$$a = (6.0 - 0.3M_\infty) + \sin \left(\frac{\ln(M_\infty) - 0.588\pi}{1.2} \right)$$

and

$$\eta = 1.15 + 0.5 \sin \left(\frac{\ln(M_\infty) - 0.916\pi}{3.29} \right)$$

d. Newtonian Expansion Method

This method substitutes a lower limit on the expansion pressure equal to the freestream value. Thus, for $\delta < 0$ the pressure coefficient, C_p , is set equal to zero.

e. Prandtl-Meyer Expansion Method

This method utilizes the relationships of Reference 8 to expand the freestream Mach number to a surface Mach number, M_c . With M_c thus obtained the familiar isentropic relationships of Reference 8 are then

used to calculate the ratio of the surface pressure to total pressure.
The pressure coefficient is then calculated as follows:

$$C_{P_{PM}} = \frac{\frac{P_c}{P_\infty} - 1.0}{\frac{\gamma}{2} M_\infty^2} = \frac{\frac{P_c/P_T}{P_\infty/P_T} - 1.0}{\frac{\gamma}{2} M_\infty^2} \quad (13)$$

$$= \frac{Z^{\gamma/(\gamma-1)} - 1.0}{\frac{\gamma}{2} M_\infty^2} \quad (14)$$

where

$$Z = \frac{(1 + \frac{\gamma-1}{2} M_\infty^2)}{(1 + \frac{\gamma-1}{2} M_c^2)}$$

Details of the expansion process are found in Section 3 of the Appendix.

f. Van Dyke Unified Expansion Method

This method for expansion flow is derived in Reference 10.

The results are

$$C_{P_{VAN DYKE}} = \frac{2\delta^2}{\gamma H^2} \left[\left(1.0 - \frac{\gamma-1}{2} H \right)^{2\gamma/(\gamma-1)} - 1.0 \right] \text{ for } H > 2/(\gamma-1) \quad (15)$$

where

$$H = (\sqrt{M_\infty^2 - 1.0})\delta$$

and

$$C_{P_{VAN DYKE}} = -\frac{1}{M_\infty^2} \text{ for } H < 2/(\gamma-1)$$

SECTION IV

COMPARISONS OF THE ANALYSIS WITH EXPERIMENT

It should be noted that, in all of the comparisons to follow, base pressure has been subtracted out and skin friction has not been included in the USSAERO comparisons or the integrated pressure HABP results.

1. USSAERO MX DATA

Selected portions of the data base from Reference 3 were utilized to compare the USSAERO capability to predict the detailed pressure coefficients and forces on typical ogive nose shapes. The comparisons of the analysis and experiment are described here for the nose geometry shown in Figure 1 and for Mach 0.4 freestream flow.

Figure 5 shows the comparison of USSAERO with measured pressure coefficients at 20 degrees angle of attack and the total integrated normal coefficients for an angle of attack range from 0 to 20 degrees. For model stations between $X/D = 0.46$ and 1.84 the theory compares very well with the measured results for pressure coefficients. On the remaining 20 percent of the nose, however, USSAERO predicted negative pressure coefficients on the windward meridians and positive pressure coefficients on the leeside. This results in the prediction of large negative loads on the aft end of the nose with a resulting under-prediction of the total normal force coefficient as evidenced on the right in Figure 5. Included for comparison purposes is the simple expression from Reference 11 that relates the normal force to angle of attack and the crossflow drag coefficient. As seen from the figure, the inclusion of the crossflow drag component improves the correlations. Analytical studies using a source distribution approach similar to Woodward's method (References 12, 13) experienced the same problem on short axisymmetric bodies. These studies attributed the source of the problem to the lack of proper modeling of the body wake. The correction used in these studies was to model the base streamlines as part of the body description. This was done by extending the body and then closing it with a wake of the same shape as the nose.

In the present study, the effect of extending the body downstream without closure was made to determine its effect on the Woodward analysis. Pressure coefficient data was available from Reference 3 for cylindrical body extensions to the nose geometry of Figure 1. The nose had a fineness ratio of $L_{\text{NOSE}}/D = 2.55$. Cylindrical body extensions of 0.25 diameters and 2.25 diameters were added to the N2 nose producing two additional configurations with total fineness ratios of 2.8 and 4.8, respectively. An additional comparison was made with the N2 with a 7.75 diameter long afterbody added to produce a configuration with a total fineness ratio of 10.3. The result seen on the left side of Figure 6 shows the effect of the small aft body extension (fineness ratio = 2.8) and the larger extension (fineness ratio = 4.8) on the Woodward predictions at the nose/body juncture ($X/D = 2.3$) and on the extended cylindrical body. As noted in the figure the addition of the 2.25 body extension corrected the negative load prediction at the base of the N2 nose (denoted as the nose/body juncture in this figure). In implementing this procedure another problem in the Woodward analysis became apparent. This can be seen on the left side of Figure 6 for the pressure coefficient comparisons on the body. Note that while the angle of attack is 20 degrees the Woodward analysis predicts a nearly symmetrical pressure distribution on the extended nose/body combination of $L/D = 4.8$; thus resulting in zero normal force on the cylinder. This problem can most likely be attributed to the absence of a solution to the 2-D Laplace equation in the Y, Z crossflow plane in the Woodward analysis. Without this addition one might not expect good agreement with data at angles of attack greater than about four degrees.

This is indeed the case as evidenced on the right of Figure 6 where lack of agreement for angles of attack above four degrees become significant for longer bodies as the comparisons with the 10.3 fineness ratio configuration show.

Thus, the present study shows that (1) for a small fineness ratio nose, extending the nose downstream one or two diameters will correct the negative loads on the aft end, however, (2) when attempting to predict the loads on nose/body combinations, the absence of a crossflow

solution in the subsonic Woodward analysis at low Mach numbers may result in significant errors in predicting the normal force coefficient at angles of attack above four degrees (especially for large fineness ratio nose/body combinations). No additional analysis was made to determine if closing the base with an extension of the same shape as the nose, such as done in References 12 and 13, would improve the correlations.

2. HABP-NASA PRESSURES

The remaining studies of this report compare supersonic predictions using various combinations of the HABP compression and expansion methods outlined in Section III and in the Appendix. The comparisons are made for the two nose/body combinations shown in Figure 2 and for the large variety of nose shapes shown in Figure 3. Results are presented over a number range between 1.63 to 4.63 for the nose/body combinations and consist of comparing the predictions with the detailed pressure coefficient data from Reference 4. For the various nose shapes seen in Figure 3, the comparisons consist of total force and moment comparisons. This data was obtained from Reference 5 at Mach numbers from 1.5 to 4.0.

The particular HABP compression/expansion prediction combination used in the comparisons are identified in all of the remaining figures as a two-digit number (c, e) where c denotes the compression method and e the expansion method. The following numbers have been selected to identify these selections.

Compression

c = 1	Newtonian
c = 5	Approximate Cone
c = 14	Modified Dahlem/Buck

Expansion

e = 1	Newtonian ($C_p = 0$)
e = 3	Prandtl-Meyer
e = 5	Van Dyke Unified

Comparisons for the pressure coefficient predictions are presented in Figures 7 through 19. The solid and dashed lines show the theoretical predictions. The circles represent the experimental data from Reference 4.

To be consistent with the data format in Reference 4 the nomenclature of the circumferential location, θ , differs from that presented in Figures 5 and 6 of this report. The nomenclature of θ in Figures 7 through 17 is as shown in Figure 2. $\theta = 0^\circ$ is the centerline on the upper surface and $\theta = 180^\circ$ is the lower surface centerline.

Each figure is arranged to show relative effects of Mach number and nose bluntness at a selected angle of attack for a particular X/L location corresponding to the instrumentation stations in Figure 2. For example, in Figure 7a comparisons between the blunt and sharp model are shown on the left of the figure for Mach 1.6 while the same comparisons are made on the right for Mach 4.63. All of these comparisons are made for X/L values from 0.075 to 0.225. Identical comparisons are shown for the remaining axial stations in Figures 7b through 7d. All comparisons in Figure 7 are for α equal to -4 degrees. Figure 8 shows the distributed loads obtained by integrating the experimental and predicted pressure distributions from Figure 7 along the body. Figures 9 through 18 repeat this pattern for the remaining angles of attack through $\alpha = 16$ degrees. Finally, the total integrated loads at each of the angles of attack are shown in Figure 19.

A careful study of the pressure comparisons show that methods (5,3) and (14,5) are generally more accurate on the nose (X/L between 0.125 and 0.425) while method (1,1) is in better agreement on the cylindrical aft body. On the cylinder the expansion prediction $C_p=0$ is in general agreement with the data. The overall correlations improve with increasing Mach number. The resulting total force and moment characteristics as shown in Figure 19 reflect that method (1,1) provides better agreement with C_N and C_M because they are more influenced by pressure prediction accuracy on the cylinder. The remaining two methods have more accuracy for the C_A predictions since the axial force is more influenced by the nose pressure prediction accuracy. Figure 19 shows that methods (5,3) and (14,5) were more accurate in predicting C_A for the sharp model than for the blunt model. However, since these comparisons are only for one bluntness ratio ($R_N/R_B = 0.17$) and one fineness ratio ($L_N/D = 3.2$), an expanded data base comparison featuring variations in these variables will be presented in the remaining paragraphs.

3. HABP-AFATL FORCE AND MOMENTS

The data base from Reference 5 was selected for the geometrical comparisons because of the large selection of nose bluntness and fineness ratios available as seen from Figure 3. The unit Reynolds number for this data was $R_e/ft = 1.8 \times 10^6$ for all Mach numbers. The boundary layer was assumed to be turbulent and the reference enthalpy skin friction option was selected in the remaining HABP predictions. The predicted skin friction coefficient variation was about the same for all of the configurations analyzed and varied nominally from 0.04 at Mach 1.5 to 0.03 at Mach 4.0. Since the skin friction coefficient was nearly the same for each of the nose shapes at a particular Mach number, the relative comparisons of predicted C_A are sensitive to the inviscid method selected. The comparisons in the following figures are made from the experimental data with the base pressure drag subtracted. Since most of the ogive nose surface experiences a compression in the angle of attack range from 0 to 16 degrees, the remainder of the study focused on the HABP compression methods. The Newtonian expansion method ($C_p = 0$) was arbitrarily selected for each combination of compression methods and remained fixed for all of the geometrical comparisons.

The remaining force and moment comparisons are shown in Figures 20 to 26. Each figure is arranged to show the effect of nose bluntness and Mach number for a particular fineness ratio. For example, Figure 20a shows comparison between the sharp nose and a nose with bluntness ratio of 1.0. The nose fineness ratio is also 1.0. Comparisons on the left are for Mach 1.50 while those on the right of the figure are for Mach 2.0. Figure 20b continues these comparisons for Mach 3.0 and Mach 4.0. The remaining figures follow the same pattern of presentation for successively increasing fineness ratios. For the higher fineness ratio nose shapes, a larger selection of nose bluntness data was available for comparison: generally ranging between $R_N/R_B = 0.25$ to 0.75.

A study of the comparisons shows that each of the compression methods has satisfactory agreement with the C_A data for bluntness ratios less than 0.4, even down to Mach numbers as low as 1.5. For $R_N/R_B = 1.0$ and 0.75

each of the compression methods generally over-predicted the axial force at all Mach numbers. For smaller bluntness ratios, this was not always true, especially with the Newtonian compression method. With one exception, Mach 1.5, each of the three methods under-predicted axial force for the sharp nose models at all Mach numbers. By comparing the sharp model results for progressively higher fineness, one can note a slight improvement in C_A predictions as fineness ratio increases. The bluntness ratio is the dominant geometrical variable affecting the analysis capability, and the agreement improves for all of the methods as the Mach number increases. The Newtonian compression method ($C = 1$) was the most accurate in predicting the normal force and pitching moment coefficients over the entire Mach number range; this was the same result obtained in the nose/body configuration studies (Figures 7 through 19).

SECTION V

CONCLUSIONS

An evaluation has been made on two aerodynamic analysis programs that one might use to predict the aerodynamic characteristics of simple slender bodies without complexities such as control surfaces, nozzles, etc. Specifically, in the subsonic range USSAERO (Reference 1) which subdivides the body into a large number of panels with a constant source distribution on each panel, was selected for evaluation. In the low supersonic regime ($M = 1.5$ to 4.63) three impact methods and three shadow methods, available in the Supersonic-Hypersonic Arbitrary Body Program, referred to as HABP, were studied. From this study a number of conclusions were reached and are presented as follows:

The USSAERO program gave satisfactory subsonic predictions on the ogive nose geometries for angles of attack less than eight degrees. For higher angles of attack, two problems were encountered. The first problem was a large negative load predicted on the aft end of the nose. This was a result of negative pressure coefficients on the windward rays and positive pressure coefficients on the leeward rays being predicted. The problem was corrected by extending the nose 2.25 diameters downstream with a cylindrical afterbody. In implementing this procedure, a second problem in the USSAERO analysis became evident. The second problem was the prediction of zero normal loads on the cylindrical extensions even at angles of attack up to 20 degrees. This was a result of predicted symmetrical pressure distributions on the cylindrical extensions. It is felt that this is due to the 2D crossflow plane solution not being present in the subsonic USSAERO analysis.

Three compression and three expansion HABP prediction methods were evaluated from Mach 1.5 to Mach 4.63 for a large variety of ogive nose shapes. The primary variables were nose bluntness and fineness ratio. In addition comparisons were made for a nose/body combination of overall fineness ratio of 6.67 with both a sharp and blunt nose. The results for the nose/body combination showed that approximate cone and modified Dahlem/Buck compression predictions methods in conjunction with

Prandtl-Meyer and Van Dyke Unified expansion methods were more accurate than the Newtonian predictions for C_A due to the larger contribution of the nose on the predictions. On the other hand, the Newtonian methods were superior for the C_N and C_M predictions which are influenced more by the cylindrical afterbody than the nose.

Comparisons for a large variety of ogive nose shapes, with nose bluntness and fineness ratio being the primary variables, showed that nose bluntness was the significant geometrical variable that determined prediction accuracy. For bluntness ratios above $R_N/R_B = 0.4$ all of the methods over predicted C_A . The sharp nose exhibited slight sensitivity to nose fineness ratio in predicted C_A . The normal force coefficient, C_N , and the pitching moment coefficient, C_M , predictions were relatively insensitive to these geometrical variables.

APPENDIX

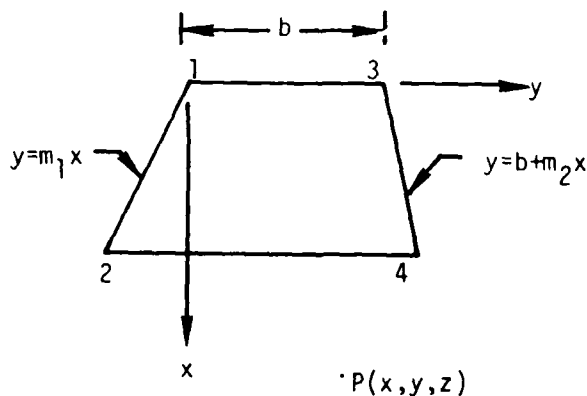
DETAILED FORMULATION OF METHODS

Some of the intermediate procedures necessary in obtaining the pressure coefficients in Section III are included here for completeness.

1. USSAERO/DISTRIBUTED SOURCES

As seen in Equation 4 the pressure coefficient acting at the centroid of each panel is determined by the components of velocity in the X, Y, and Z direction. These are obtained by the partial differentiation of the source potential defined in Equation 3 with respect to the x, y, and z coordinates referenced to the leading of each panel as shown in the following sketch. The resulting velocities are then transferred to the components in the X, Y, Z coordinate system.

To begin the procedure consider the geometry of each panel as defined by the following sketch



The velocity components in the x, y, z directions are obtained by differentiating Equation 3. The resulting expressions are:

$$\frac{V_x}{V_\infty} = \phi_x = \frac{1}{4\pi} \iint_A \frac{(x-\xi)d\xi d\eta}{[(x-\xi)^2 + (y-\eta)^2 + z^2]^{3/2}} \quad (A-1)$$

$$\frac{V_y}{V_\infty} = \phi_y = \frac{1}{4\pi} \iint_A \frac{(y-\eta)d\xi d\eta}{[(x-\xi)^2 + (y-\eta)^2 + z^2]^{3/2}} \quad (A-2)$$

$$\frac{V_z}{V_\infty} = \phi_z = \frac{1}{4\pi} \iint_A \frac{z d\xi d\eta}{[(x-\xi)^2 + (y-\eta)^2 + z^2]^{3/2}} \quad (A-3)$$

Complete details of the derivation may be found in Reference 1. However, the result for a typical corner is included here for completeness. With $a = \tan\delta$ (where δ is found as in Equation 6) and m_i = the body panel edge slope dy/dx , the three velocity components at each of the four corner points are determined as follows in the X, Y, Z coordinate system.

$$\left(\frac{V_x}{V_\infty}\right)_i = \frac{1.0}{4\pi(1+a^2)^{1/2}} [m_i G - H - aF], \quad i = 1 \text{ to } 4 \quad (A-4)$$

$$\left(\frac{V_y}{V_\infty}\right)_i = \frac{-G(1+a^2)^{1/2}}{4\pi}, \quad i = 1 \text{ to } 4 \quad (A-5)$$

$$\left(\frac{V_z}{V_\infty}\right)_i = \frac{1.0}{4\pi(1+a^2)^{1/2}} [F + a(m_i G - H)], \quad i = 1 \text{ to } 4 \quad (A-6)$$

where

$$F = \tan^{-1} \left(\frac{(z - ax)(x^2 + y^2 + z^2)^{1/2}}{-x(y - m_i x) - z(ay - m_i z)} \right)$$

$$G = \frac{1.0}{(1 + a^2 + m_i^2)^{1/2}} \sinh^{-1} \left(\frac{x + m_i y + az}{[(y - m_i x)^2 + (ay - m_i z)^2 + (z - ax)^2]^{1/2}} \right)$$

$$H = \sinh^{-1} \left(\frac{y}{(x^2 + z^2)^{1/2}} \right)$$

The velocity components at each of the four corner points are found by applying the above formulas with the origin shifted to the corner under consideration and using the appropriate edge slope. The influence of the panel is obtained by summing the influences of the four corners and applying the resulting velocity to the centroid of the panel. Thus, for the j th panel

$$V_{X_j} = (V_{X_1} - V_{X_2} - V_{X_3} + V_{X_4})_j \quad (A-7)$$

$$V_{Y_j} = (V_{Y_1} - V_{Y_2} - V_{Y_3} + V_{Y_4})_j \quad (A-8)$$

$$V_{Z_j} = (V_{Z_1} - V_{Z_2} - V_{Z_3} + V_{Z_4})_j \quad (A-9)$$

These velocity components are then substituted into Equation 4 to determine the pressure coefficient at the centroid of the panel.

2. HABP/HAMMITT-MURTHY

The objective of the Hammitt-Murthy solution is to determine the surface pressure ratio, P_c/P_∞ , for application in Equation 9 to calculate the surface pressure coefficient. The procedure used is to determine the shock cone angle, θ_s , and surface Mach number M_c , as outlined in Reference 7. The pressure ratio and local Mach number behind the shock are next obtained followed by an isentropic relation between the shock and surface to obtain P_c/P_∞ .

To determine θ_s the basic equation to be solved is, from Reference 7, the quadratic

$$H_1 h_s^2 + (2 \sin 2\delta) h_s + H_2 = 0 \quad (A-10)$$

where

$$h_s = (\theta_s - \delta)$$

$$H_1 = 2 - (\gamma + 5) \sin^2 \delta$$

$$H_2 = -[(\gamma - 1) \sin^2 \delta + 2/M_\infty^2]$$

Note that once h_s has been calculated and δ has been found from Equation 6, θ_s is then determined. Equation A-10 is first checked to see if the roots are real or imaginary. If the roots are imaginary the flow is detached and the Tangent Cone Empirical method of Reference 2 is used, as follows:

$$\sin \theta_s = [K_C M_\infty \sin \delta + e^{-K_C M_\infty \sin \delta}] / M_\infty \quad (A-11)$$

where

$$K_C = 2(\gamma + 1)/(\gamma + 3)$$

If the roots of Equation A-10 are real then the solution is taken as the quadratic root

$$\theta_s = \delta - \frac{\sin 2\delta}{H_1} \left\{ 1.0 - \left[1.0 + \frac{H_1 H_2}{\sin^2 (2\delta)} \right]^{1/2} \right\} \quad (A-12)$$

If $H_1 \rightarrow 0$, then the term within the brackets in Equation A-12 is expanded into a power series and the solution becomes

$$\theta_s = \delta + \frac{H_2}{2 \sin(2\delta)} \left[1.0 - \frac{1}{4} H_1 H_2 \left(1.0 - \frac{1}{2} H_1 H_2 \right) \right] \quad (A-13)$$

The surface Mach number is determined as

$$M_c = \left[\frac{M_\infty^2 \cos^2 \theta_s (1 + 2h_s^2)}{1 + \frac{\gamma-1}{2} M_\infty^2 (\sin^2 \theta_s - 2h_s^2 \cos^2 \theta_s)} \right]^{1/2} \quad (A-14)$$

The pressure ratio behind the shock is determined next from Reference 8

$$P_s/P_\infty = \frac{2\gamma}{\gamma+1} M_\infty^2 \sin^2 \theta_s - \frac{\gamma-1}{\gamma+1} \quad (A-15)$$

Next the isentropic relations of Reference 8 are used between the shock and surface for constant T_T . First, the surface temperature ratio is determined.

$$\frac{T_c}{T_\infty} = \frac{(1.0 + \frac{\gamma-1}{2} M_\infty^2)}{(1.0 + \frac{\gamma-1}{2} M_c^2)} \quad (A-16)$$

The ratio T_∞/T_s is found as follows (Reference 8)

$$\frac{T_\infty}{T_s} = \frac{(P_s/P_\infty + A)}{\frac{P_s}{P_\infty} (1.0 + A \frac{P_s}{P_\infty})} \quad (A-17)$$

where

$$A = \frac{\gamma-1}{\gamma+1}$$

Next the isentropic relation of Reference 8 is used to determine P_c/P_s

$$P_c/P_s = \left(\frac{T_c}{T_\infty} \frac{T_\infty}{T_s} \right)^{\frac{\gamma}{\gamma-1}} \quad (A-18)$$

Finally, the surface pressure ratio P_c/P_∞ is determined as

$$\frac{P_c}{P_\infty} = \frac{P_c}{P_s} \frac{P_s}{P_\infty} \quad (A-19)$$

$\frac{P_c}{P_\infty}$ is then substituted into Equation 9 to obtain the surface pressure ratio. It was pointed out in the main text that the Hammitt-Murthy solution is applied for $M_\infty \sin \delta > 0.325$ and the second order solution for $M_\infty \sin \delta < 0.3$. For values of $M_\infty \sin \delta$ between these values a transition solution is obtained. This is found by using a Taylor's series expansion of the second order solution in the neighborhood of $M_\infty \sin \delta = 0.3$.

Specifically let

$$C_p(x) = C_{p_{\text{CONE}}(\text{TRANSITION})} \quad \text{for } a < M_\infty \sin \delta < b \quad (\text{A-20})$$

where $a = 0.3$ and $b = 0.325$

$$C_p(a) = C_{p_{\text{CONE}}(2\text{nd-order})} \quad \text{for } M_\infty \sin \delta = a \quad (\text{A-21})$$

$$C_p(b) = C_{p_{\text{CONE}}(\text{HAMMITT-MURTHY})} \quad (\text{A-22})$$

$$X = M_\infty \sin \delta, \Delta X = X - a \quad (\text{A-23})$$

and

$$h = b - a \quad (\text{A-24})$$

Then the transition solution is found as

$$C_p(x) = C_p(a) + \frac{dC_p}{dX} \Delta X + \frac{d^2 C_p}{dX^2} \Delta X^2 \quad (\text{A-25})$$

The first derivative is found by differentiating Equation 8 with respect to $\tan \delta$ and applying the following chain rule:

$$\begin{aligned} \frac{dC_p}{dX} &= \frac{dC_p}{d(M_\infty \sin \delta)} = \frac{dC_p}{d(\tan \delta)} \cdot \frac{d(\tan \delta)}{d(M_\infty \sin \delta)} \\ &= \frac{dC_p}{d(\tan \delta)} \cdot \frac{d(\tan \delta)}{d\delta} \cdot \frac{d\delta}{d(M_\infty \sin \delta)} \\ &= \frac{dC_p}{d(\tan \delta)} \cdot \frac{\sec^2 \delta}{M_\infty \cos \delta} = \frac{dC_p}{d(\tan \delta)} \cdot \frac{1}{M_\infty \cos^3 \delta} \end{aligned} \quad (\text{A-26})$$

Upon differentiating Equation 8 with respect to $\tan \delta$ and combining with Equation A-26 the result is

$$\begin{aligned} \frac{dC_p}{dX} = & \tan \delta \{ 4(\xi - 1.0) + \tan^2 \delta [6(\xi - 1)^2 \\ & - (5M_\infty^2 - 1)(4\xi - 1) + 4A] \} / (M_\infty \cos^3 \delta) \end{aligned} \quad (A-27)$$

where the terms in this equation are the same as defined in Equation 8. The second derivative is found from the finite difference relation

$$\frac{d^2 C_p}{dX^2} = \frac{C_p(b) - 2C_p(a) + C_p(a-h)}{h^2} \quad (A-28)$$

where

$$C_p(a-h) = C_p(a) - \frac{dC_p}{dX} \cdot h$$

$$\frac{d^2 C_p}{dX^2} = \frac{C_p(b) - C_p(a) - \frac{dC_p}{dX} \cdot h}{h^2} \quad (A-29)$$

3. HARP-PRANDTL-MEYER EXPANSION

The general procedure for the Prandtl-Meyer expansion from free-stream is as follows: first, the relations from Reference 8 are used to obtain the surface Mach number, M_c . Then an isentropic relationship is applied between the freestream and surface to obtain P_c/P_∞ . This expansion procedure is used whenever δ from Equation 6 is negative.

The Prandtl-Meyer angle corresponding to the freestream is

$$\nu_\infty = \sqrt{\frac{\gamma+1}{\gamma-1}} \tan^{-1} \sqrt{\frac{\gamma-1}{\gamma+1} (M_\infty^2 - 1)} - \tan^{-1} \sqrt{M_\infty^2 - 1} \quad (A-30)$$

The Prandtl-Meyer angle after expansion is

$$\nu_c = \nu_\infty + |\delta| \quad (A-31)$$

The approximate downstream surface Mach number is found as follows

$$M_C \approx M_\infty + \left(\frac{dM_\infty}{dv} \right) \Delta v \quad (A-32)$$

Differentiating Equation A-30 for $\frac{dM_\infty}{dv} \Delta v$ and substituting into Equation A-32 gives

$$M_C \approx M_\infty \left[1 + \frac{(\Delta v) \left(1 + \frac{\gamma-1}{2} M_\infty^2 \right)}{\sqrt{M_\infty^2 - 1}} \right] \quad (A-33)$$

where

$$\Delta v = v_C - v_\infty = |\delta|$$

Equation A-30 can be used with v_C replacing v_∞ and M_C replacing M_∞ and rearranged to give

$$M_C = \left\{ 1.0 + \left(R \sqrt{\frac{\gamma+1}{\gamma-1}} \right)^2 \right\}^{1/2} \quad (A-34)$$

$$\text{where } R = \tan \left[\frac{v_C + \tan^{-1} \sqrt{M_C^2 - 1.0}}{\sqrt{\frac{\gamma+1}{\gamma-1}}} \right]$$

Equation A-34 has the form

$$M_C = g(M_C) \quad (A-35)$$

or

$$M_C - g(M_C) = F(M_C) = 0$$

and

$$1 - g'(M_C) = F'(M_C) \quad (A-36)$$

Equation A-35 may be solved by iterating for the surface Mach number M_c using the Newtonian method

$$M_{c_{i+1}} = M_{c_i} - \frac{F(M_{c_i})}{F'(M_{c_i})} \quad (A-37)$$

$$= M_{c_i} - \frac{M_{c_i} - g(M_{c_i})}{1 - g'(M_{c_i})} \quad (A-38)$$

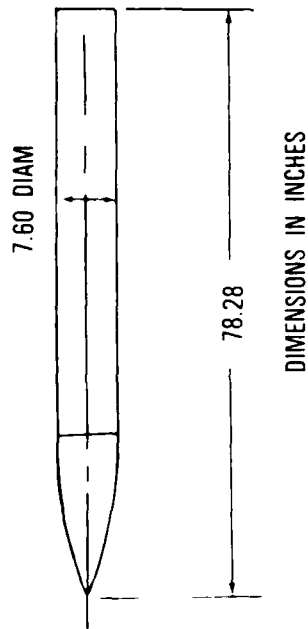
$$= \frac{g(M_{c_i}) - g'(M_{c_i})M_{c_i}}{1 - g'(M_{c_i})} \quad (A-39)$$

With Equation A-32 used as a starting value, successive iterations of Equation A-39 will yield the final surface Mach number M_c for a given value of v_c . With M_c determined, the pressure coefficient is determined from the isentropic relationship given in Equation 14.

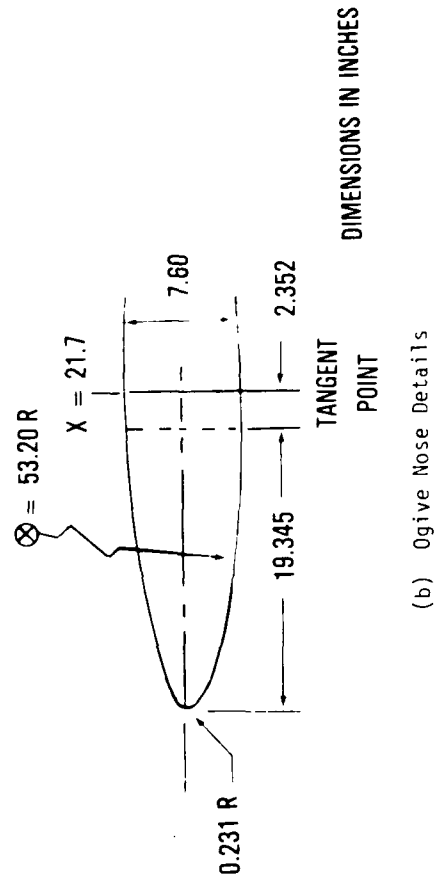
REFERENCES

1. F. A. Woodward, An Improved Method for the Aerodynamic Analysis of Wing-Body-Tail Configurations in Subsonic and Supersonic Flow, NASA CR-2228, May 1973.
2. A. E. Gentry, D. N. Smyth, and W. R. Oliver, The Mark IV Supersonic-Hypersonic Arbitrary Body Program, AFFDL-TR-73-159, November 1973.
3. D. C. Baker and D. E. Reichenau, Aerodynamic Characteristics of an MX Missile at Freestream Mach Numbers from 0.3 to 1.3, and Angles of Attack up to 180 Degrees, AEDC-TR-75-34, April 1975.
4. E. J. Landrum, Wind Tunnel Pressure Data at Mach Numbers 1.6 to 4.63 for a Series of Bodies of Revolution at Angles of Attack from -4° to 60°, NASA TM X-3558, October 1977.
5. C. B. Butler, E. S. Sears, and S. G. Pallas, Aerodynamic Characteristics of a 2, 3, and 4 Caliber Tangent-Ogive Cylinders with Nose Bluntness Ratios of 0.0, 0.25, 0.50, and 0.75 at Mach Numbers from 0.6 to 4.0, AFATL-TR-77-8, January 1977.
6. M. D. Van Dyke, Second-Order Slender Body Theory-Axisymmetric Flow, NASA TR R-47, 1959.
7. A. G. Hammitt and K. R. Murthy, Approximate Solutions for Supersonic Flow Over Wedges and Cones, JAS, January 1960, pp. 71-73.
8. Ames Research Staff, Equations, Tables and Charts for Compressible Flow, NACA TR 1135, 1953.
9. V. Dahlem and M. L. Buck, Experimental and Analytical Investigations of Vehicle Designs for High Lift-to-Drag Ratios in Hypersonic Flight, AFFDL-TR-67-138, February 1968.
10. A. H. Shapiro, The Dynamics and Thermodynamics of Compressible Fluid Flow, The Ronald Press, 1953.
11. L. H. Jorgensen, Prediction of Static Aerodynamic Characteristics for Space-Shuttle-Like and Other Bodies at Angles of Attack from 0° to 180°, NASA-TN-D-6996.
12. C. L. Dyer and C. B. Heath, A Source-Doublet Approach to Modeling Triple Ejector Rack Store Configurations and Force Calculations, AFFDL-TR to be published.
13. C. H. Fox, Jr., Experimental Surface Pressure Distributions for a Family of Axisymmetric Bodies at Subsonic Speeds, NASA TM X-2439, December 1971.

MODEL GEOMETRY



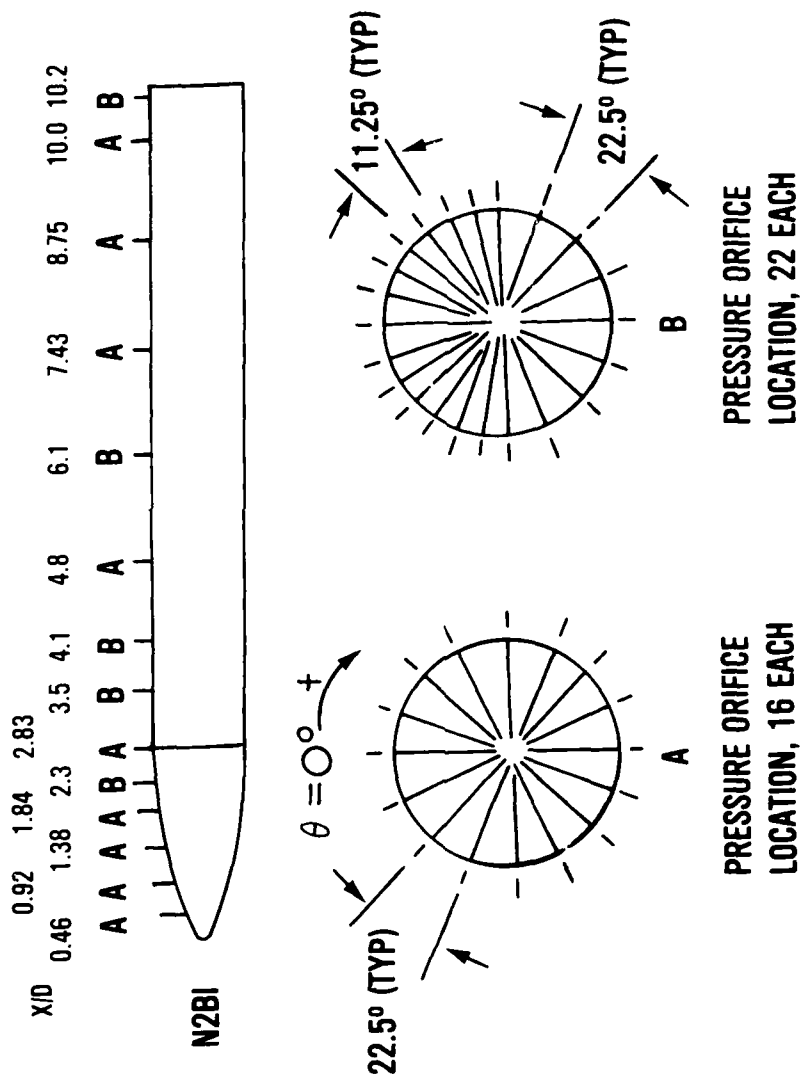
(a) Model Overall Dimensions



(b) Ogive Nose Details

Figure 1. Model Geometry and Pressure Orifice Locations for USSAERO Comparisons

MODEL PRESSURE ORIFICE LOCATIONS



(c) Orifice Locations

Figure 1. Concluded

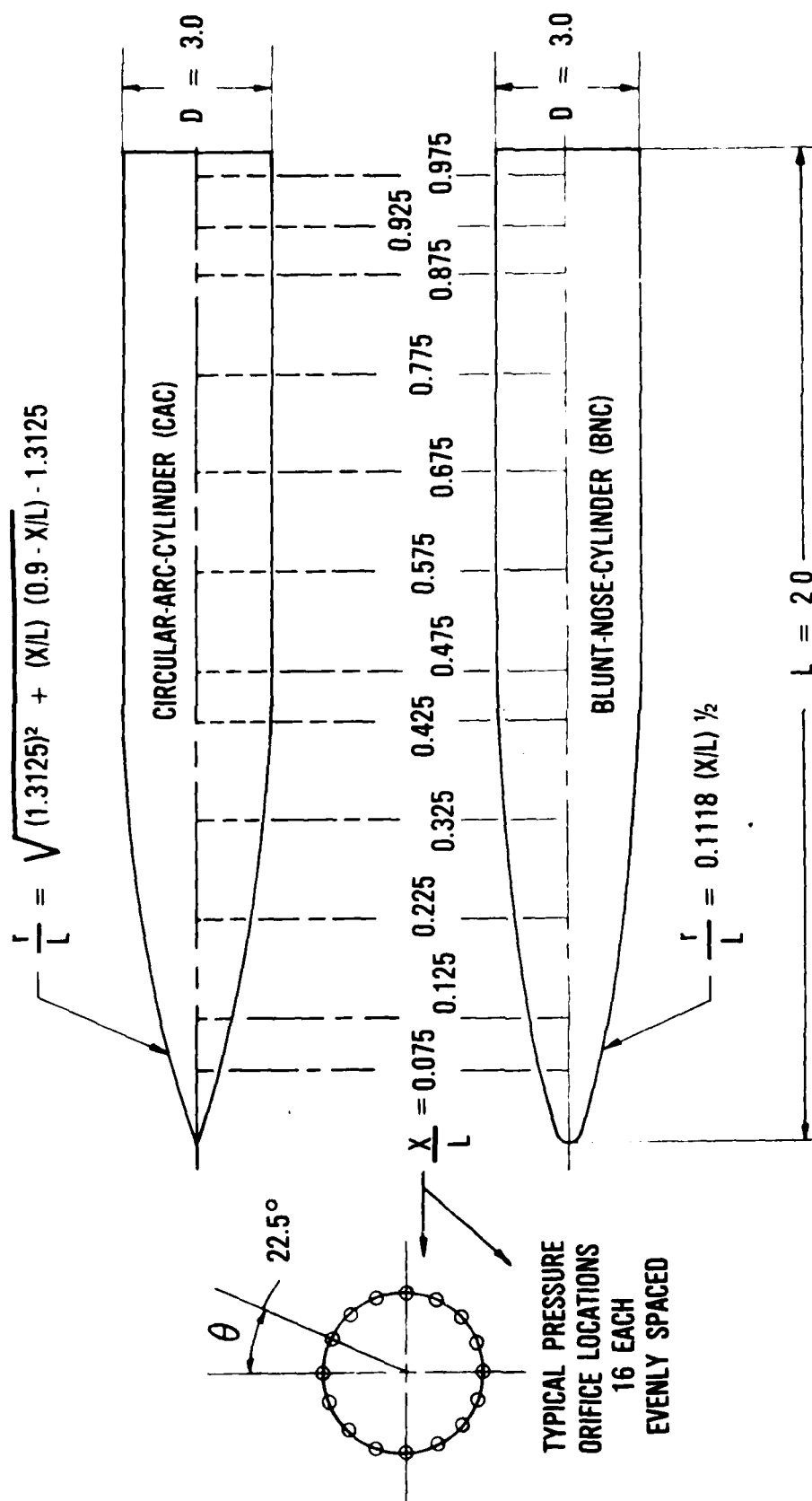


Figure 2. Model Geometries and Pressure Orifice Locations for HABP Pressure Prediction Comparisons.

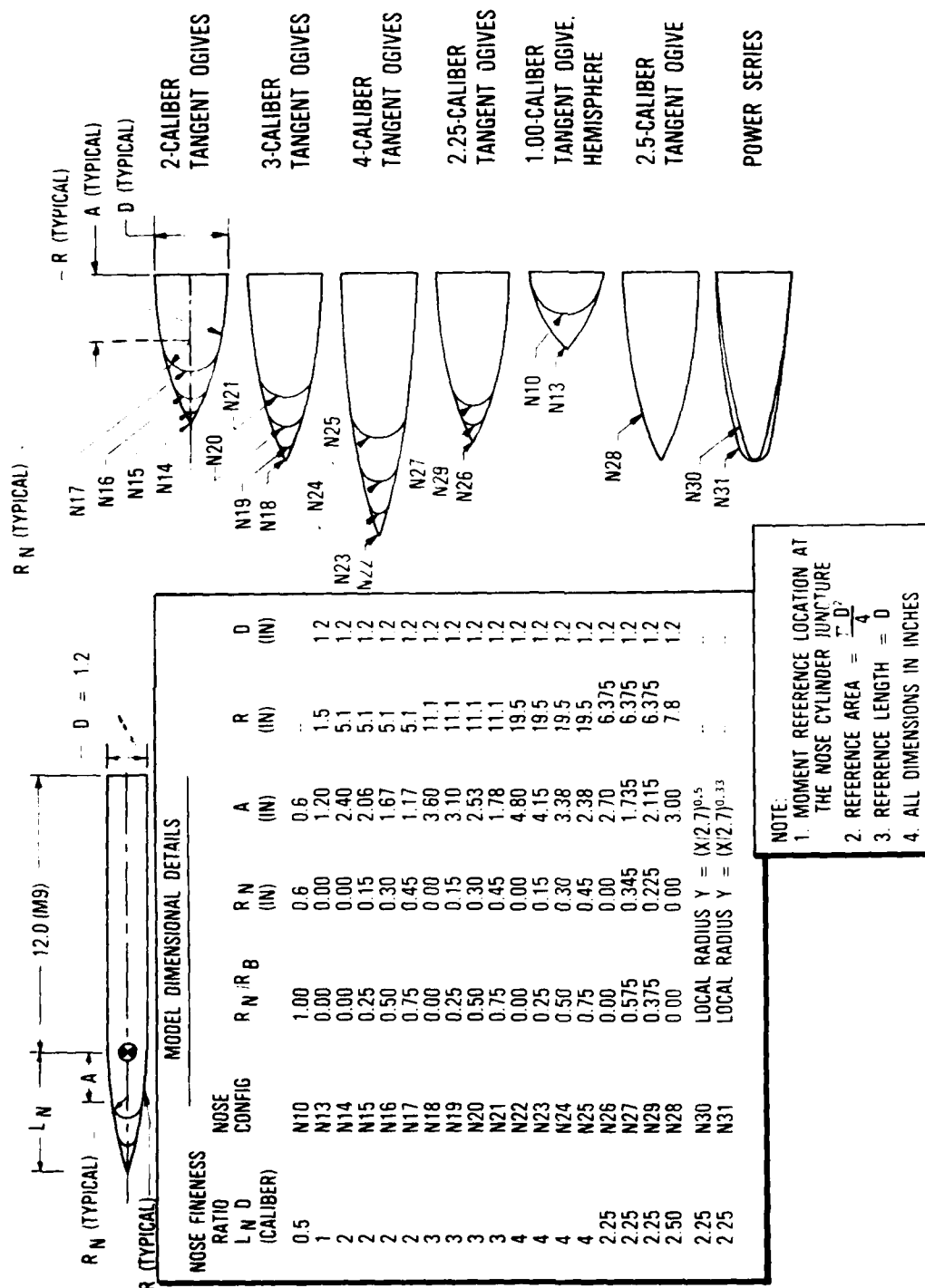


Figure 3. Model Geometries for HABP Force and Moment Comparisons.

USSAERO BODY GEOMETRY REPRESENTATION

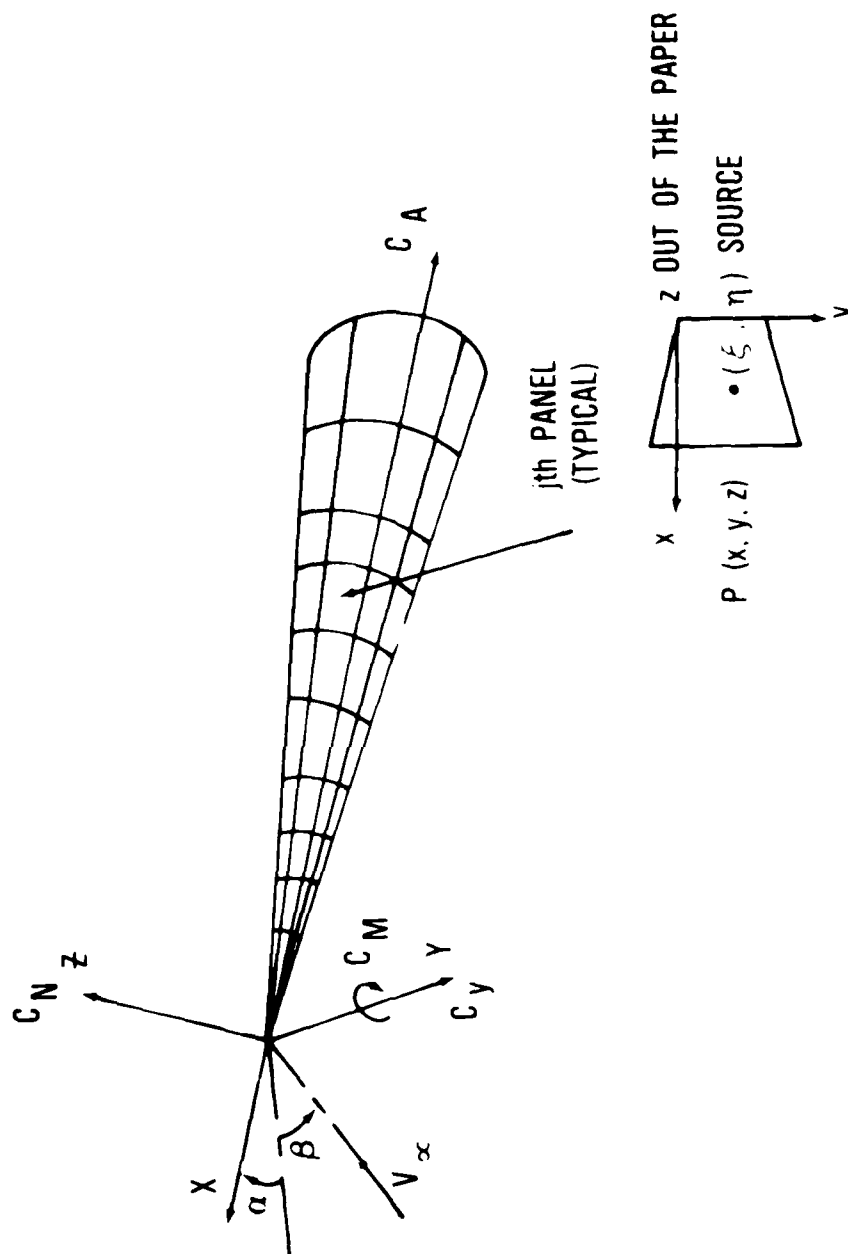


Figure 4. Axis and Coefficient Nomenclature

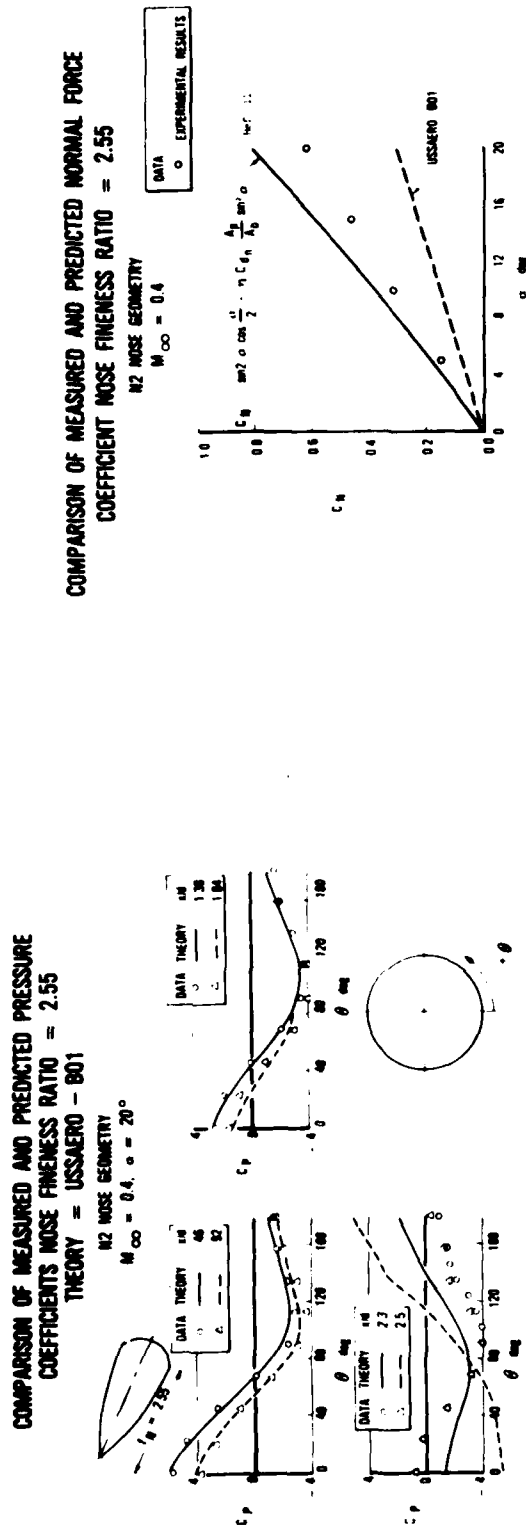
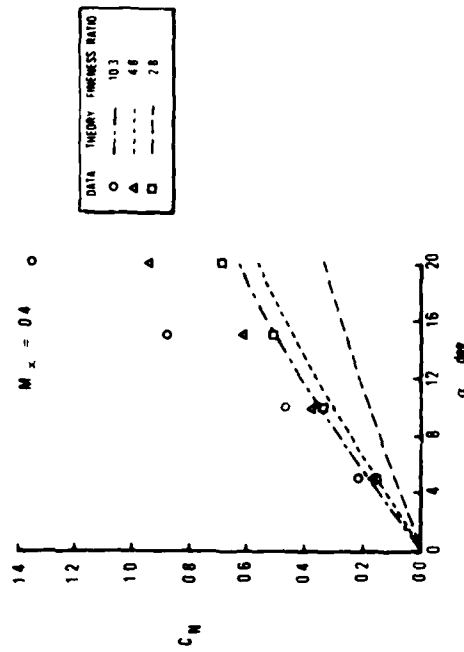


Figure 5. Comparison of USSAERO with Experiment for a Typical Ogive Nose Geometry.

EFFECT OF FINENESS RATIO ON NORMAL FORCE
COEFFICIENT/COMPARISON WITH USSAERO-B01



EFFECT OF FINENESS RATIO ON PREDICTED PRESSURE
COEFFICIENTS (NOSE FINENESS RATIO = 2.55)

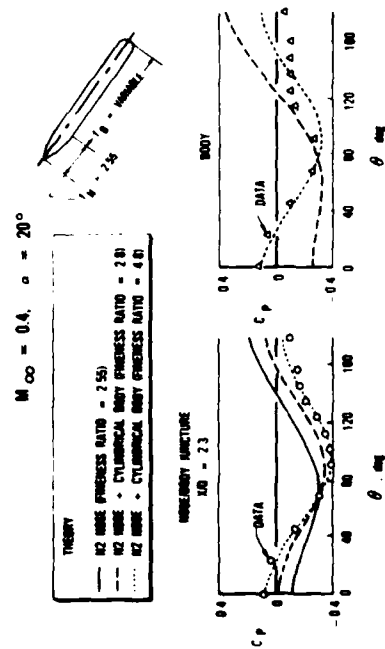


Figure 6. Effect of Adding an Afterbody on the USSAERO Comparisons with Experiment.

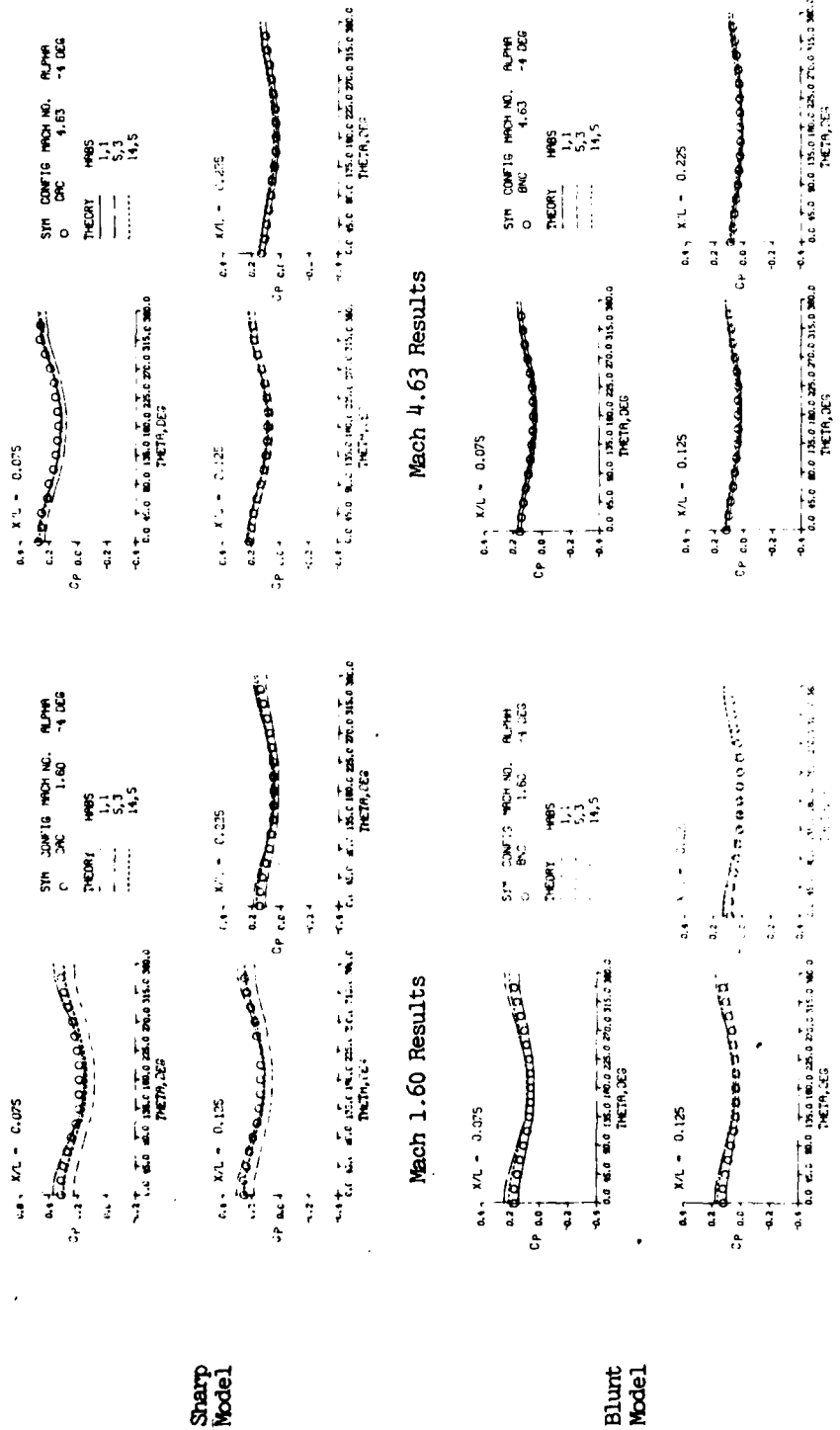
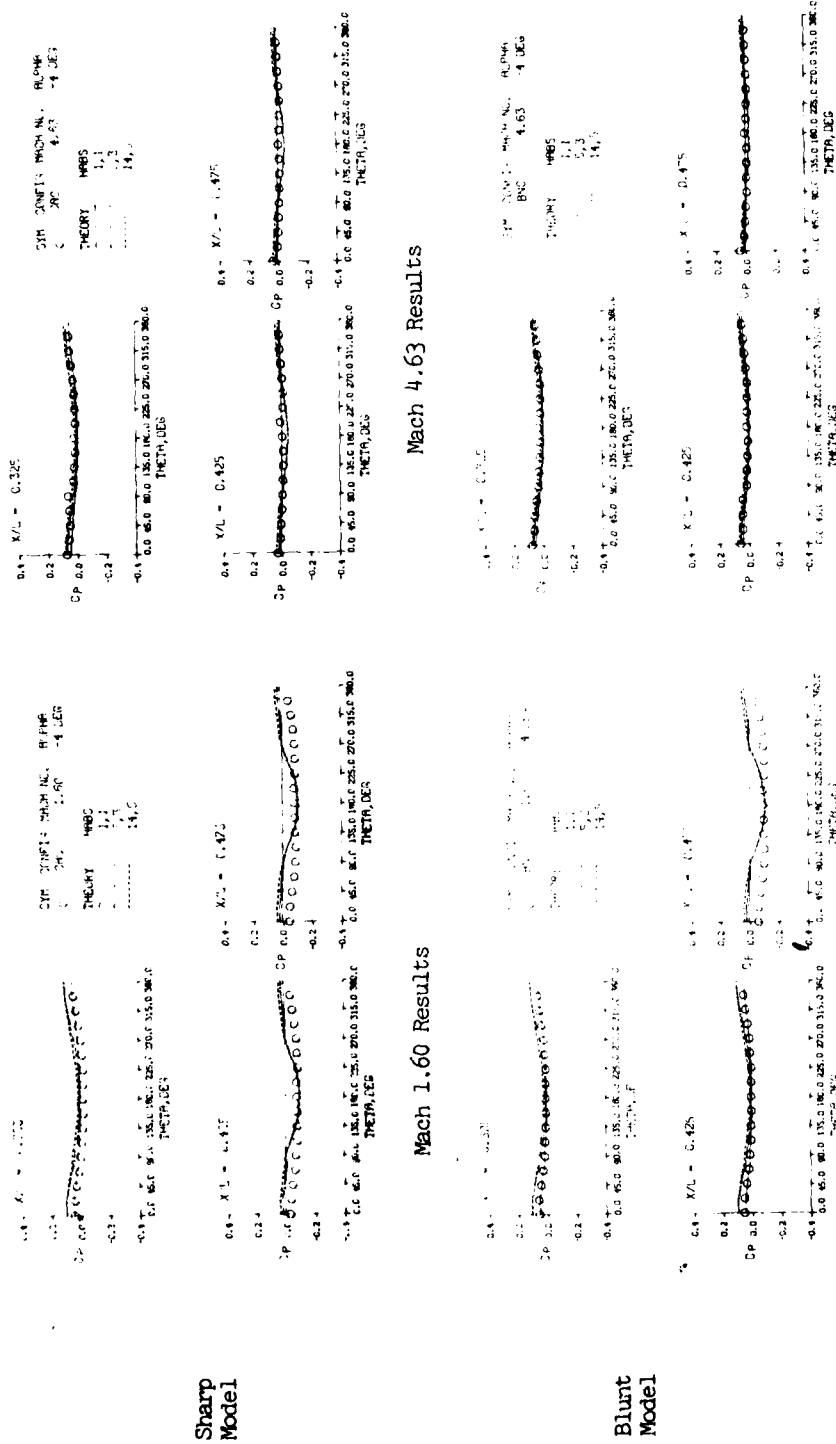
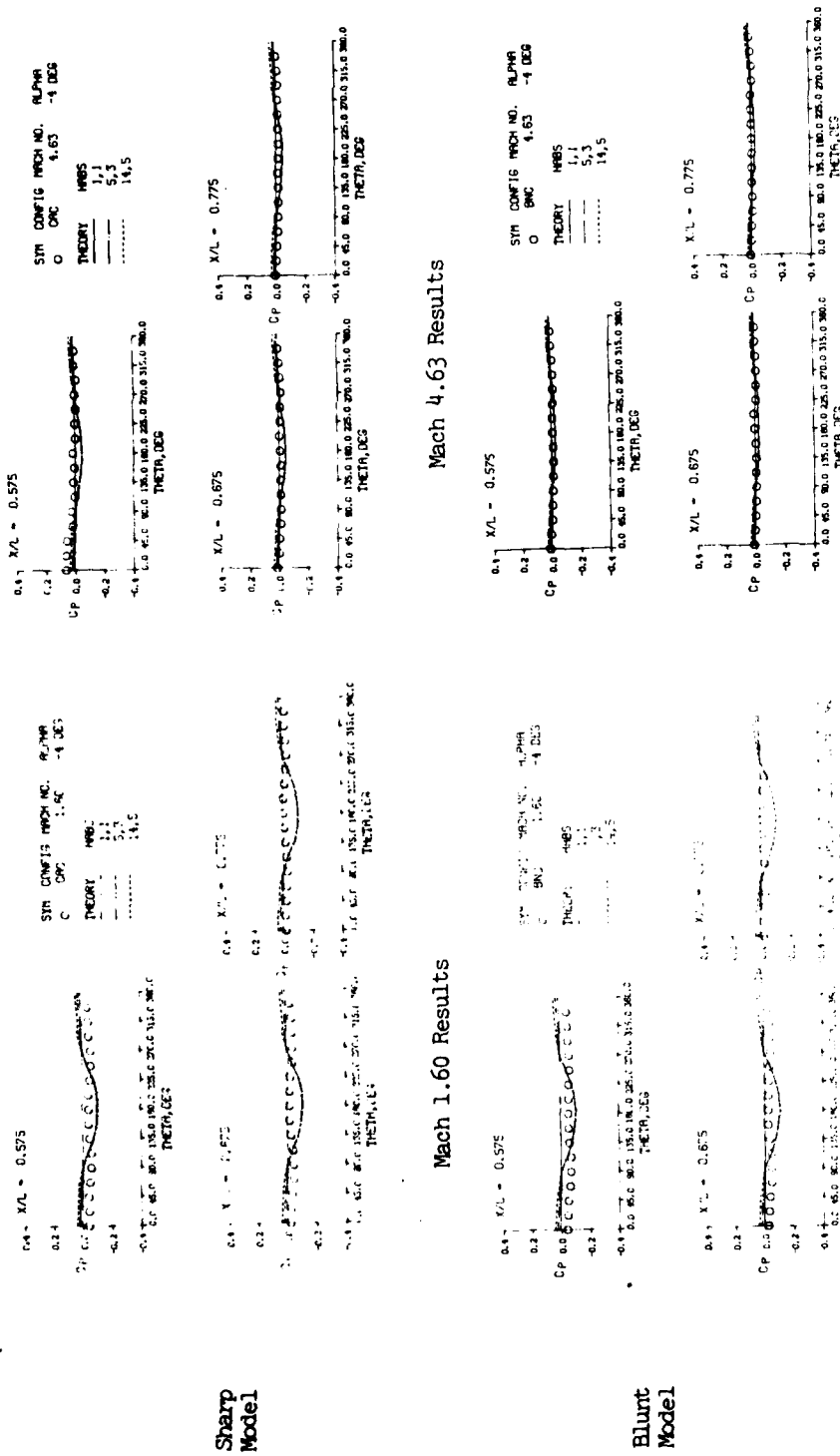


Figure 7. Comparison of Pressure Coefficient Data with the HASP Analytical Results. Effects of Mach Number and Nose Bluntness, Alpha = -4 Degrees.





(c) X/L = 0.575 to 0.775

Figure 7. Continued

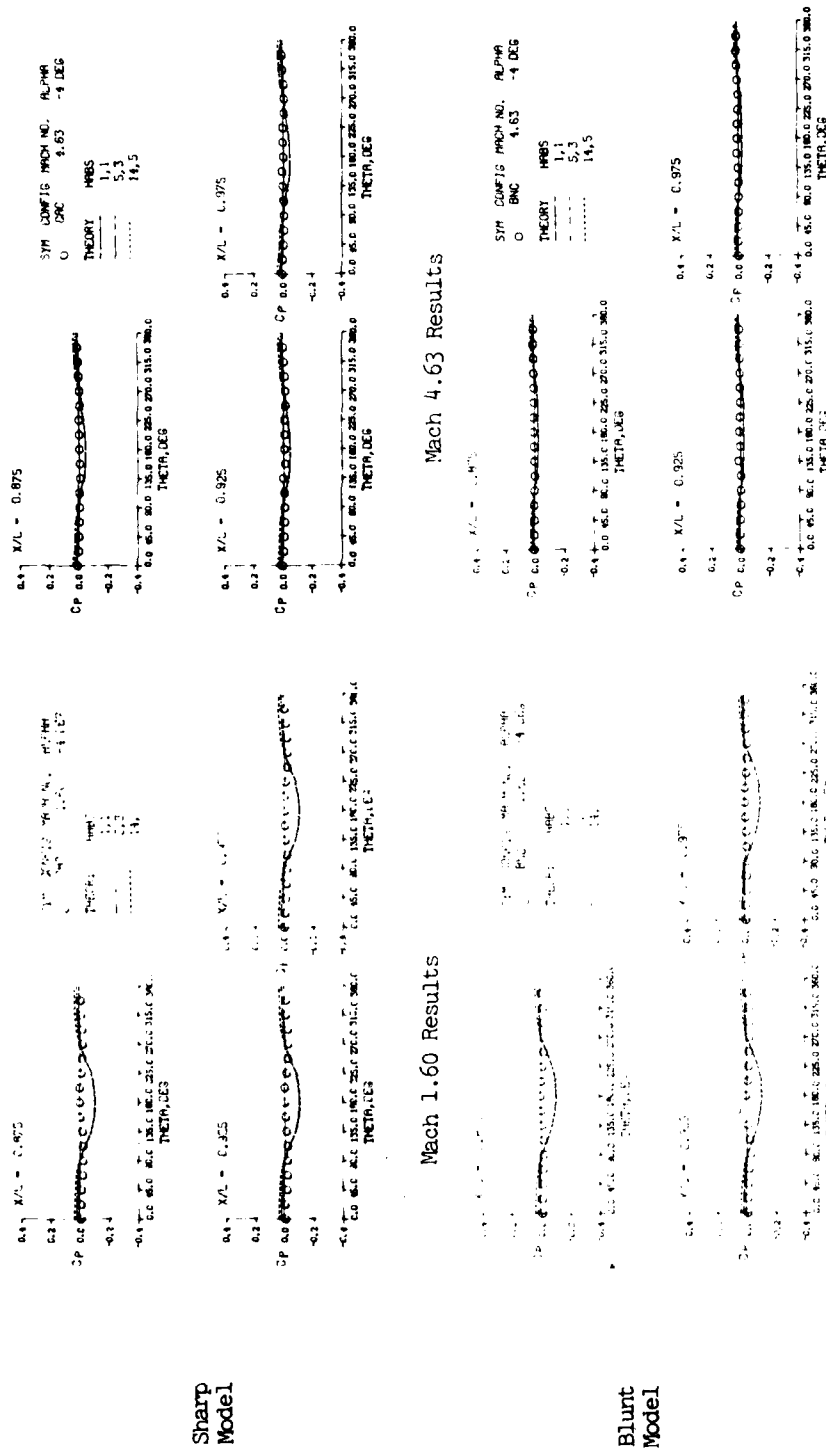
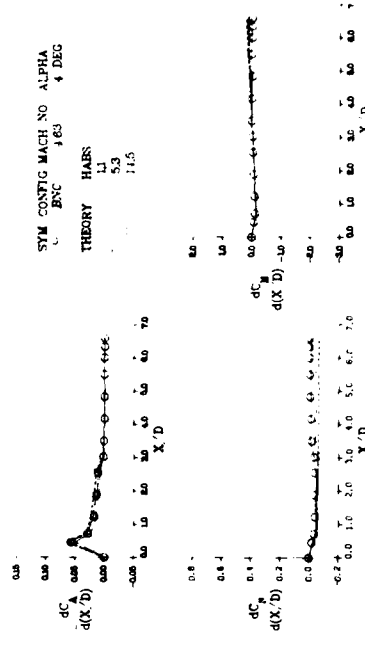
(d) $X/L = 0.875$ to 0.975

Figure 7. Concluded



Mach 4.63 Results



Mach 1.60 Results

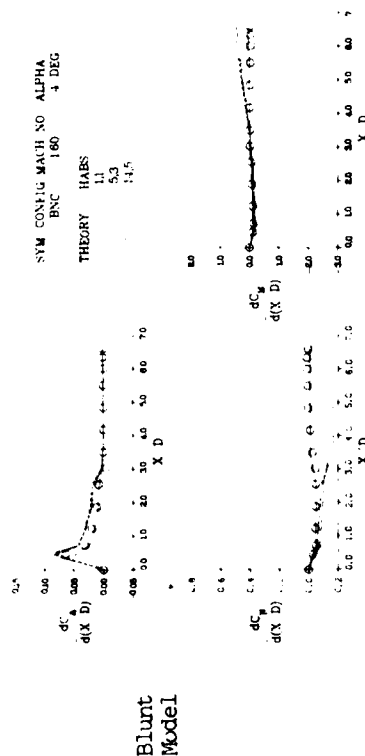
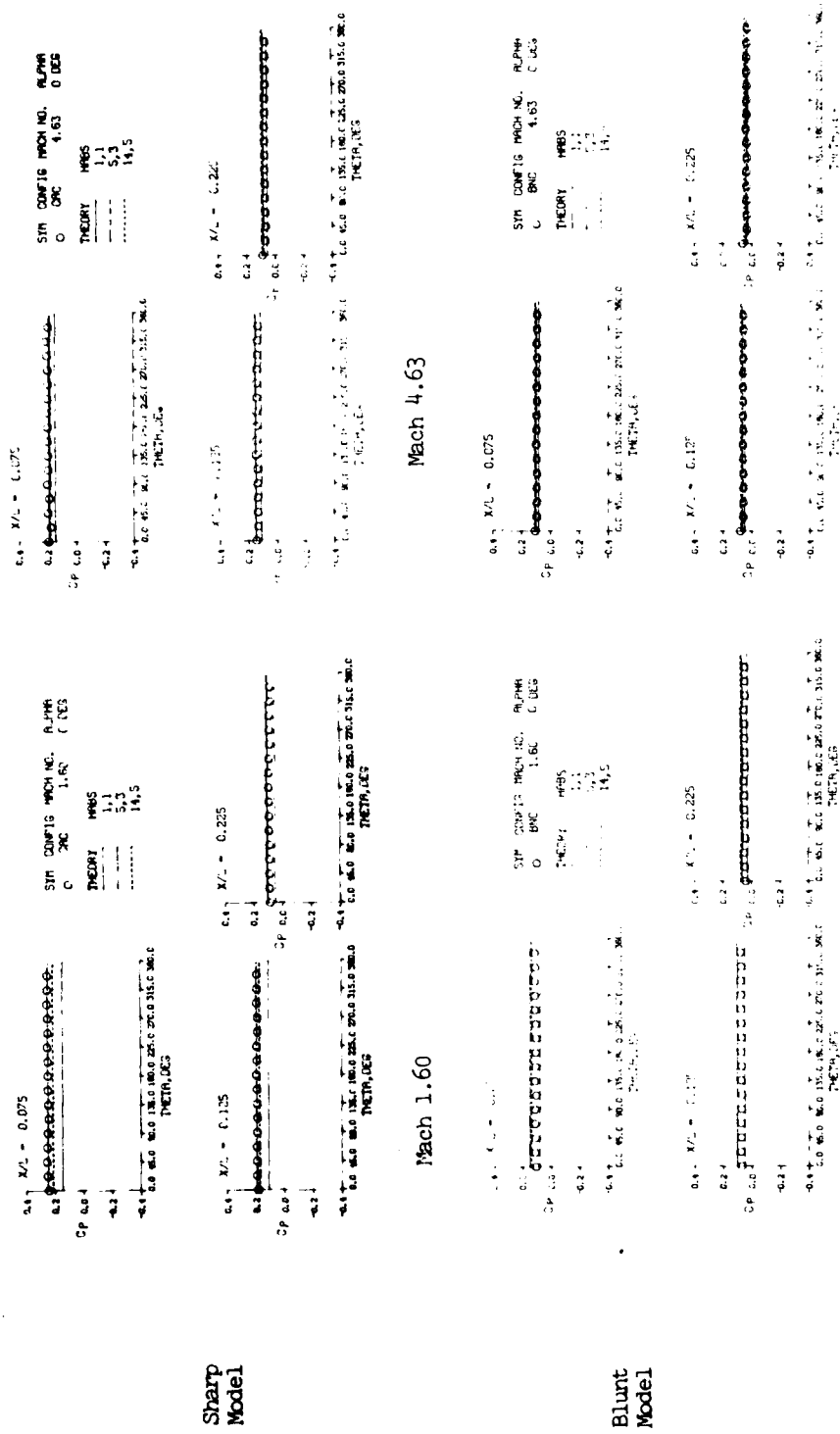


Figure 8. Integrated HABS Comparisons with Experiment for Distributed Local Force and Moment Results, Alpha = -4 Degrees.



(a) X/L = 0.075 to 0.225

Figure 9. HABP Pressure Comparisons at $\alpha = 0$ Degrees.

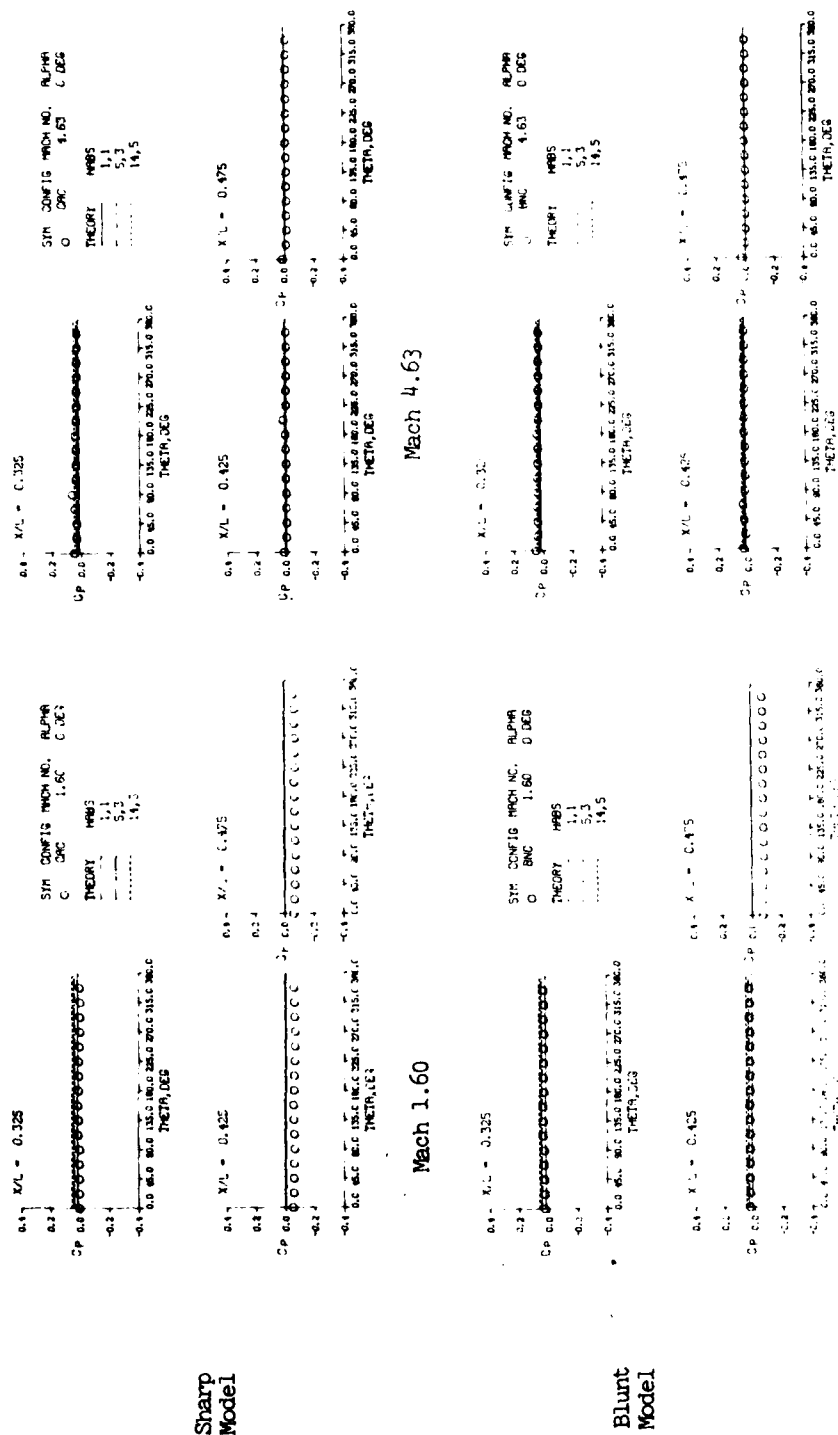


Figure 9. Continued

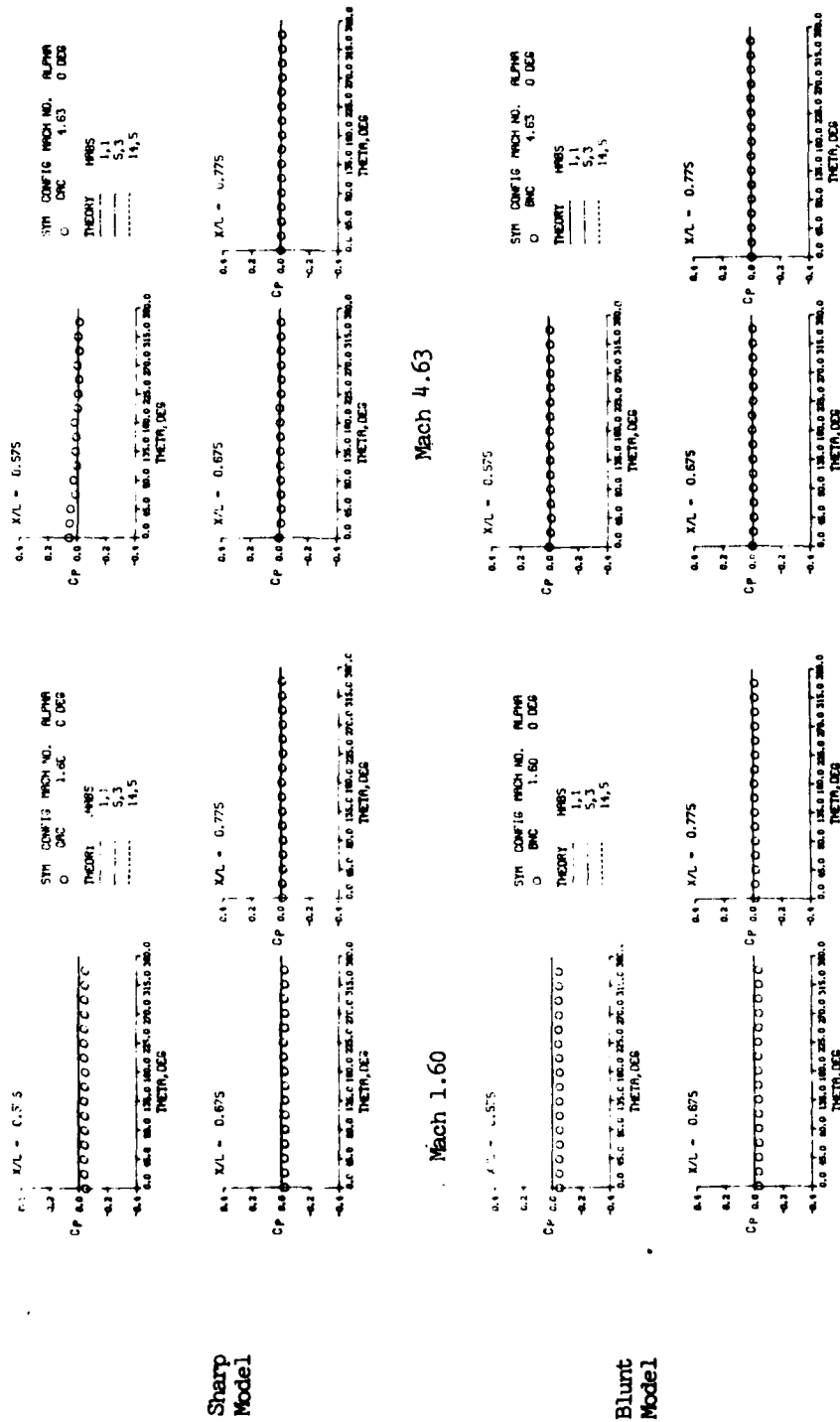
(c) $X/L = 0.575$ to 0.775

Figure 9. Continued

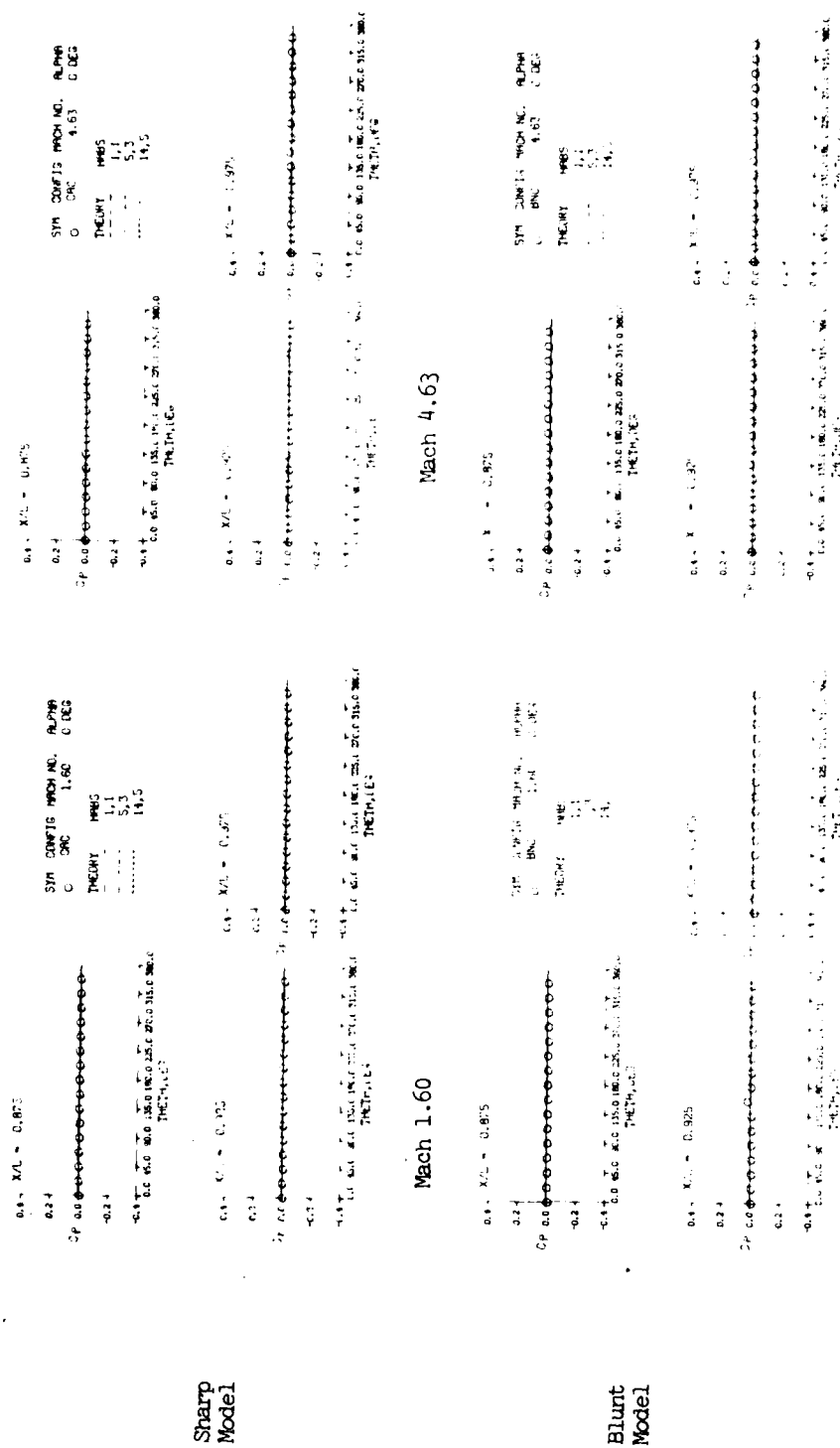


Figure 9. Concluded

(d) $X/L = 0.875$ to 0.975

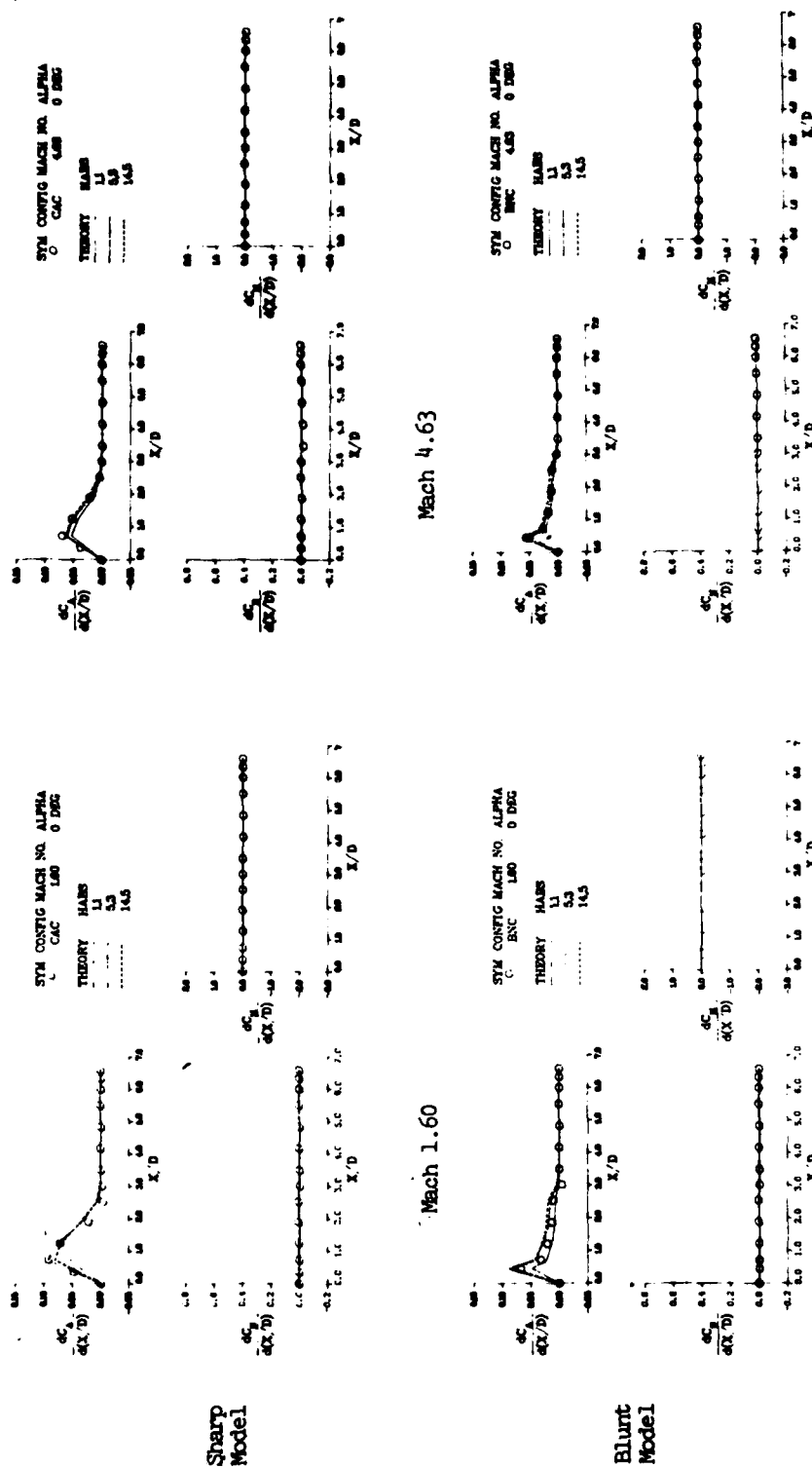
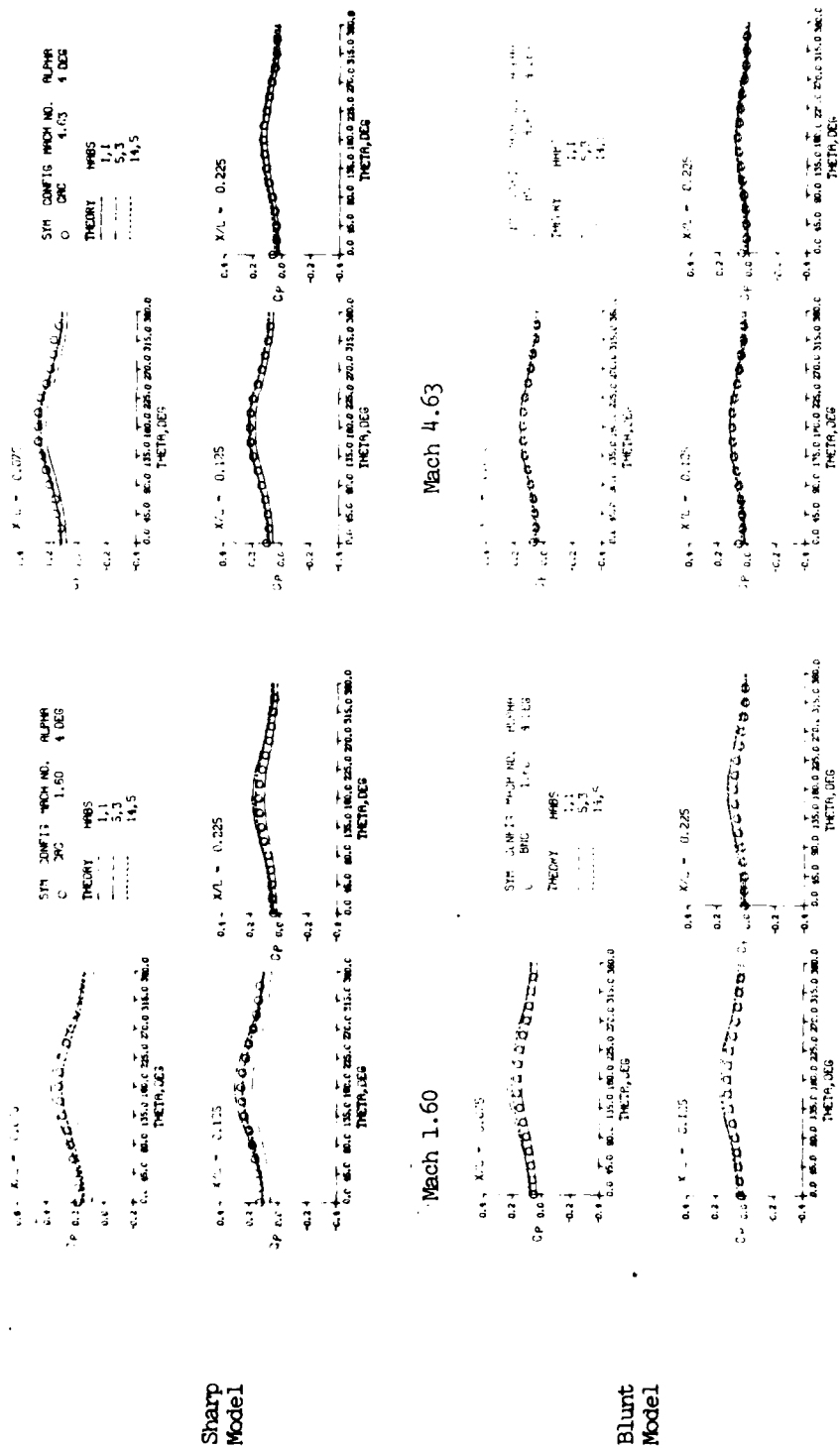
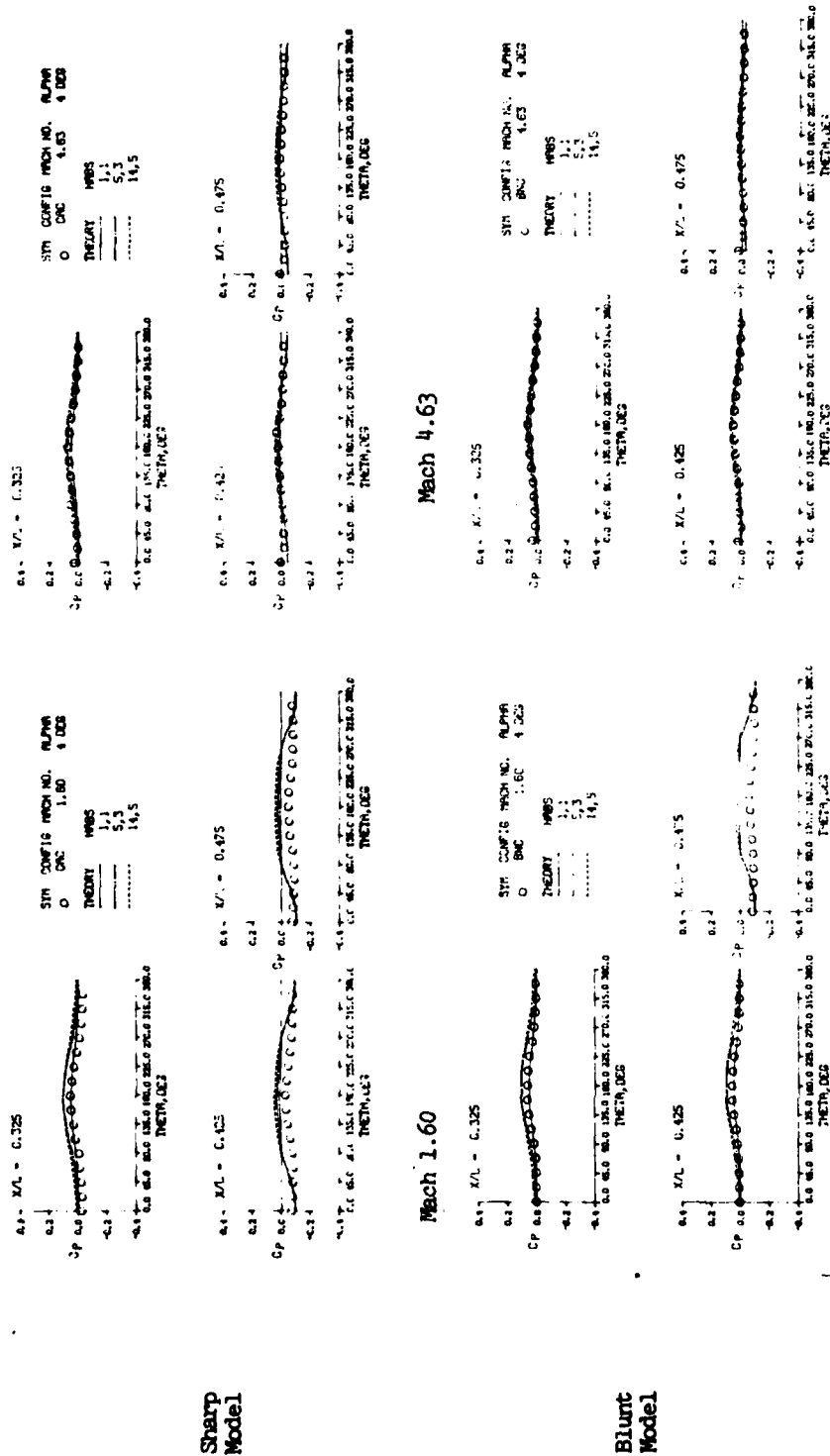


Figure 10. Integrated HABP Local Force and Moment Distribution, $\alpha = 0$ Degrees.



(a) $X/L = 0.075$ to 0.225

Figure 11. HABP Pressure Comparisons for Alpha = 4 Degrees.



(b) $X/L = 0.325$ to 0.475

Figure 11. Continued

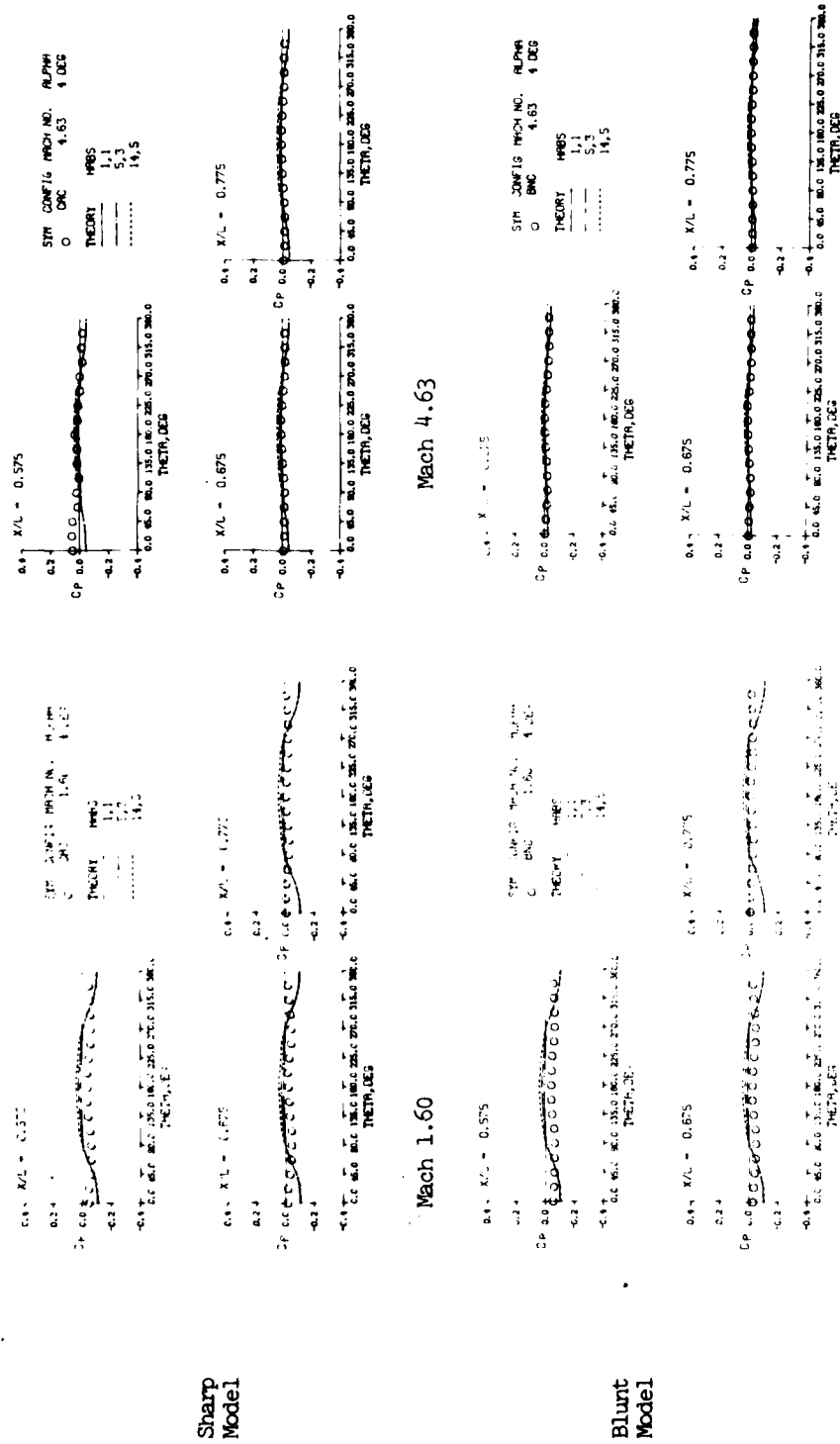
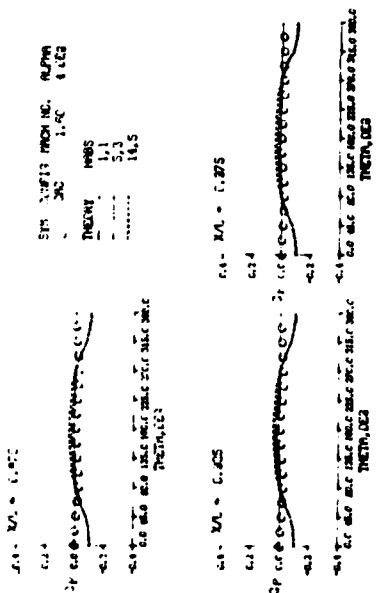
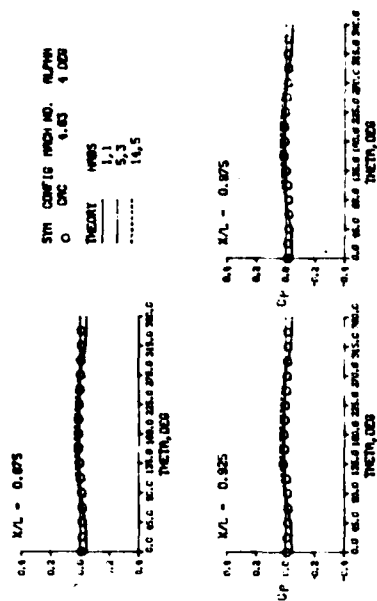


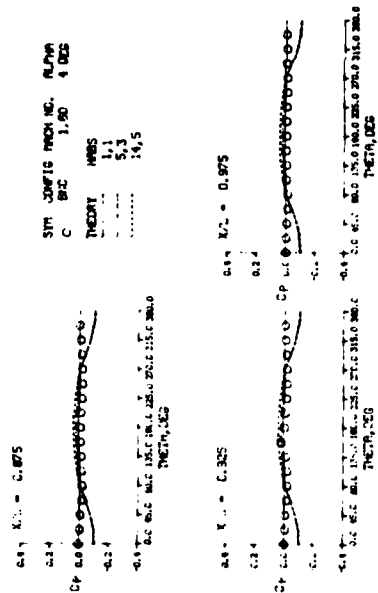
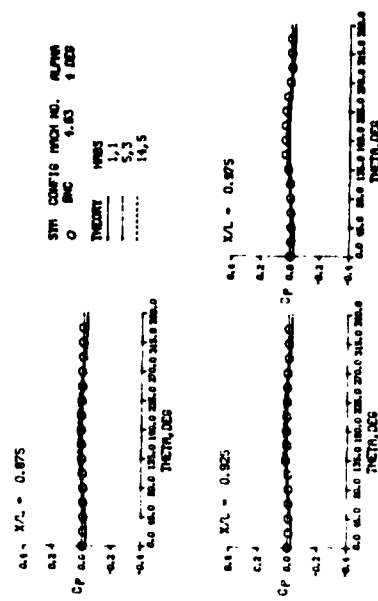
Figure 11. Continued

(c) $X/L = 0.575$ to 0.775



Mach 1.60

Mach 4.63



(d) X/L = 0.875 to 0.975

Figure 11. Concluded

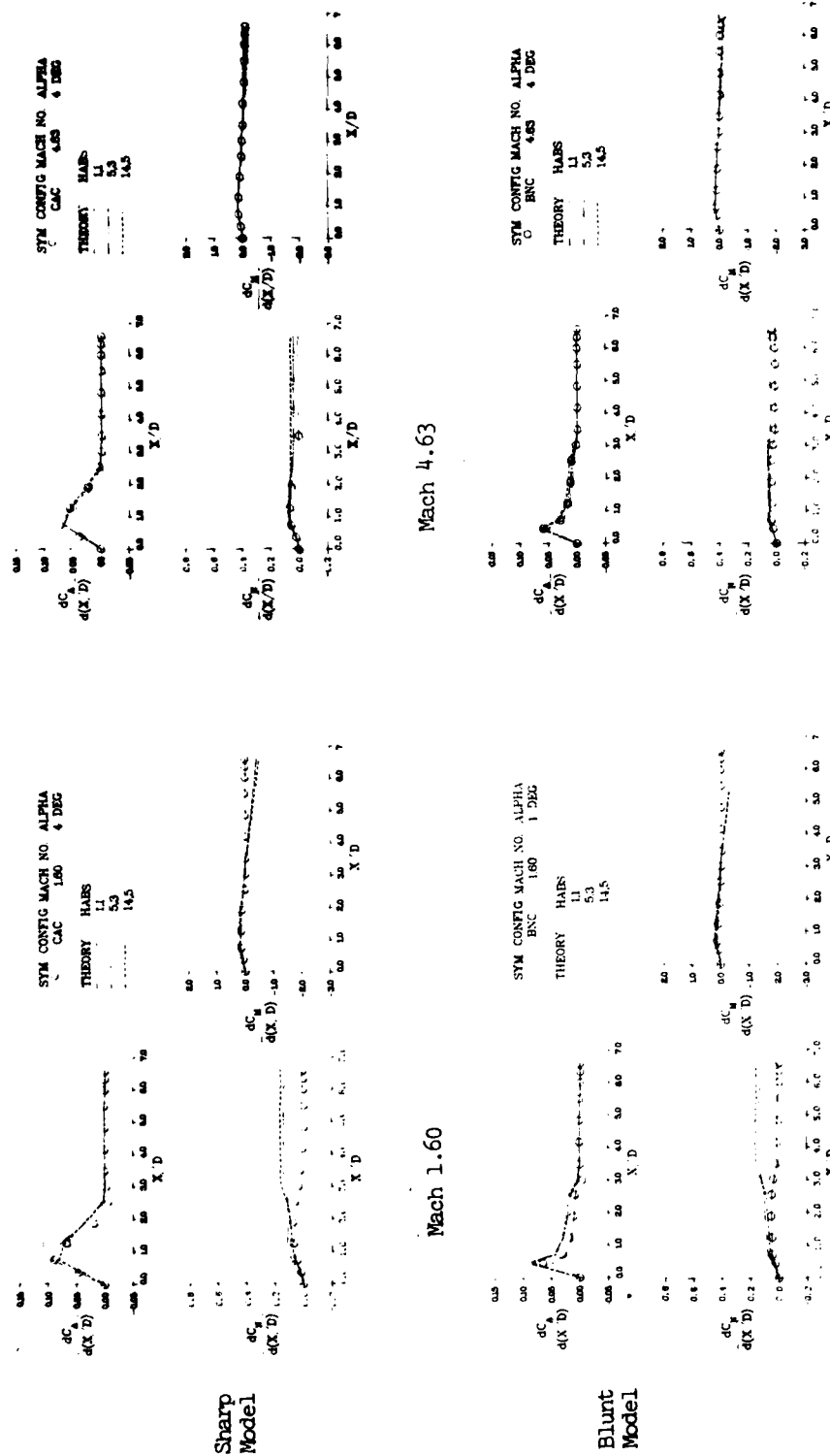


Figure 12. Integrated HABP Local Force and Moment Distribution, Alpha = 4 Degrees.

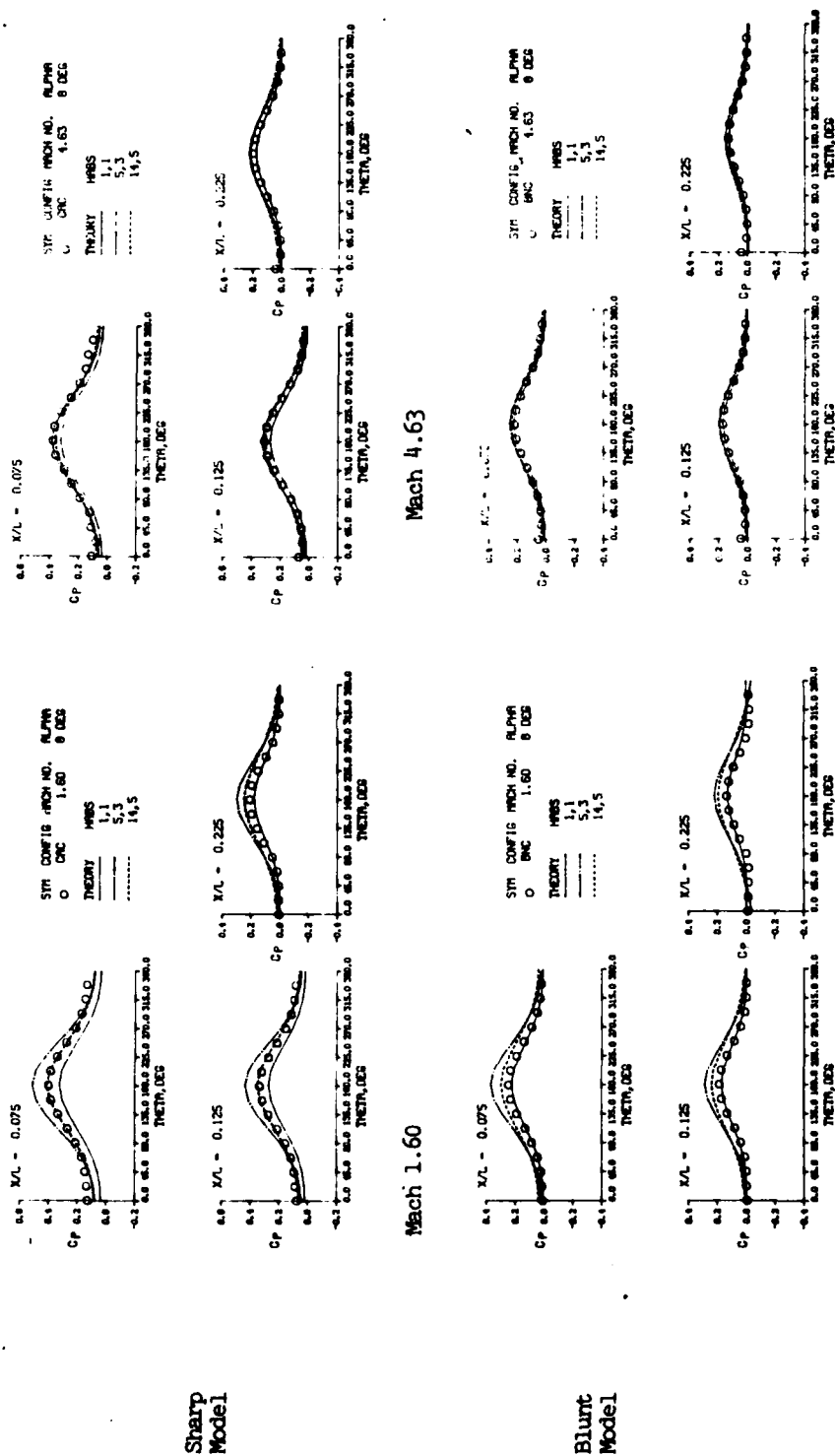
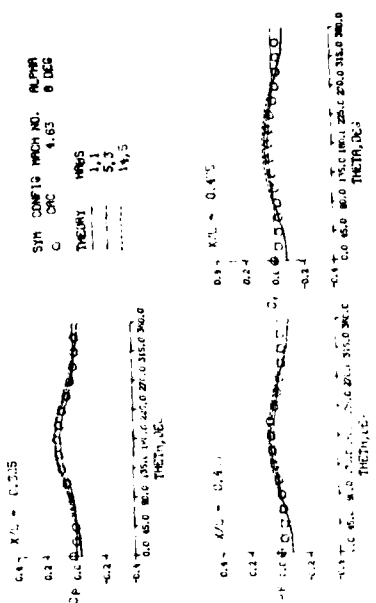
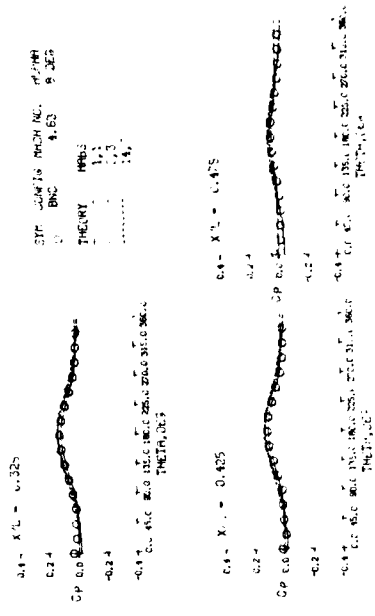
(a) $X/L = 0.075$ to 0.225

Figure 13. HARP Pressure Prediction Comparisons at Alpha = 8 Degrees.

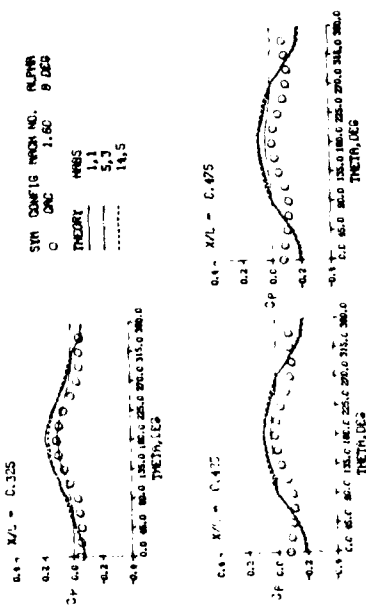


Sharp
Model

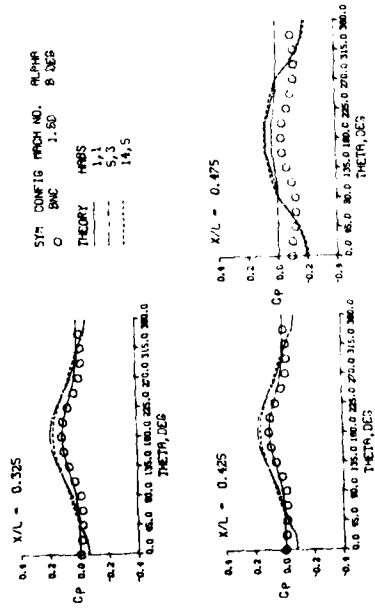
Mach 4.63



Blunt
Model



Mach 1.60



(b) X/L = 0.325 to 0.475

Figure 13. Continued

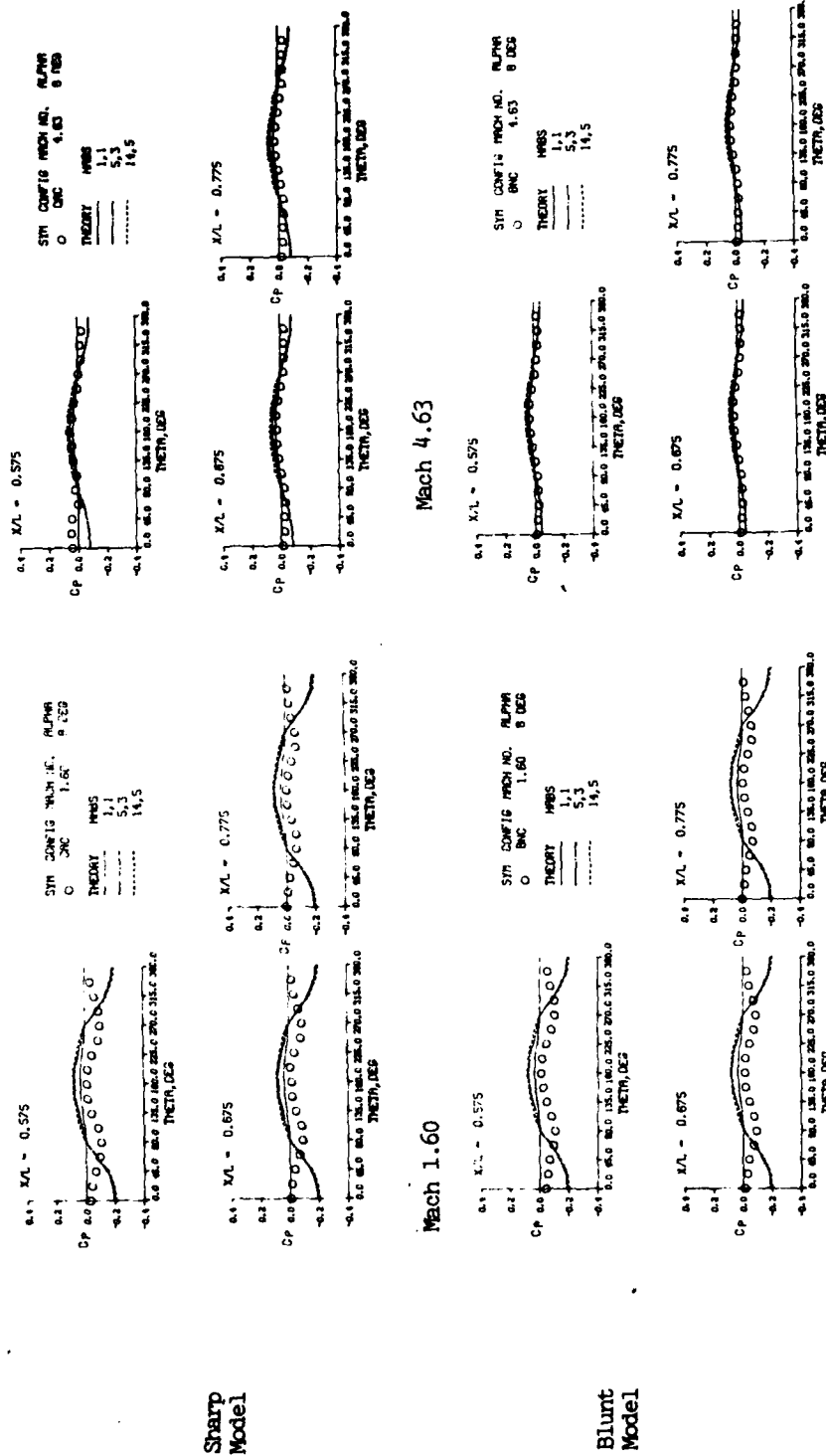


Figure 13. Continued

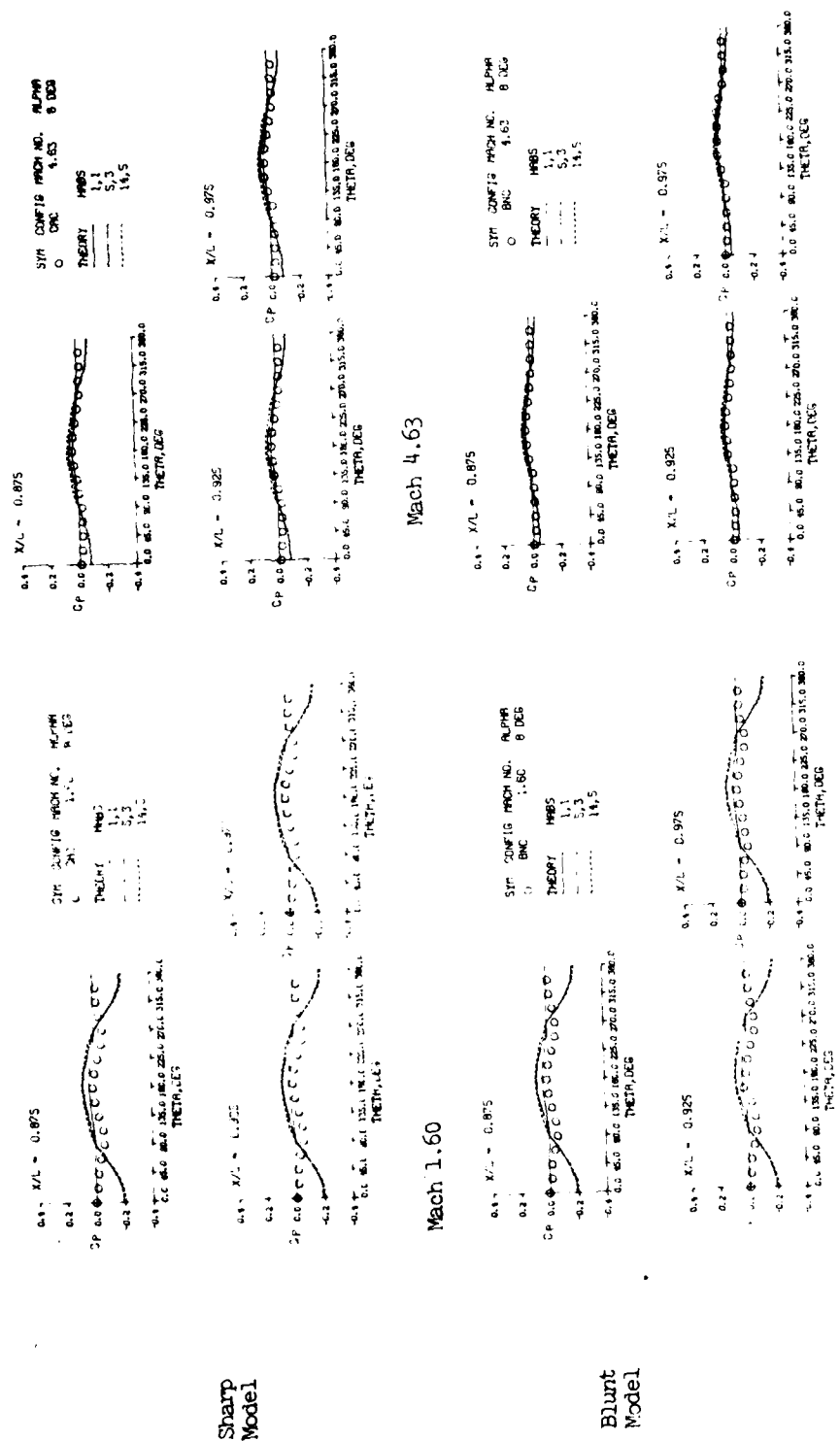
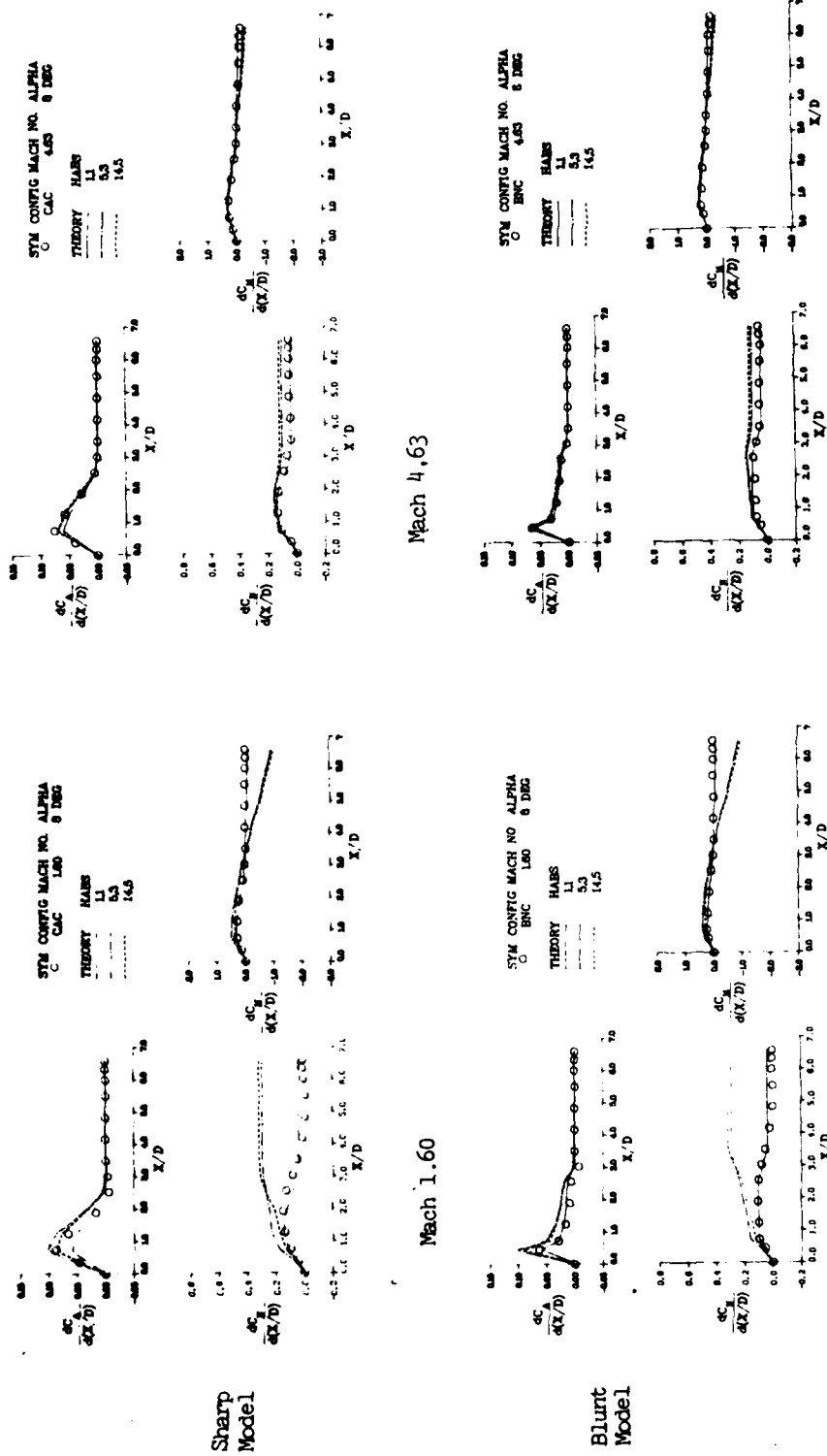
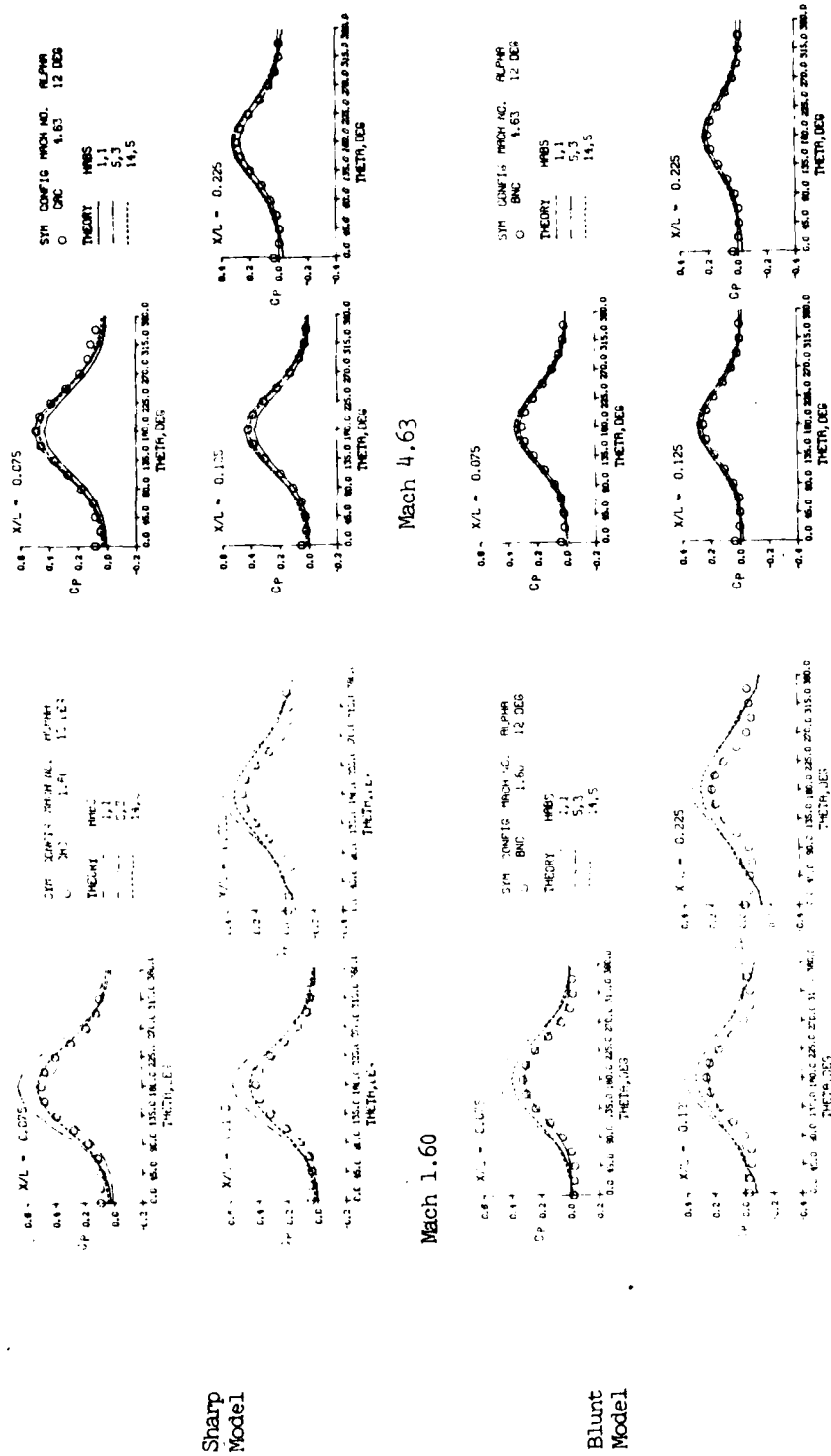
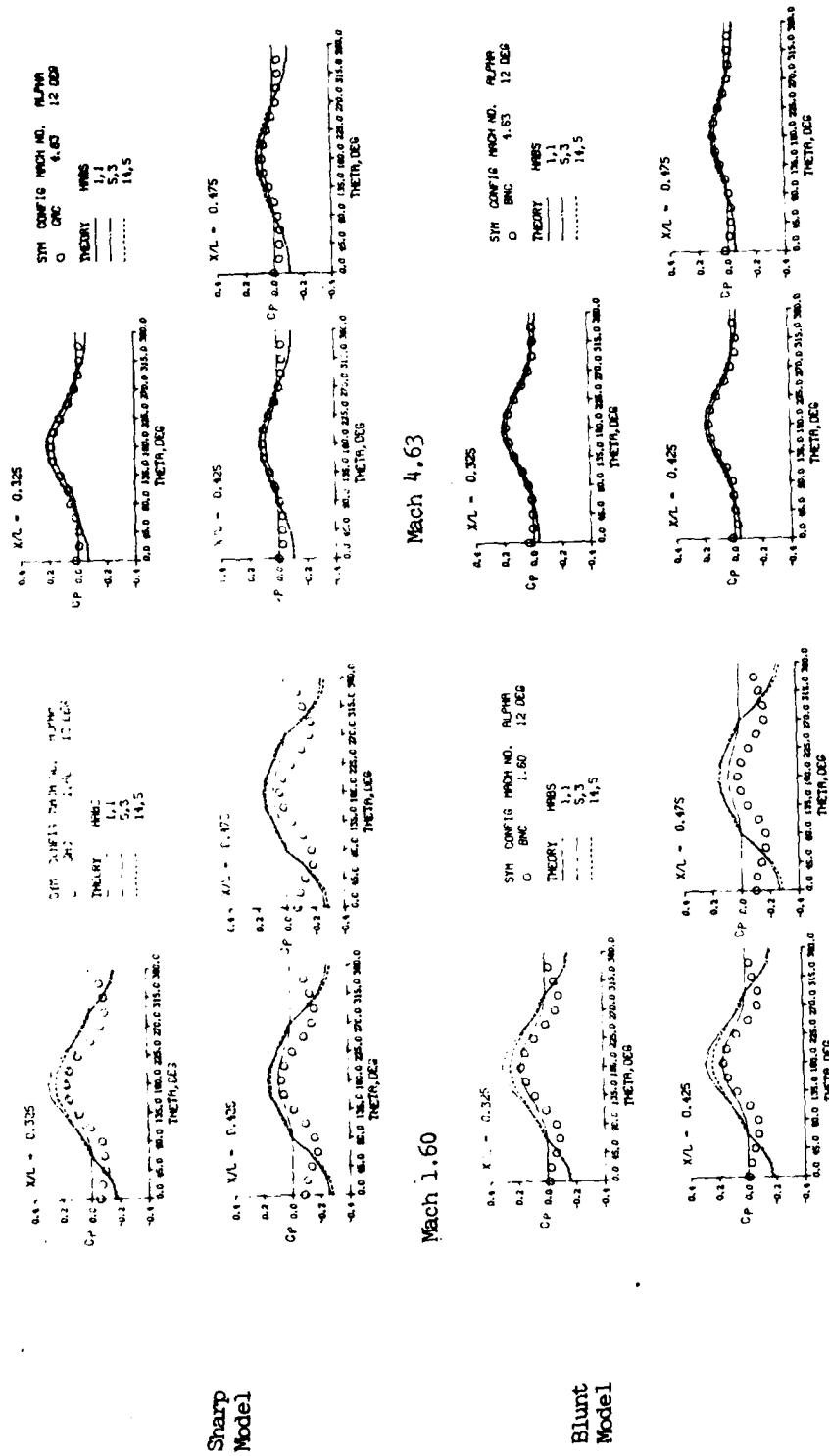


Figure 13. Concluded

Figure 14. Integrated HABP Local Force and Moment Distribution, $\alpha = 8^\circ$.

(a) $X/L = 0.075$ to 0.275 Figure 15. HABS Pressure Prediction Comparisons at $\alpha = 12^\circ$.



(b) $X/L = 0.325$ to 0.475

Figure 15. Continued

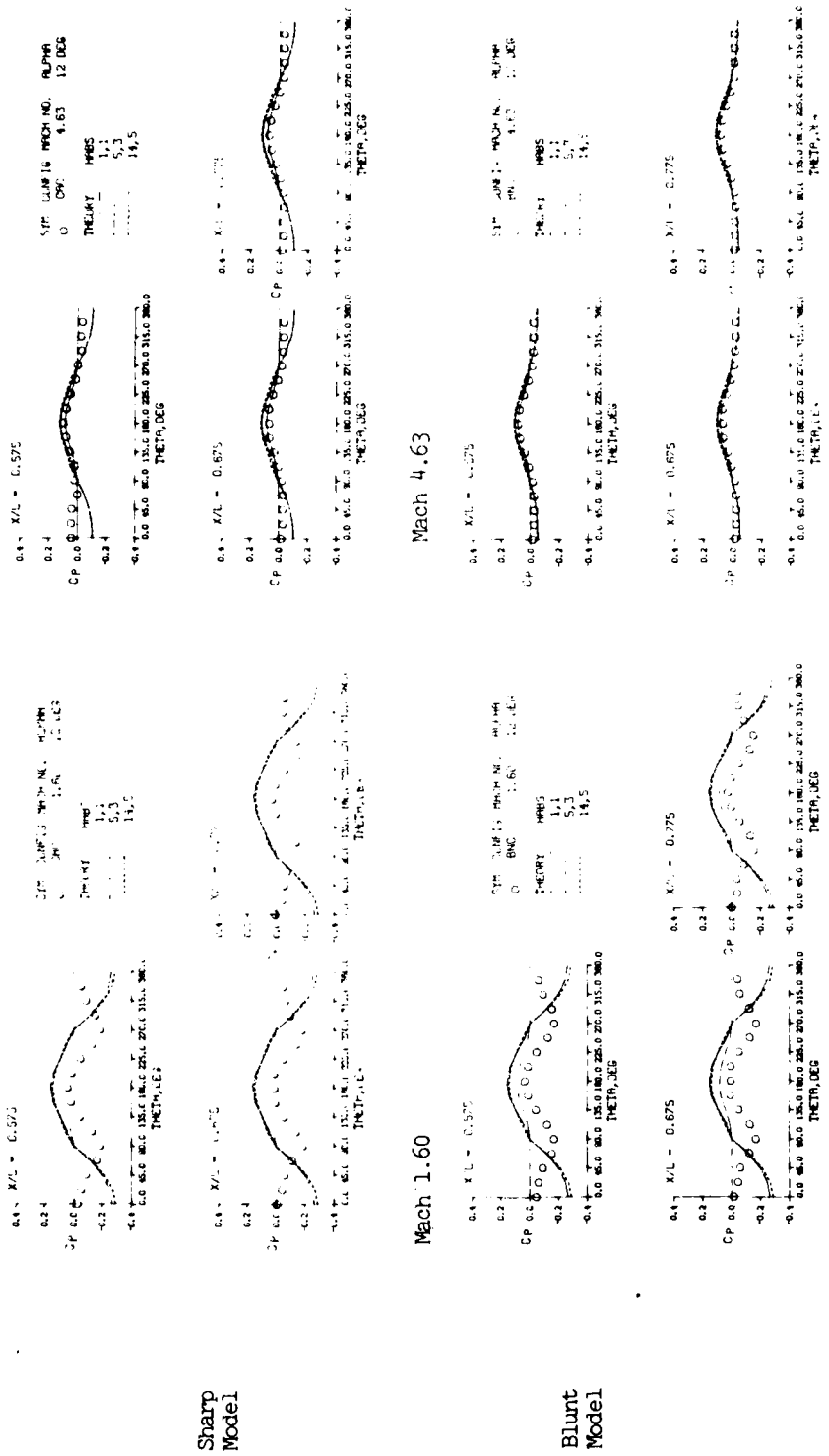


Figure 15. Continued

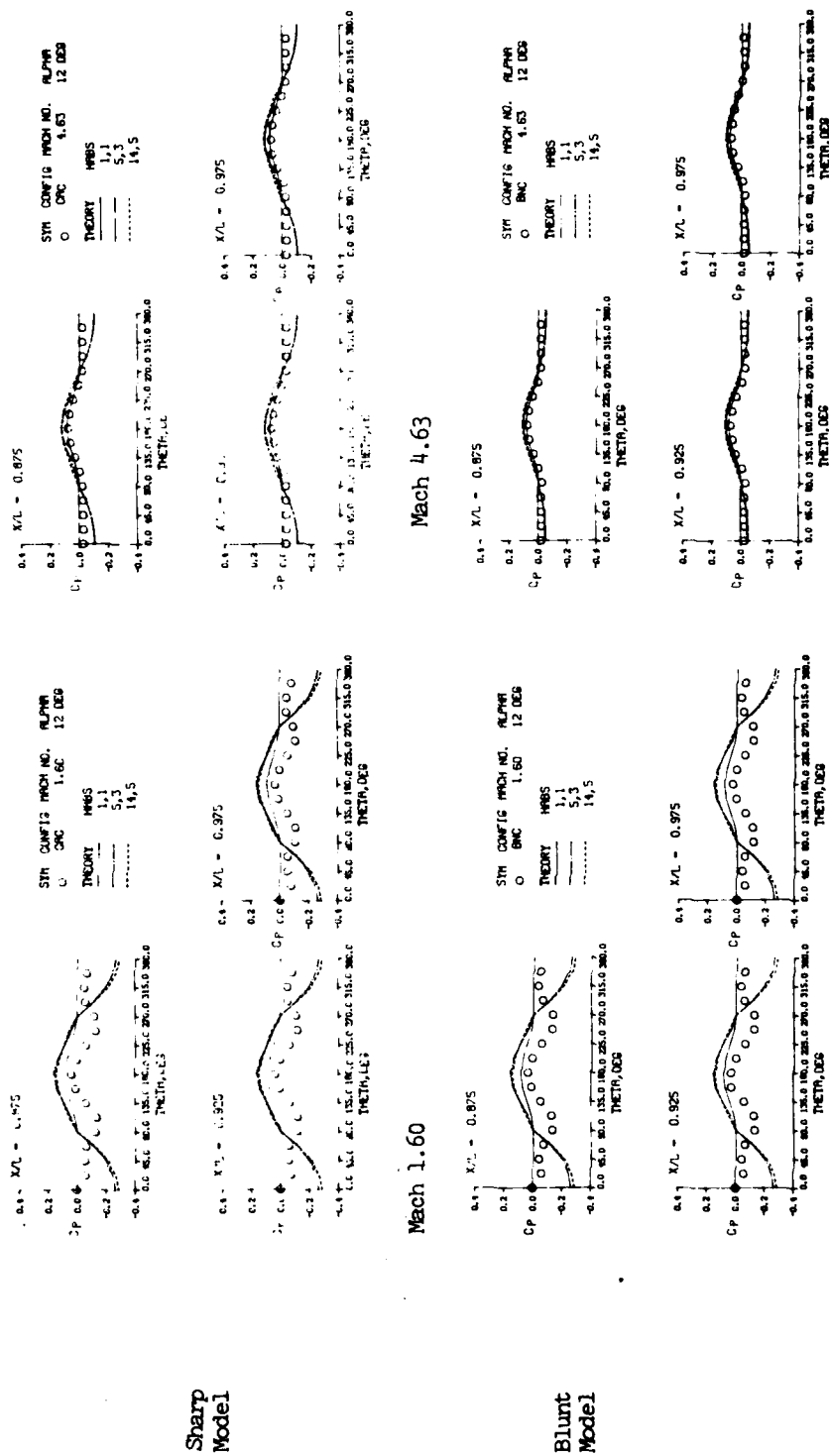
(d) $X/L = 0.875$ to 0.975

Figure 15. Concluded

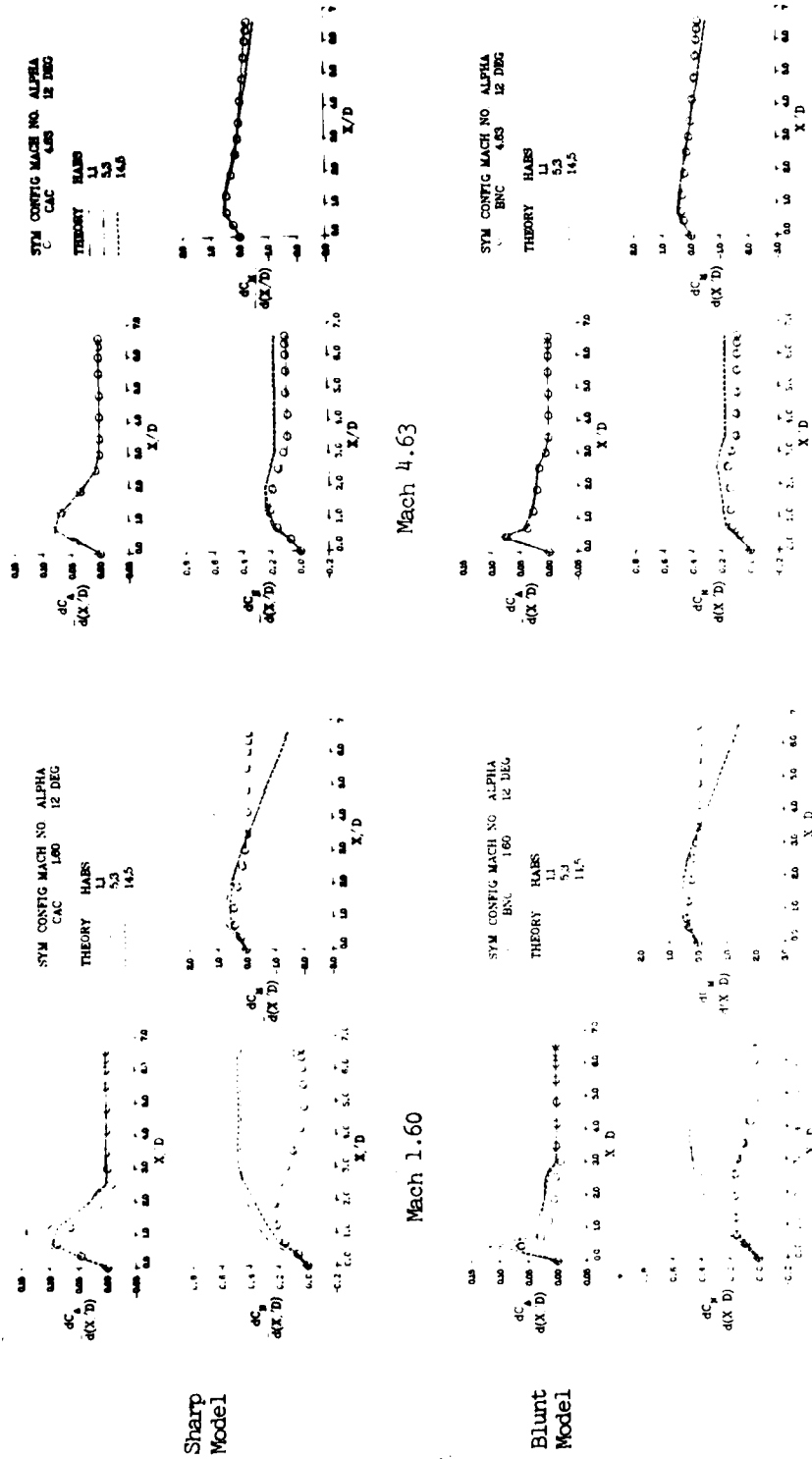


Figure 16. Integrated HABP Local Force and Moment Distribution, Alpha = 12 Degrees.

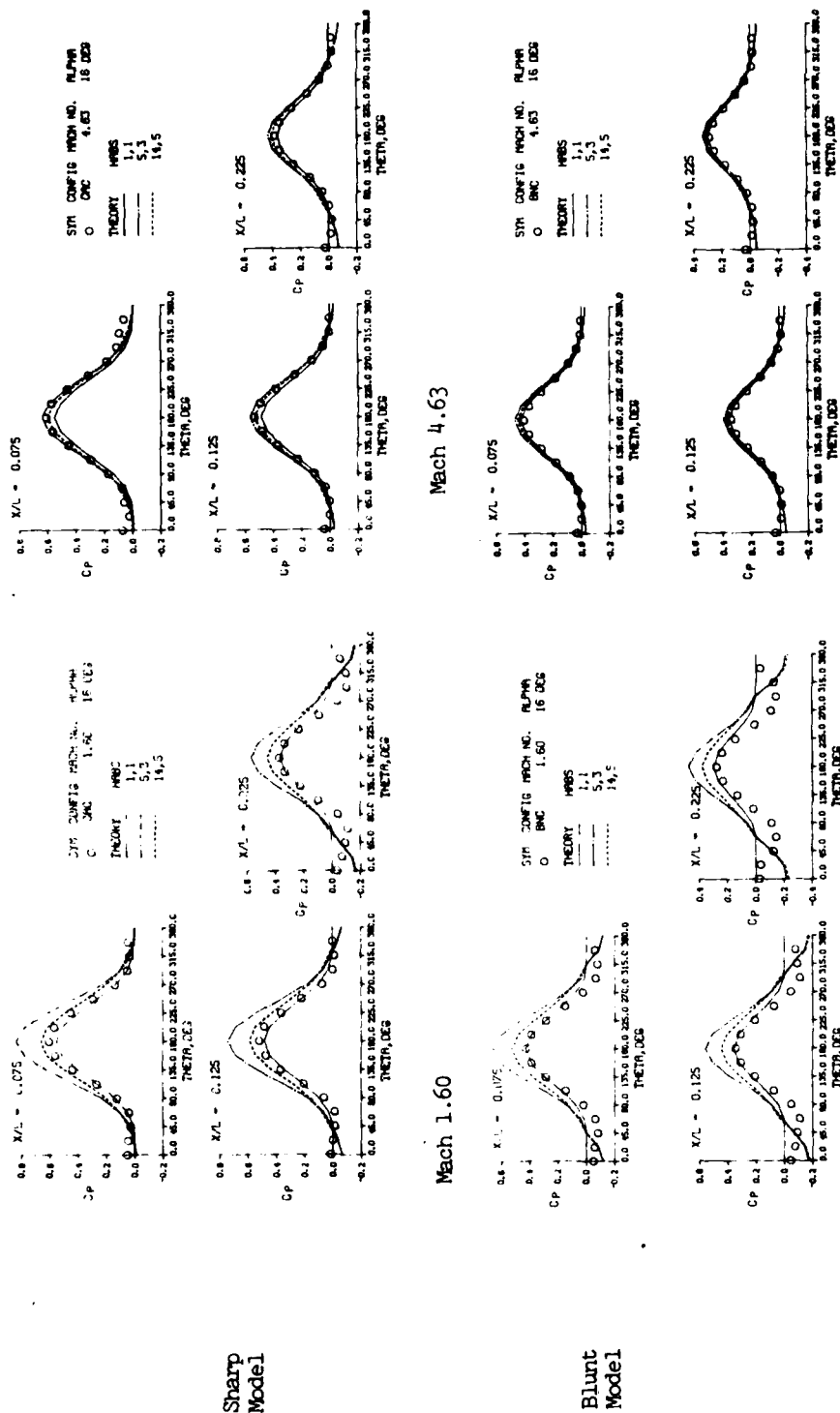
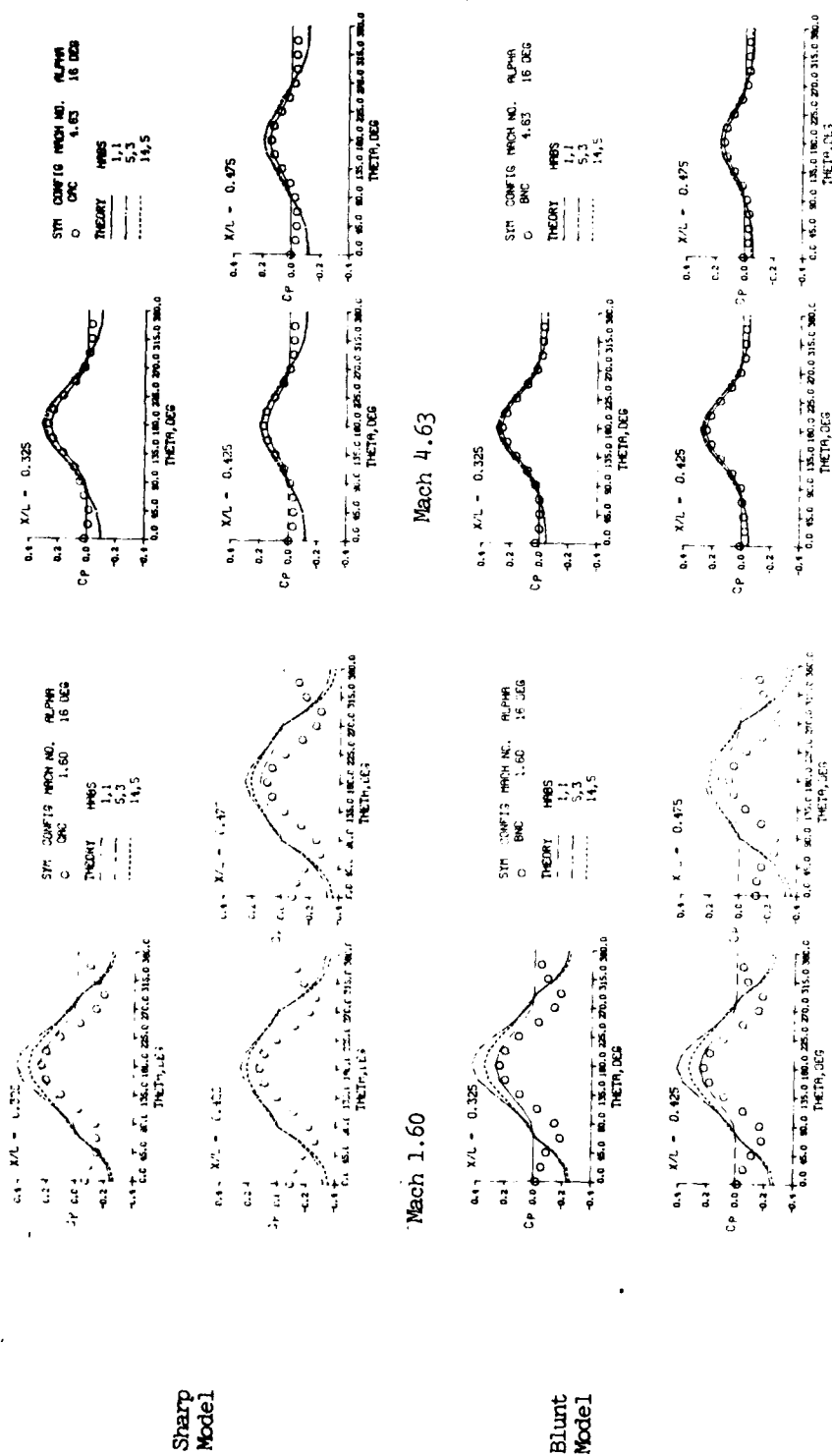


Figure 17. HARP Pressure Comparisons at Alpha = 16 Degrees.



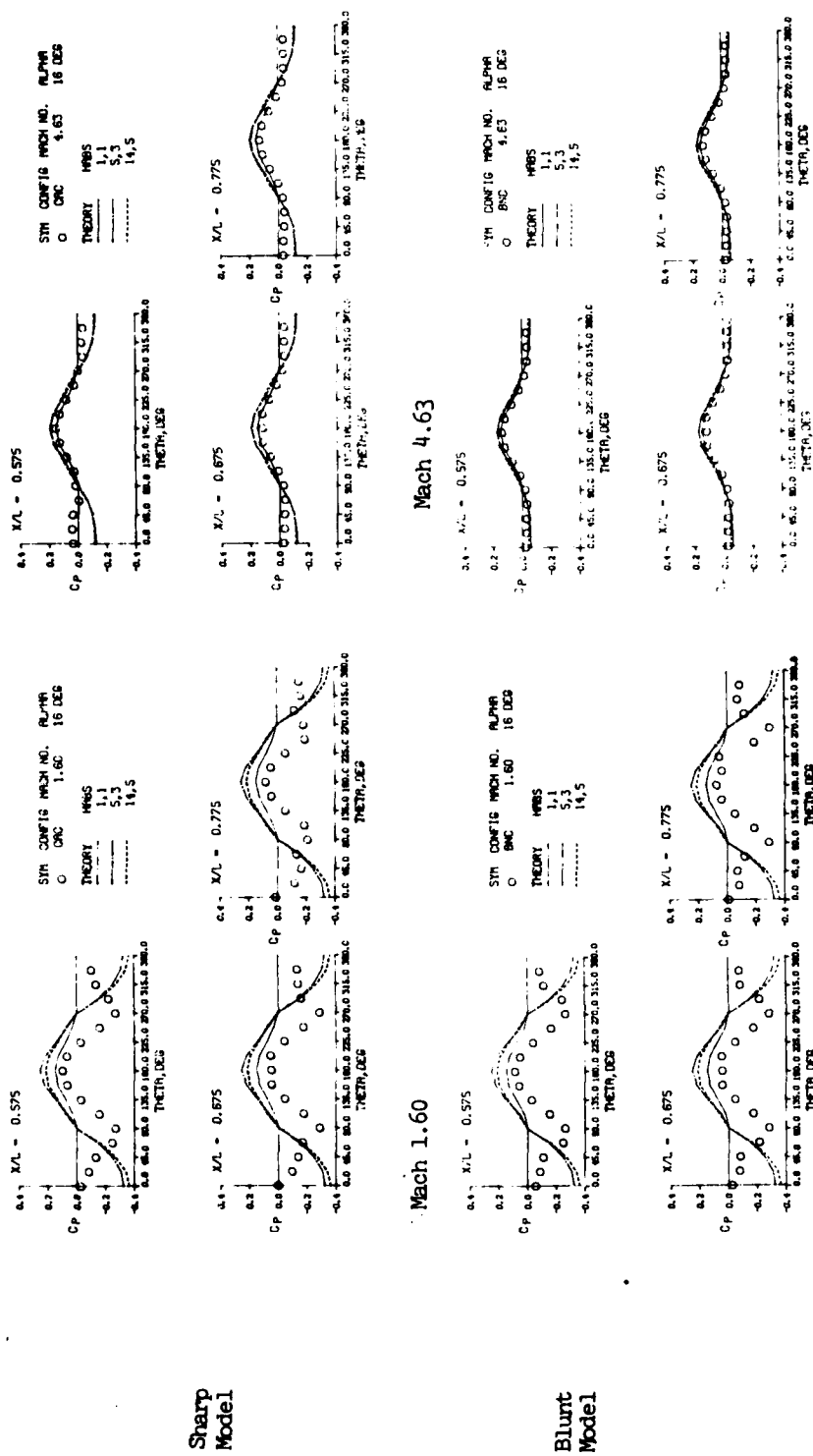
(c) $X/L = 0.575$ to 0.775

Figure 17. Continued

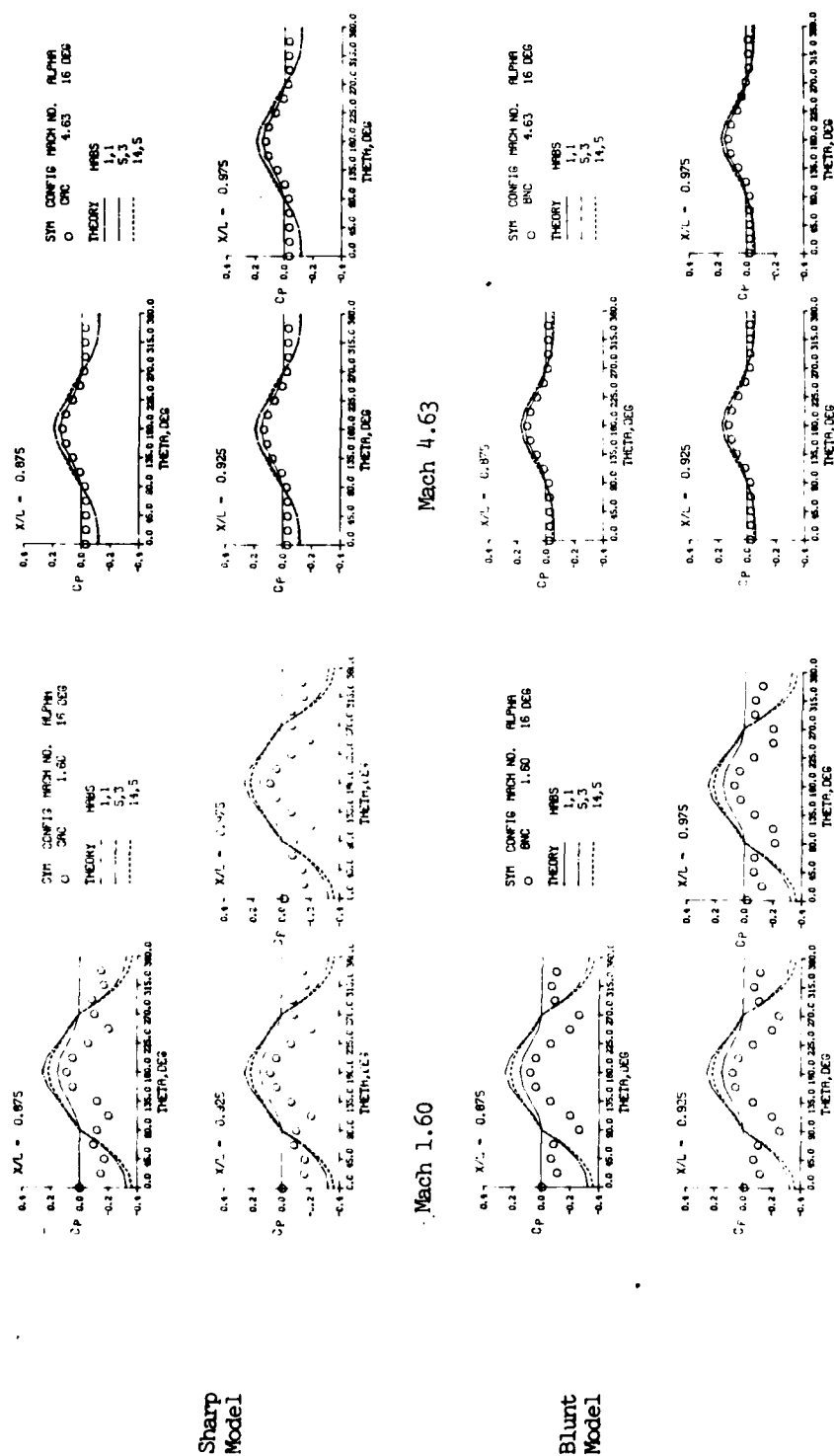


Figure 17. Concluded

(d) $X/L = 0.875$ to 0.975

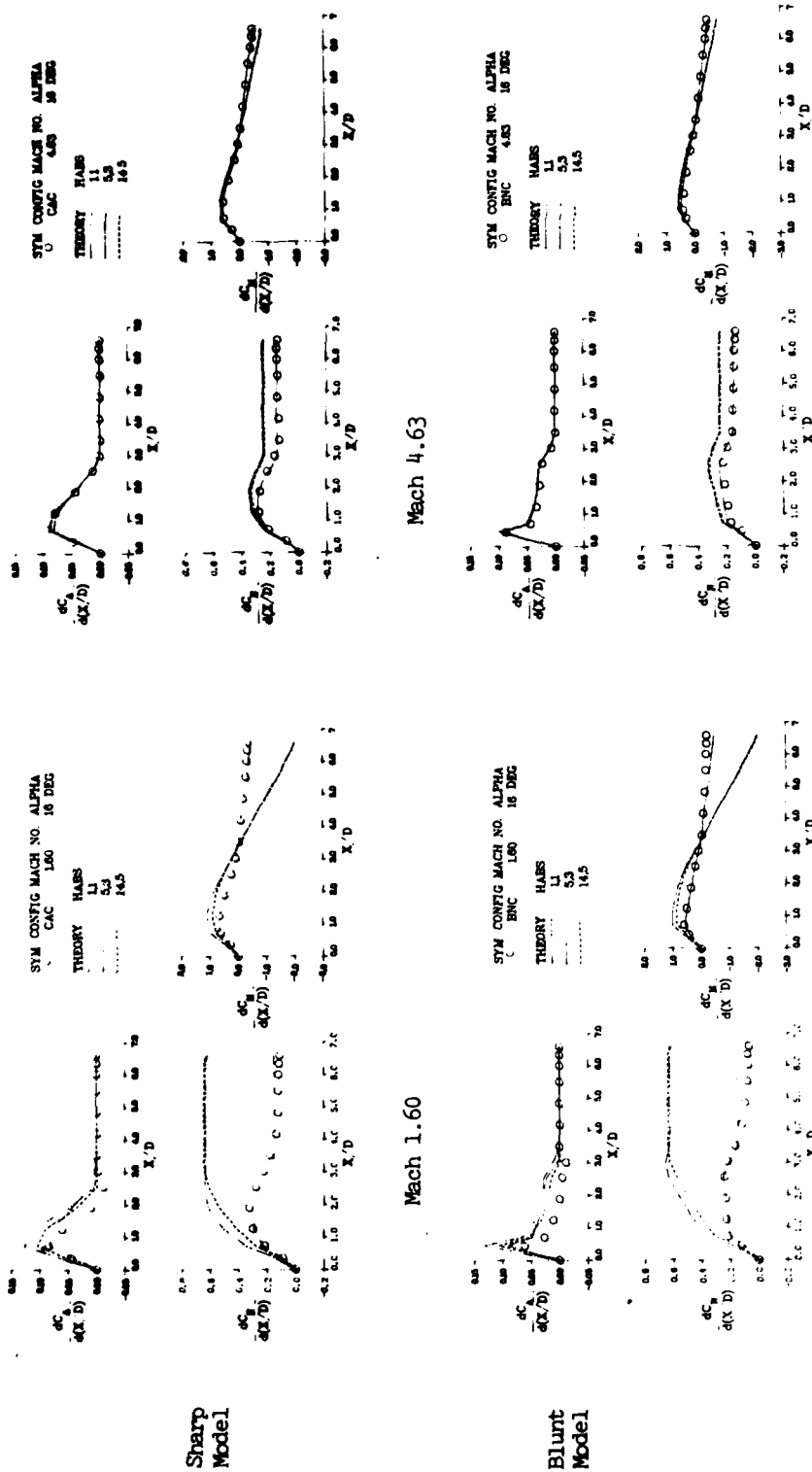


Figure 18. Integrated HAP Local Force and Moment Distribution, $\alpha = 16$ Degrees.

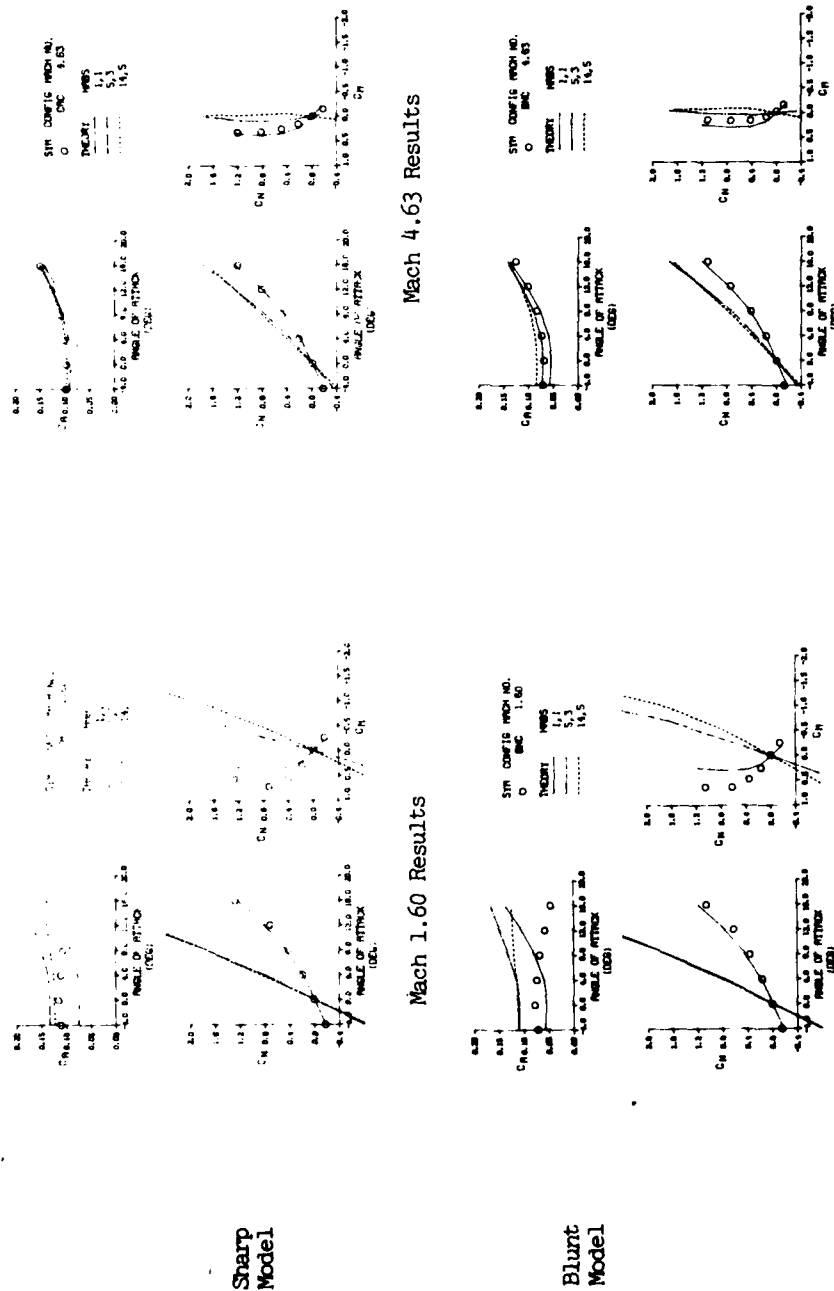


Figure 19. Total Force and Moment HABP Comparisons with Experiment at Various Angles of Attack. Effect of Mach Number and Nose Bluntness.

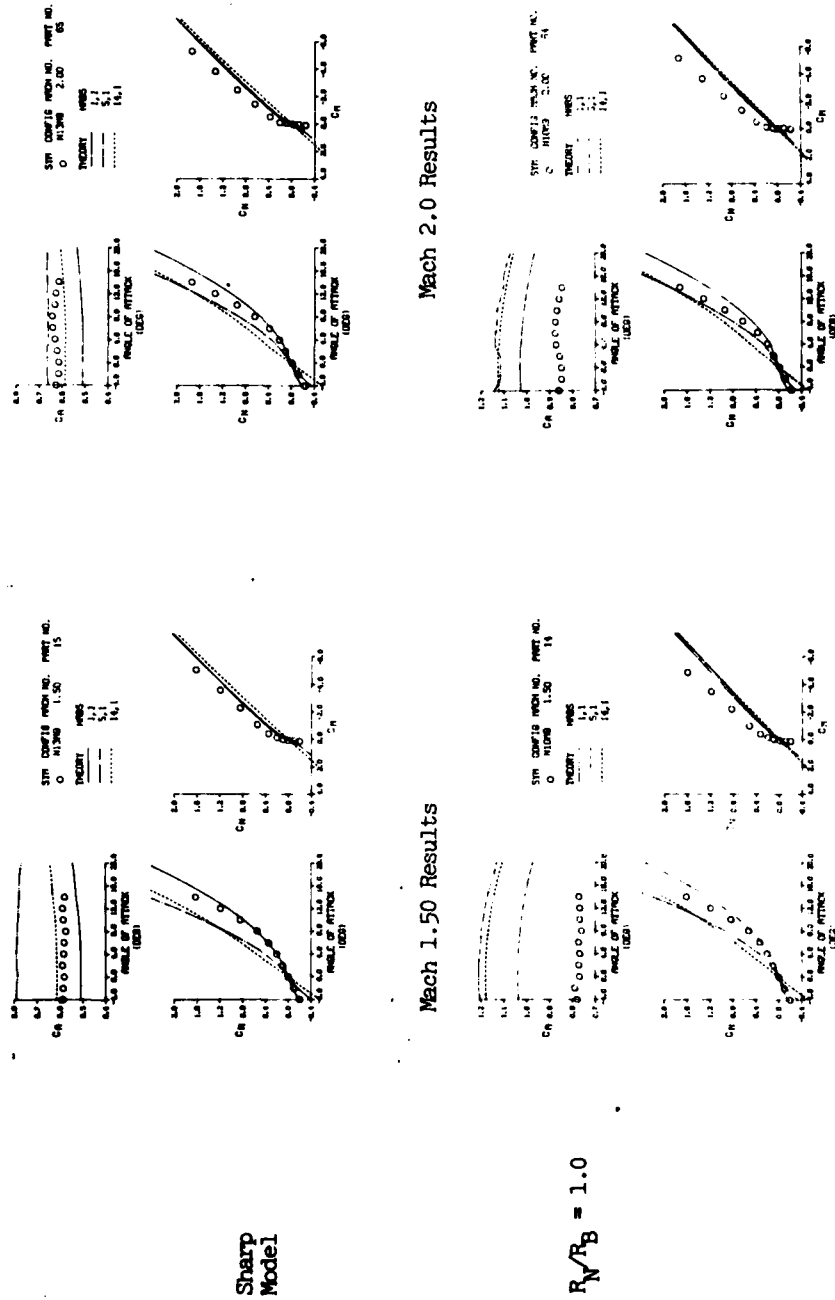
(a) $R_N/R_B = 0.0$ and 1.0 , $M = 1.5$ and 2.0

Figure 20. Effect of Nose Bluntness and Mach Number on Total Force and Moment HABP Comparisons. Nose Fineness Ratio = 1.0.

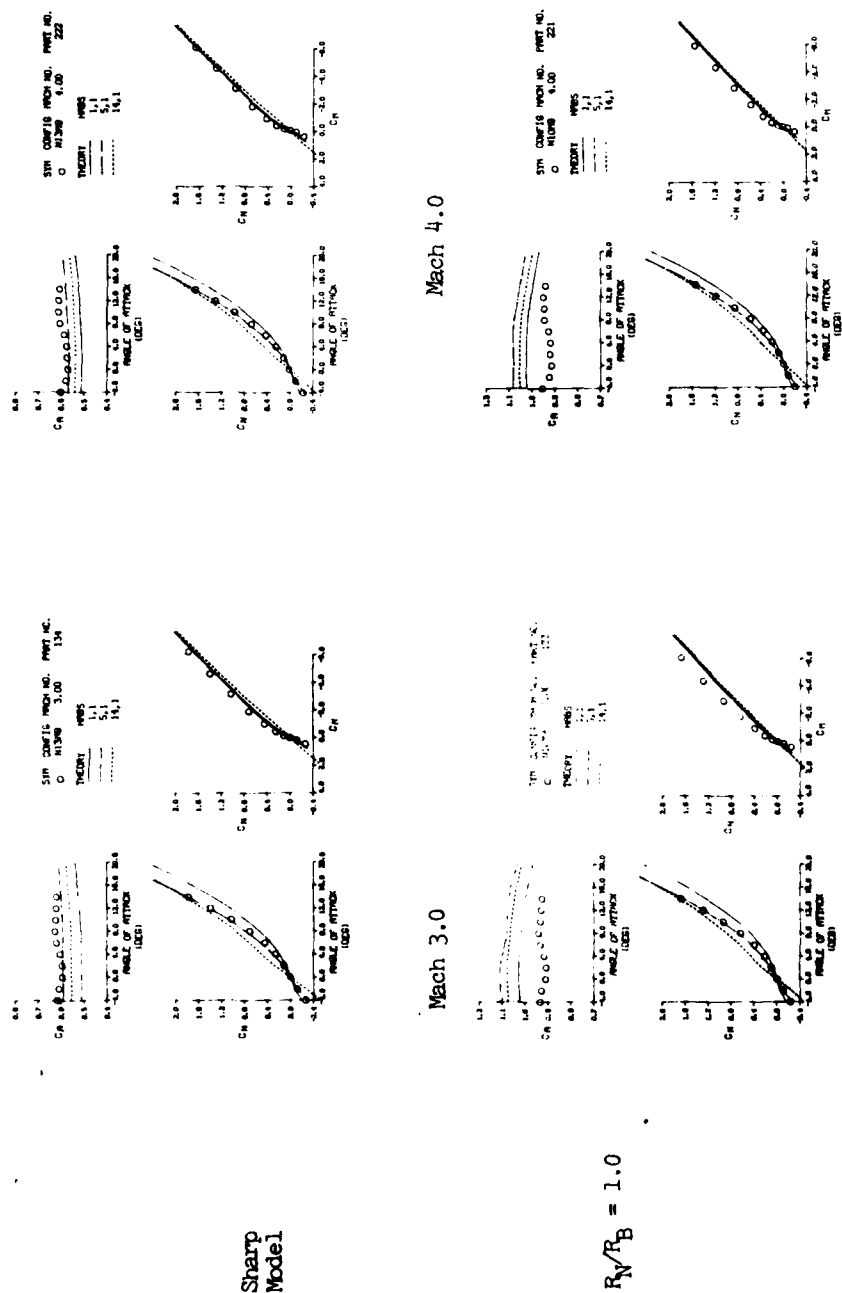
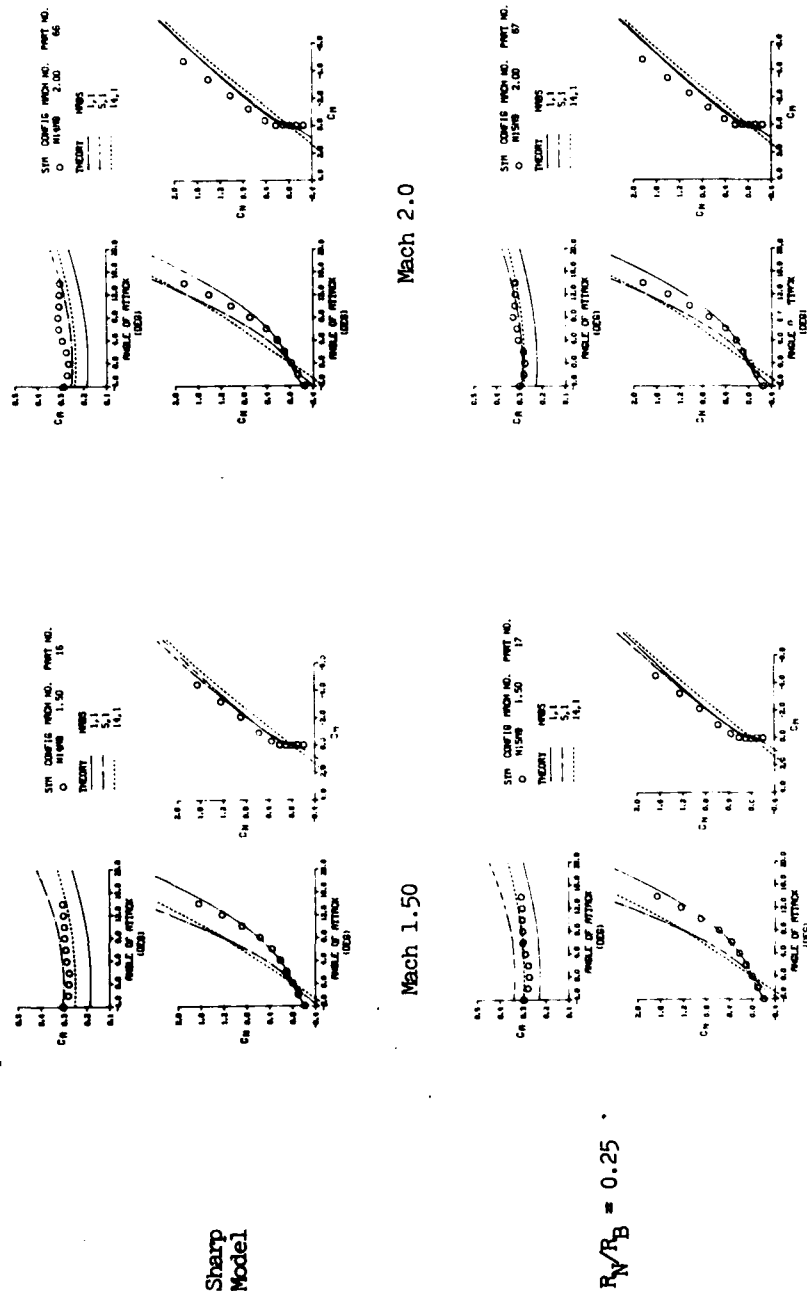


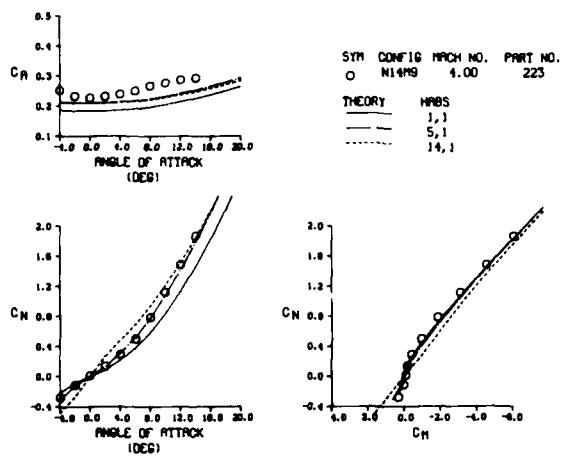
Figure 20. Concluded



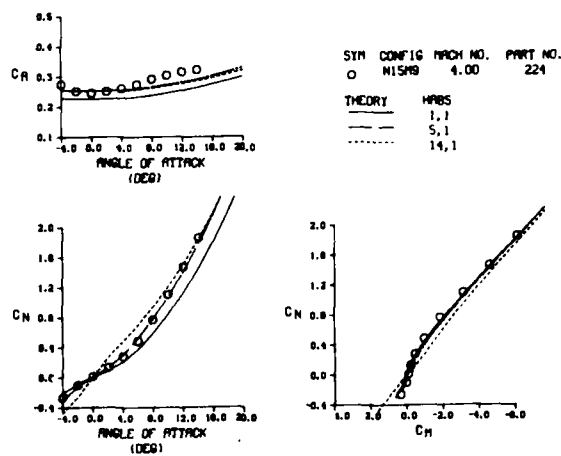
(a) $R_N/R_B = 0.0$ and 0.25 , $M = 1.5$ and 2.0

Figure 21. HABP Force and Moment Comparisons for the 2.0 Nose Fineness Ratio Geometry. Effects of Nose Bluntness and Mach Number.

Sharp
Model



$R_N/R_B = 0.25$



(b) $R_N/R_B = 0.0$ and 0.25 , $M = 4.0$

Figure 21. Continued

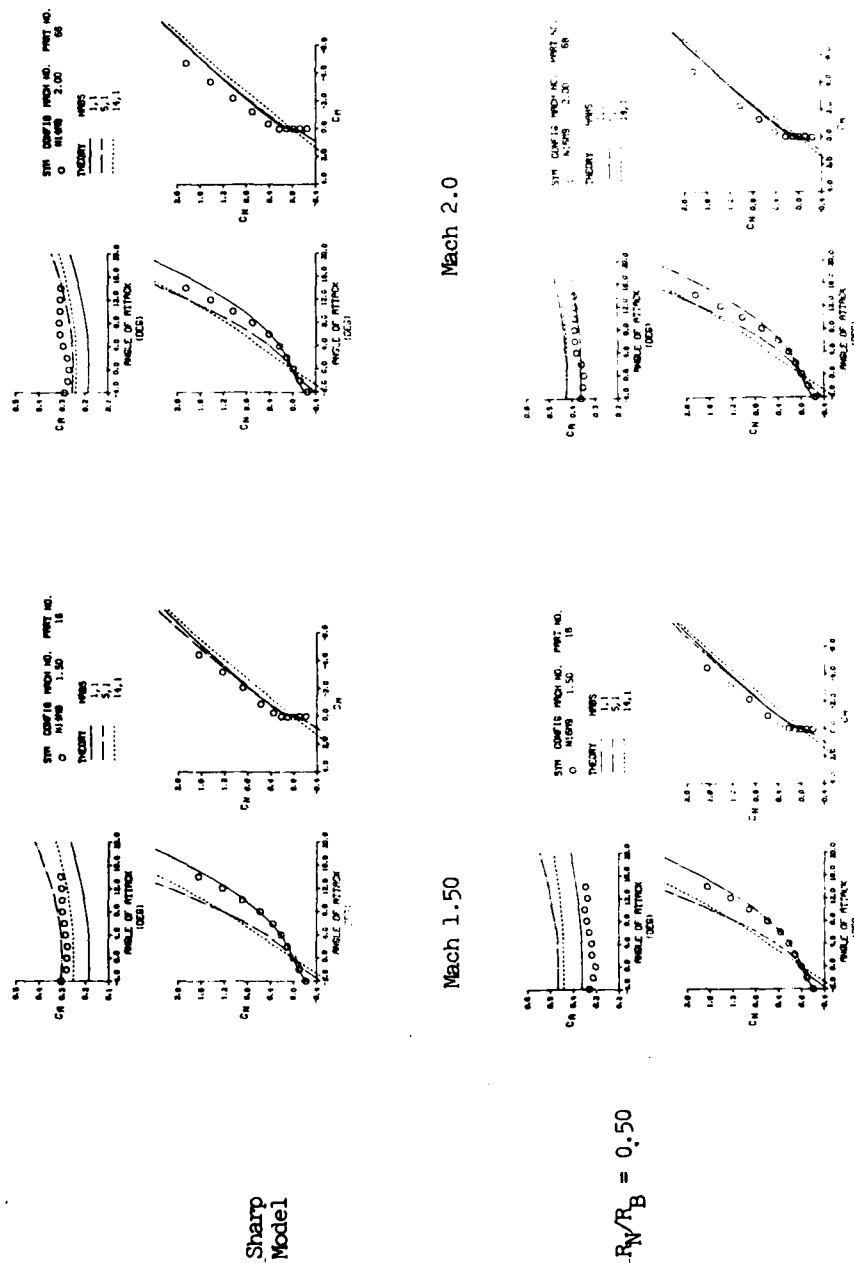
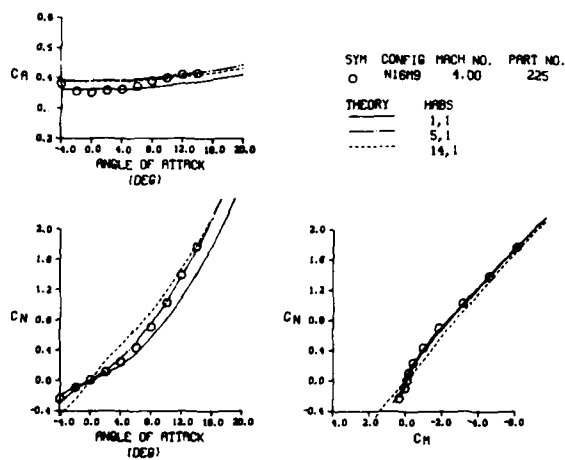
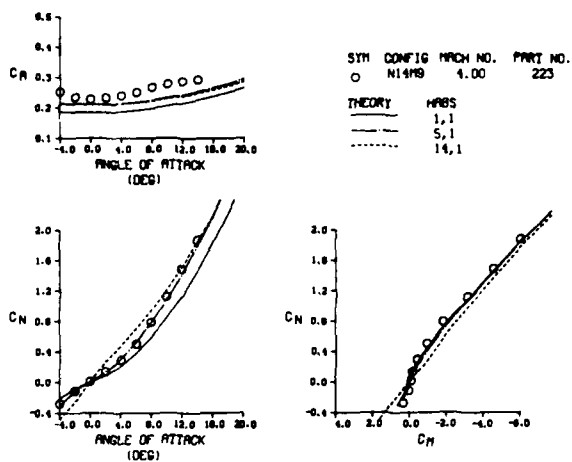


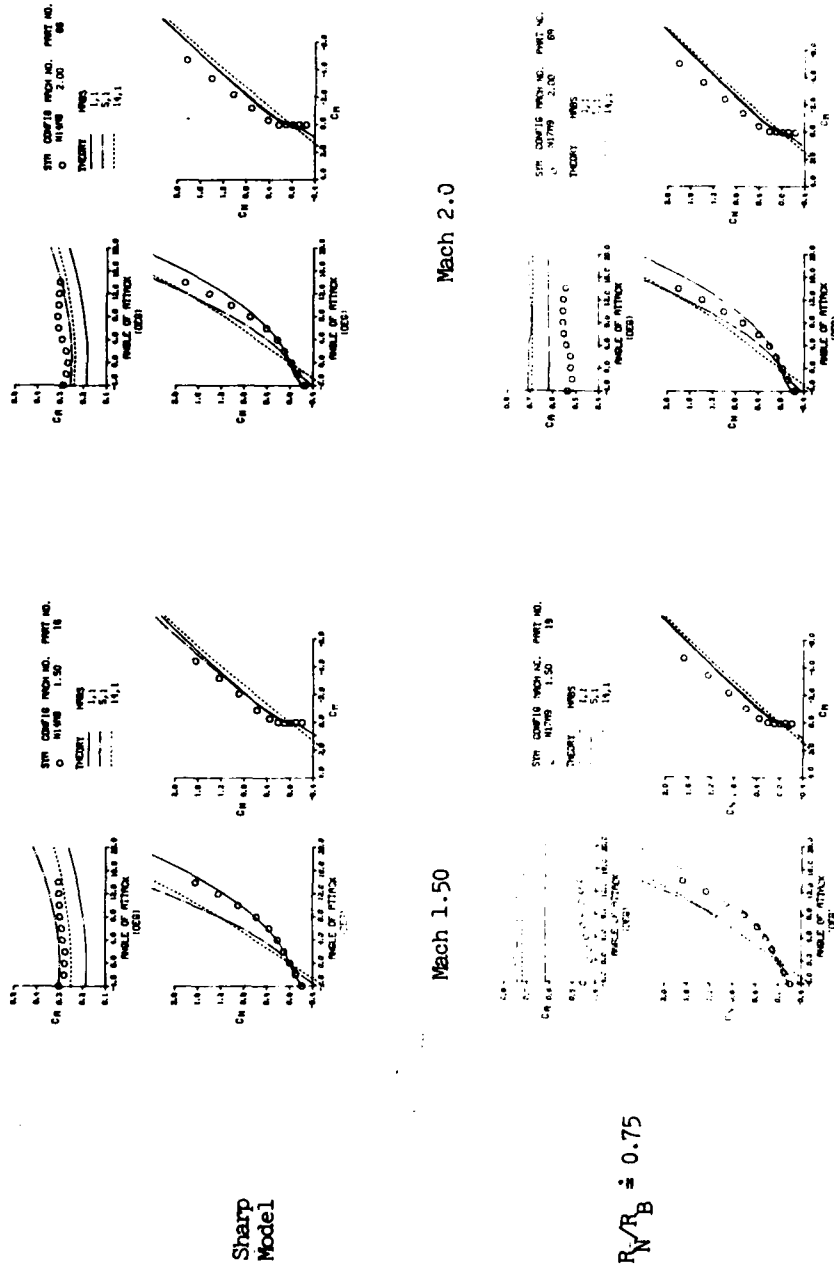
Figure 21. Continued

Sharp
Model



(d) $R_N/R_B = 0.0$ and 0.50 , $M = 4.0$

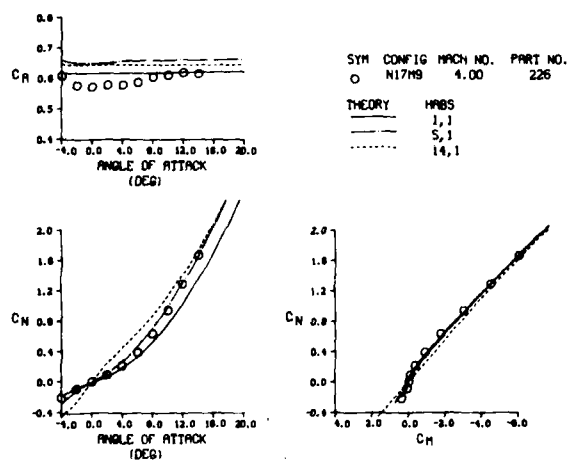
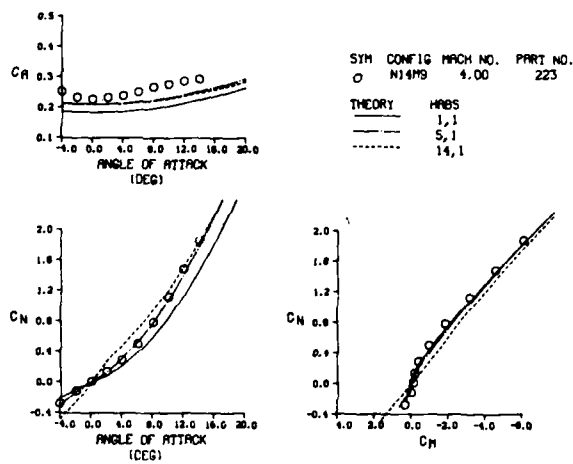
Figure 21. Continued



(e) $R_N/R_B = 0.0$ and 0.75 , $M = 1.50$ and 2.0

Figure 21. Continued

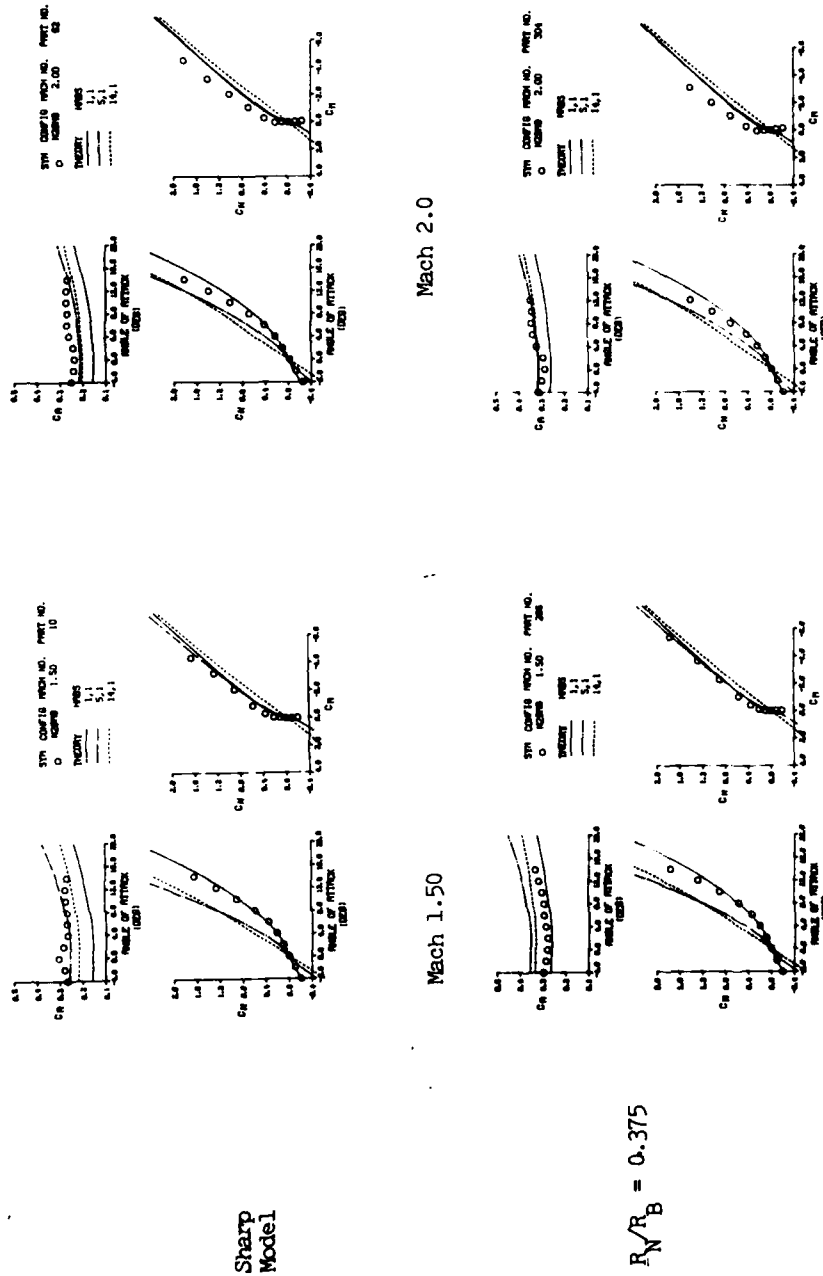
Sharp
Model



$$R_N/R_B = 0.75$$

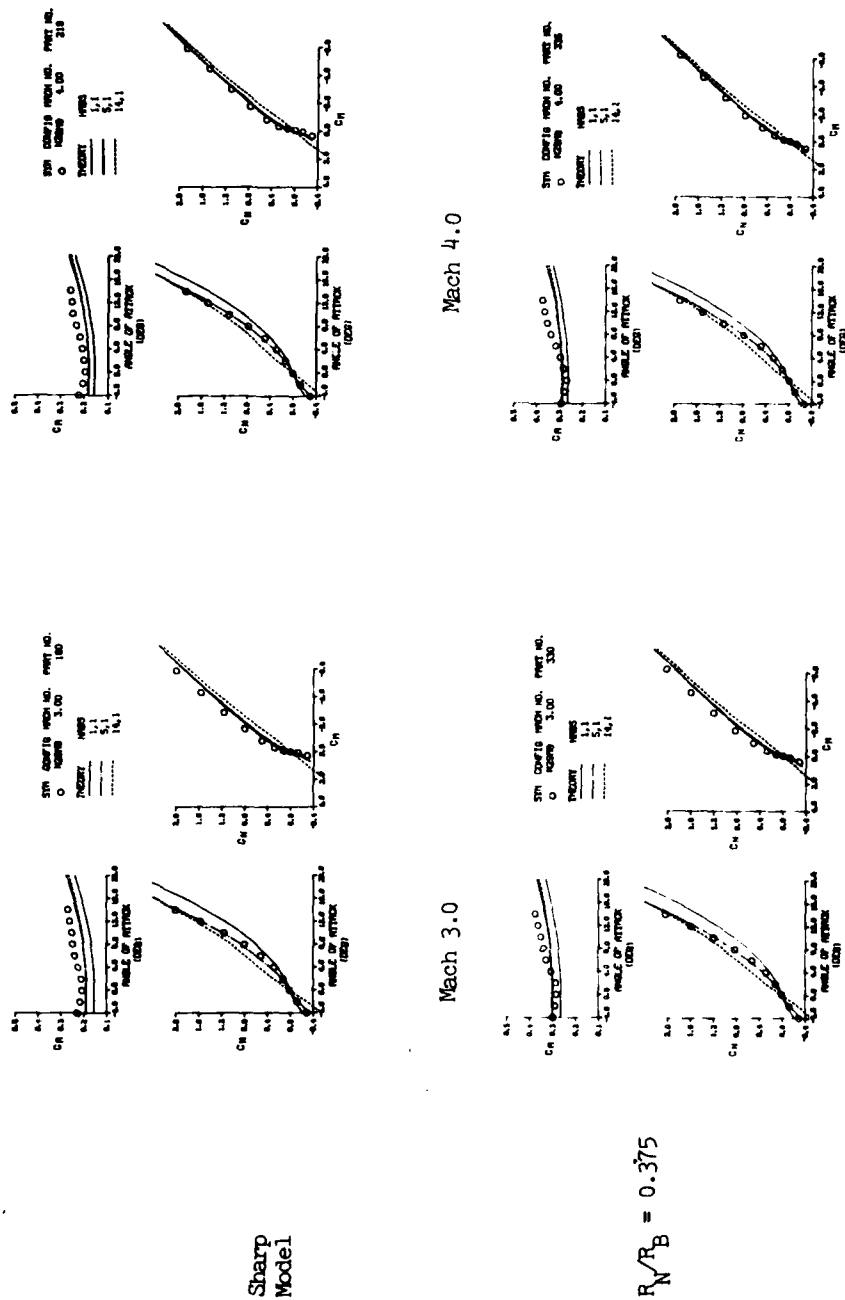
(f) $R_N/R_B = 0.0$ and 0.75 , $M = 4.0$

Figure 21. Concluded



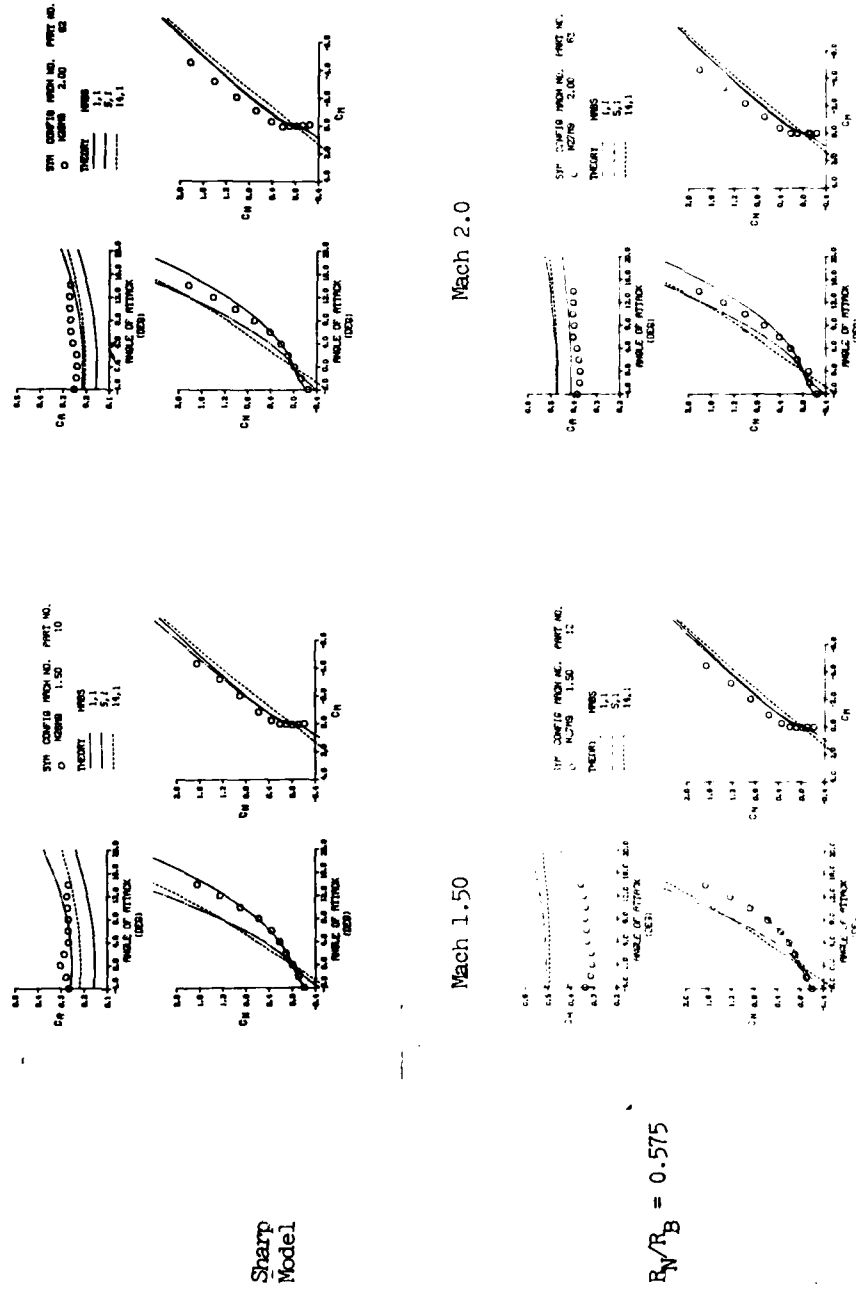
(a) $R_N/R_B = 0.0$ and 0.375 , $M = 1.5$ and 2.0

Figure 22. HABP Force and Moment Comparisons for Nose Fineness Ratio = 2.25.



(b) $R_N/R_B = 0.0$ and 0.375 , $M = 3.0$ and 4.0

Figure 22. Continued



(c) $R_N/R_B = 0.0$ and 0.575 , $M = 1.50$ and 2.0

Figure 22. Continued

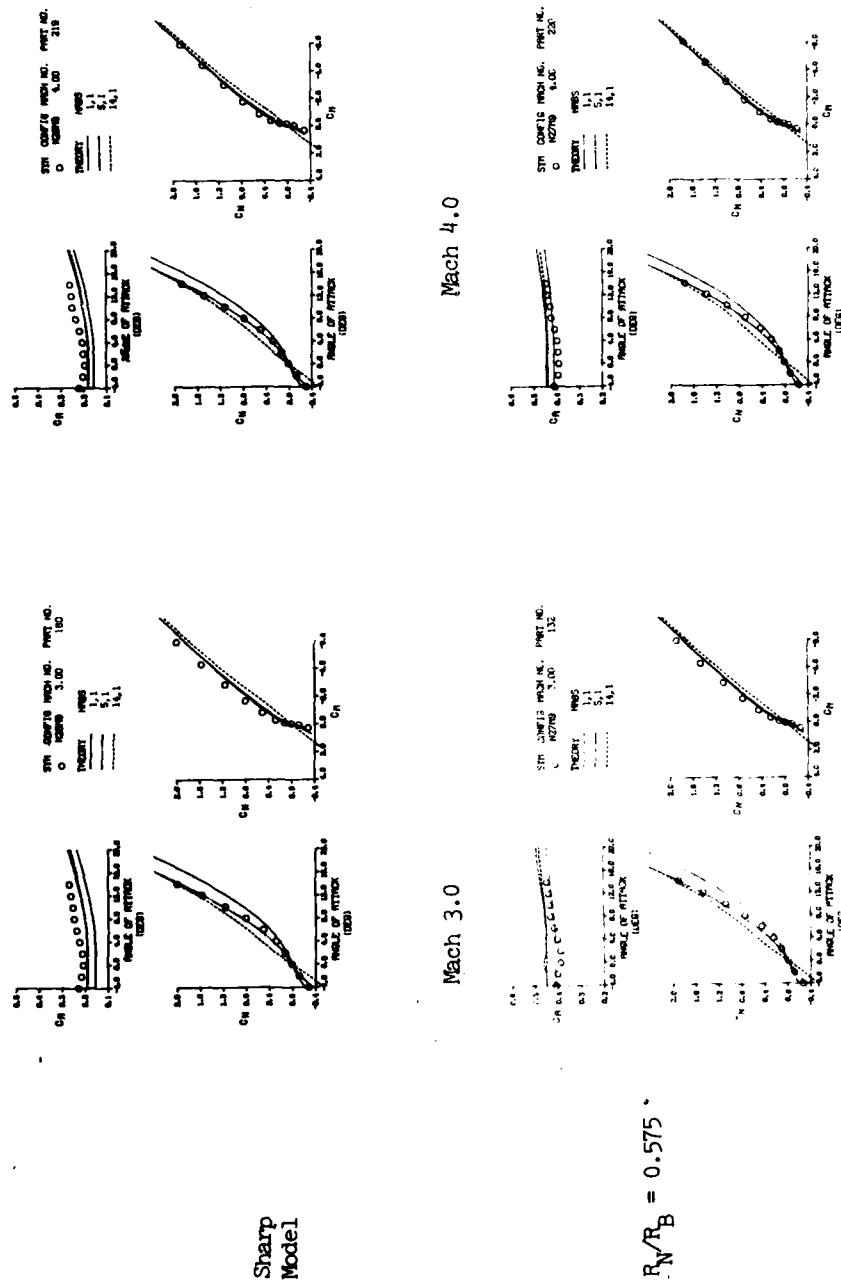
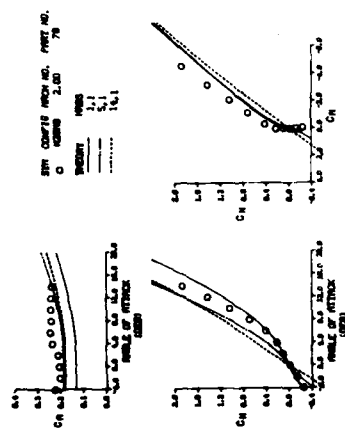
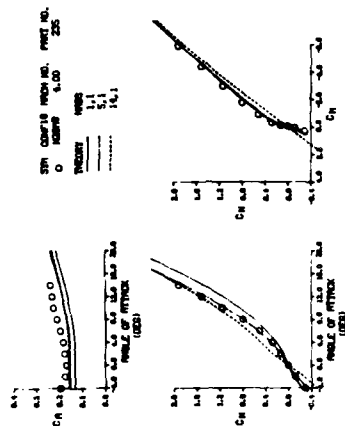


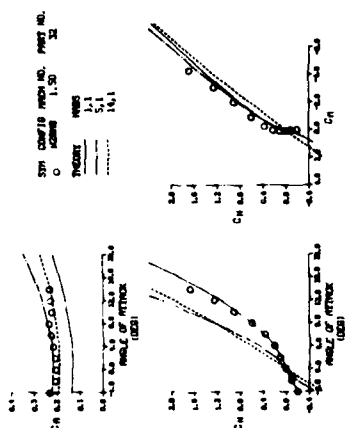
Figure 22. Concluded



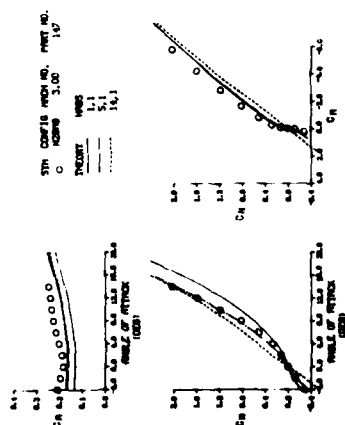
Mach 2.0



Mach 4.0



Mach 1.50



Mach 3.0

Sharp
Model

Sharp
Model

Figure 23. HABP Force and Moment Comparisons for the 2.5 Nose Fineness Ratio Geometry. Sharp Nose

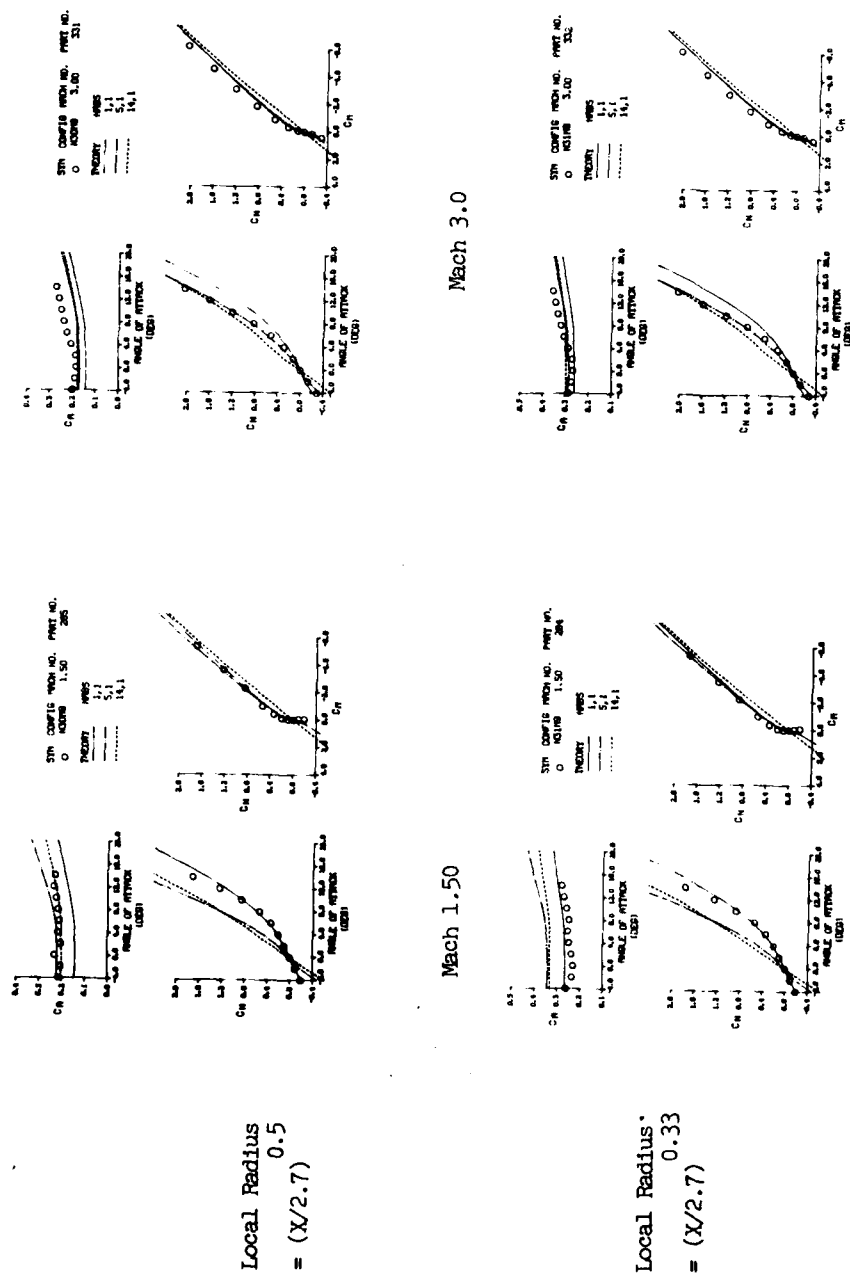
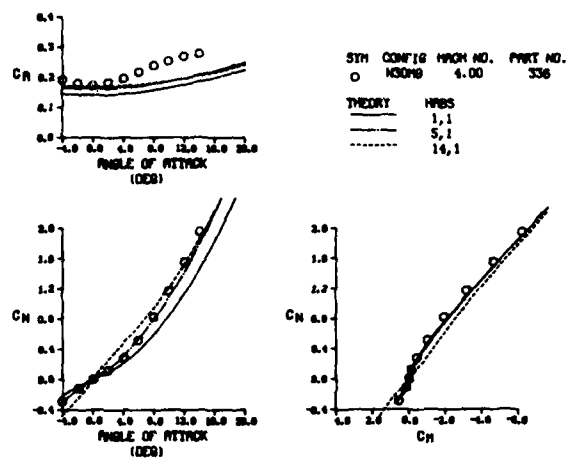
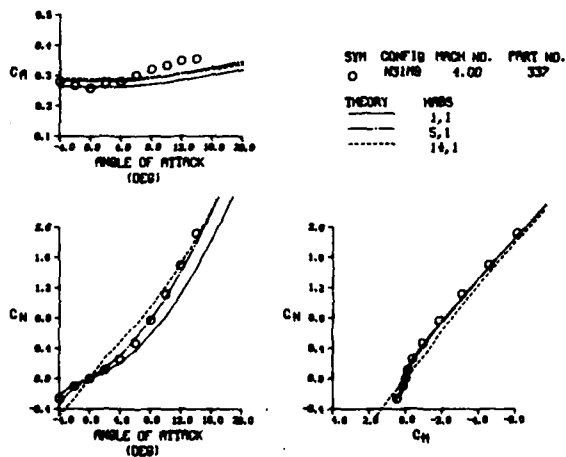


Figure 24. HABP Force and Moment Comparisons for the Power Series Nose Geometry.

Local Radius
 0.5
 $= (X/2.7)$

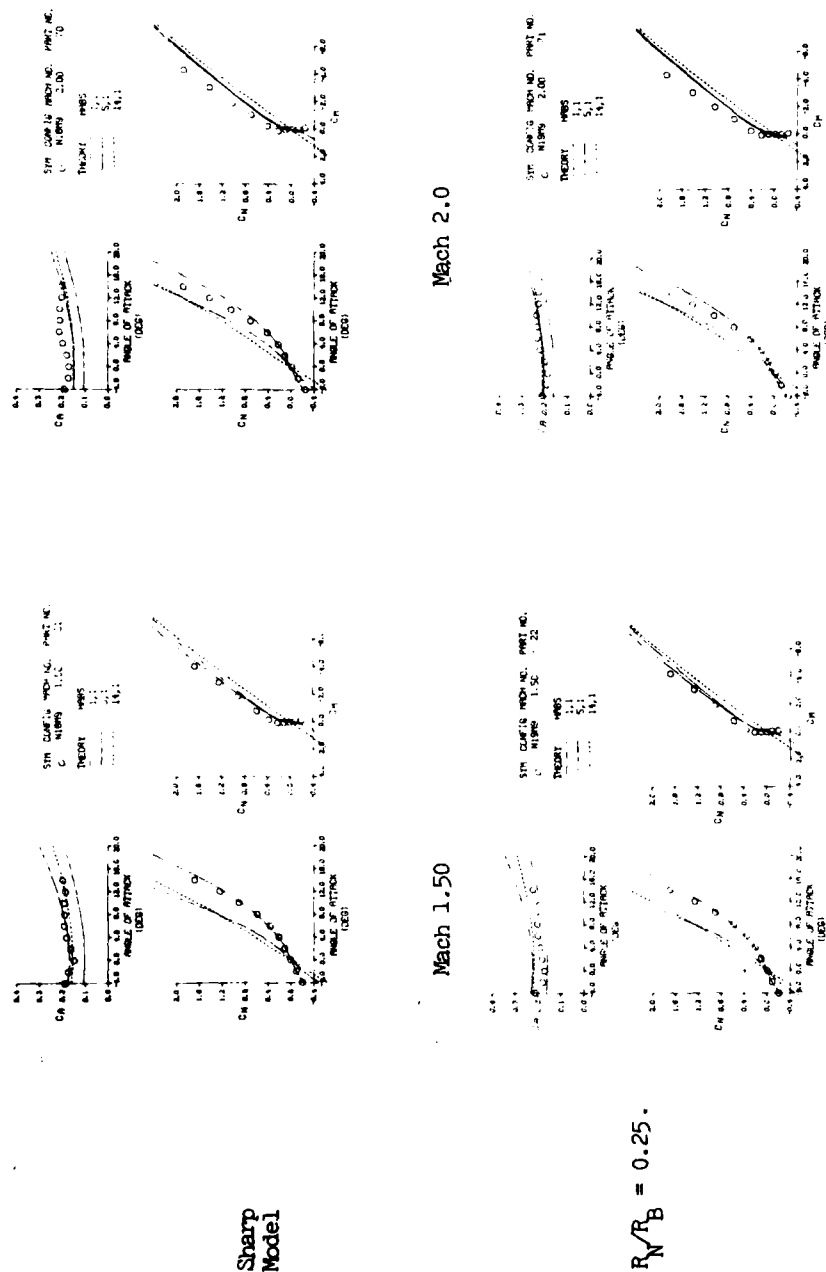


Local Radius
 0.33
 $= (X/2.7)$



(b) Mach 4.0

Figure 24. Concluded



(a) $R_N/R_B = 0.0$ and 0.25 , $M = 1.5$ and 2.0

Figure 25. HABP Force and Moment Comparisons for the 3.0 Fineness Ratio Nose.

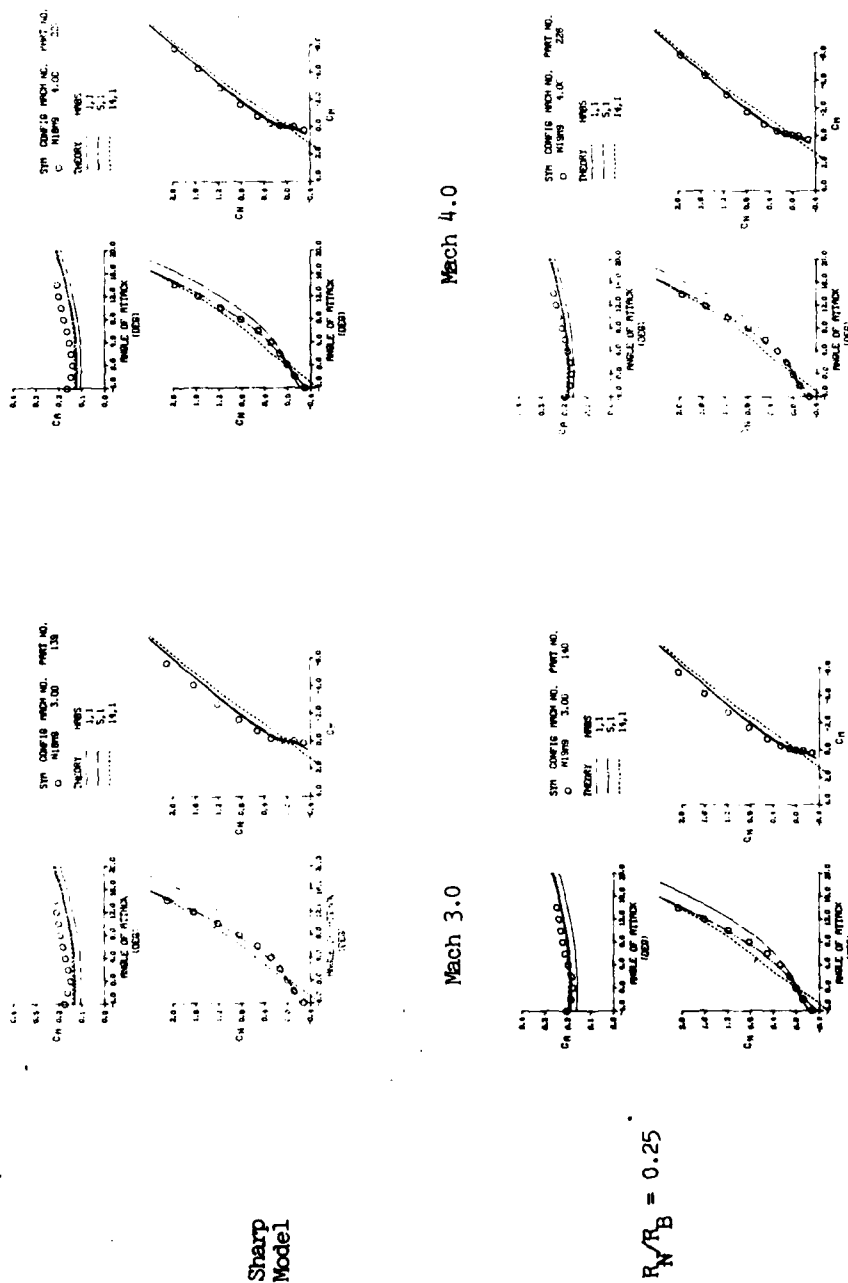
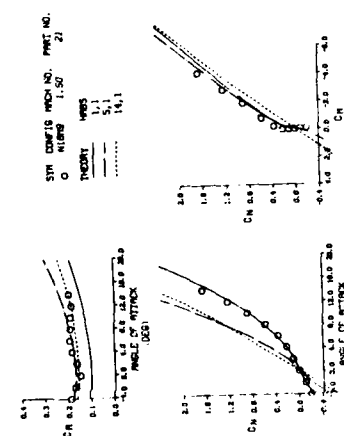
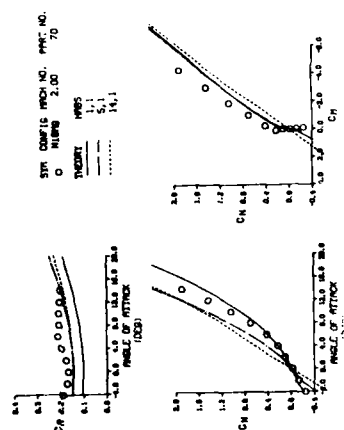
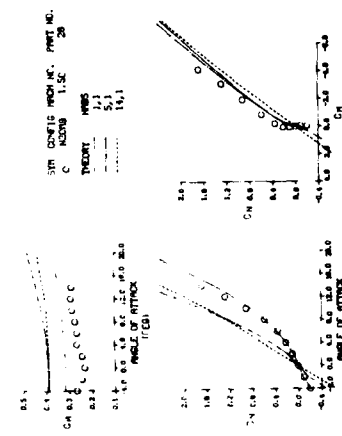
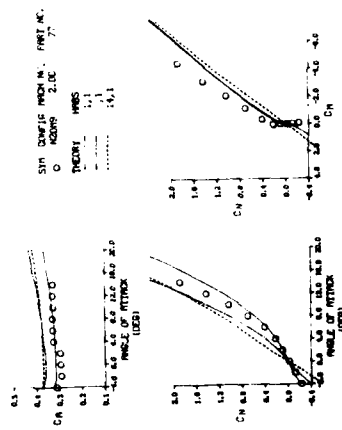


Figure 25. Continued



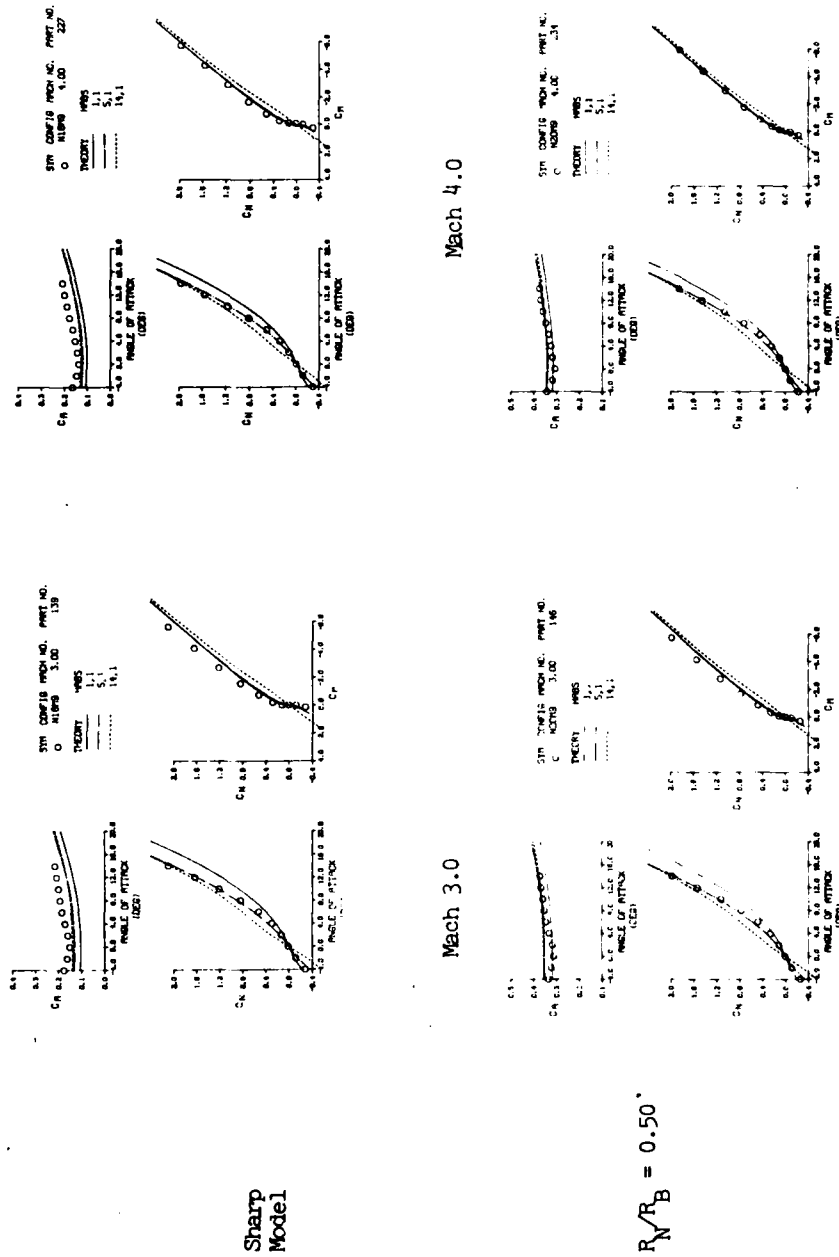
Sharp
Model

Mach 2.0


$$R_N/R_B = 0.50.$$

(c) $R_N/R_B = 0.0$ and 0.50 , $M = 1.5$ and 2.0

Figure 25. Continued



(d) $R_N/R_B = 0.0$ and 0.50 , $M = 3.0$ and 4.0

Figure 25. Continued

AD-A106 065

AIR FORCE WRIGHT AERONAUTICAL LABS WRIGHT-PATTERSON AFB OH F/G 20/4
EVALUATION OF USSAERO AND HABP COMPUTER CODES FOR AERODYNAMIC P--ETC(U)
SEP 81 J I FLAHERTY
AFWAL-TR-81-3035

UNCLASSIFIED

NL

2 OF 2

AD-A
11 6325



END
DATE
FILMED
11-81
DTIC

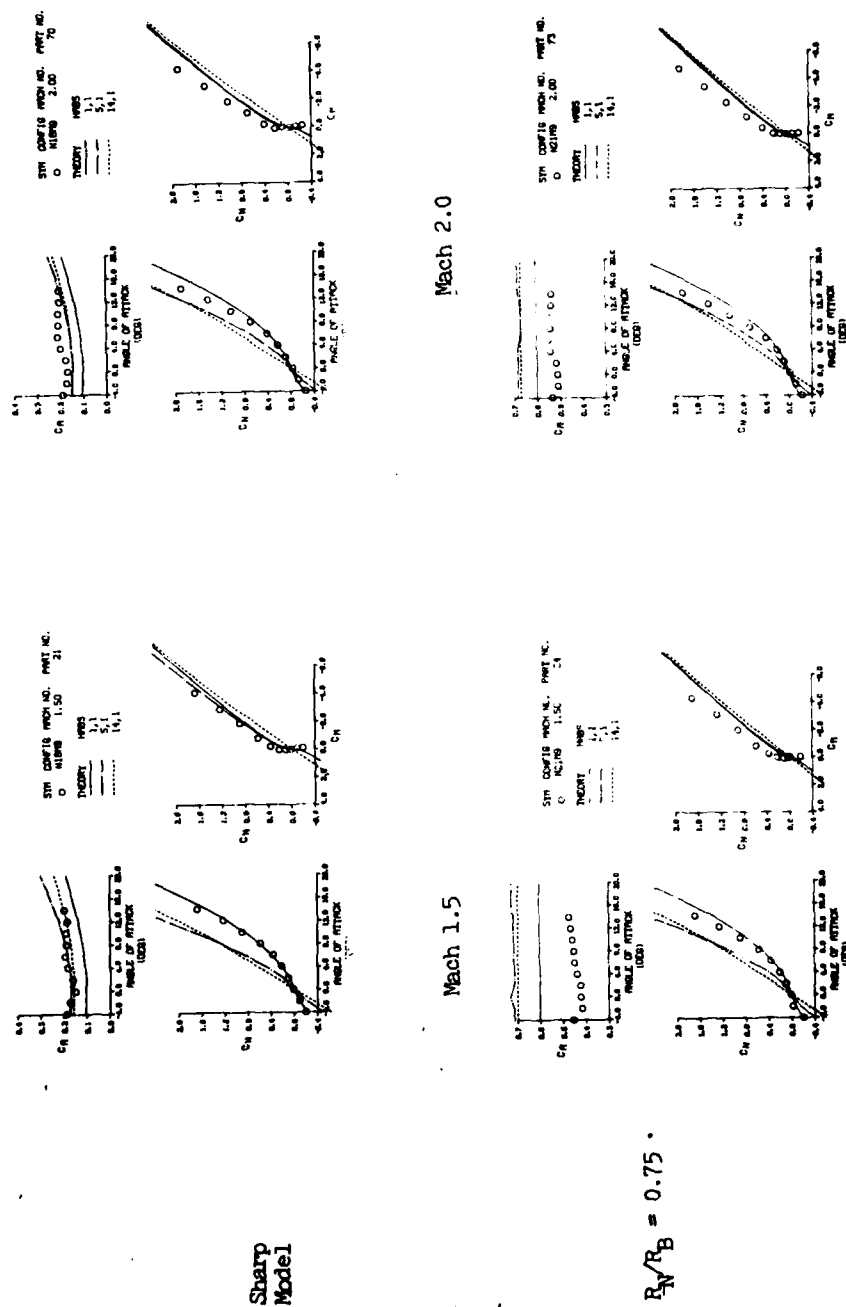
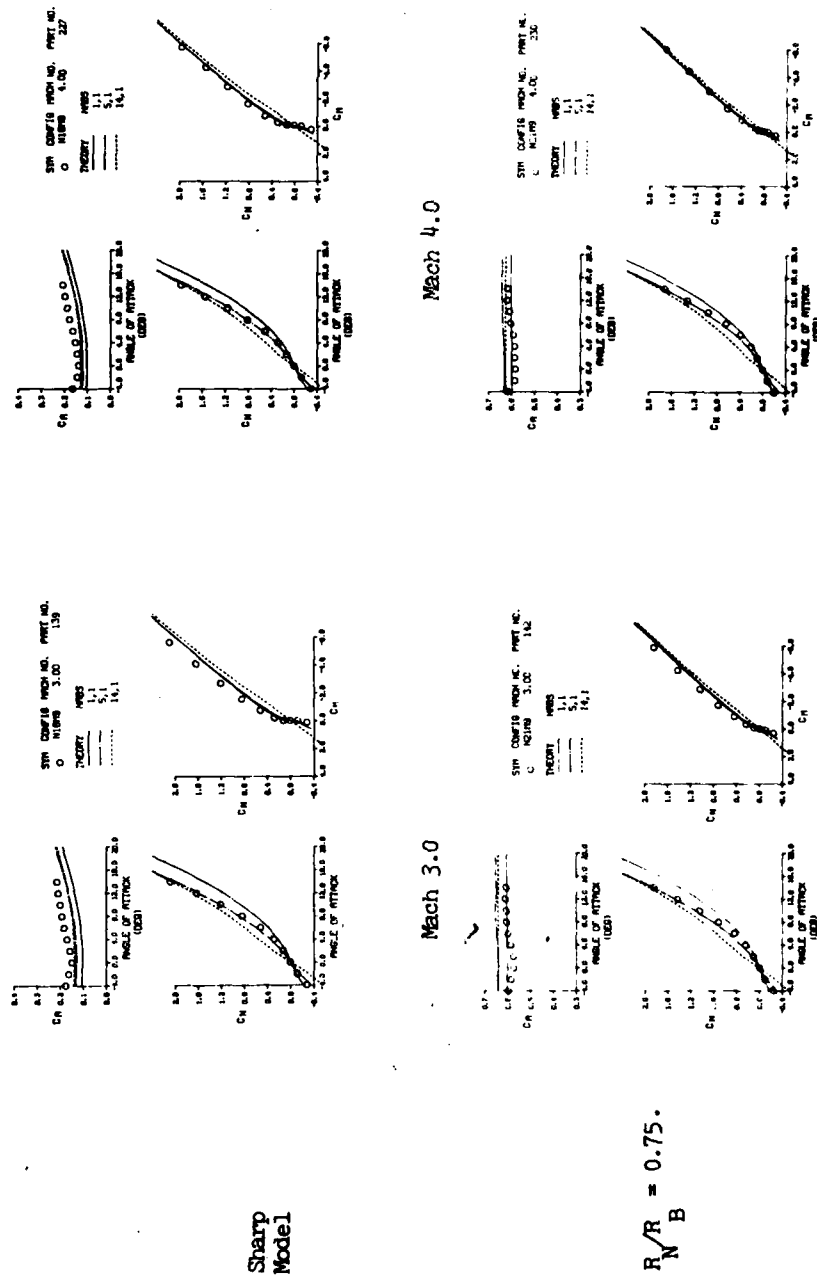
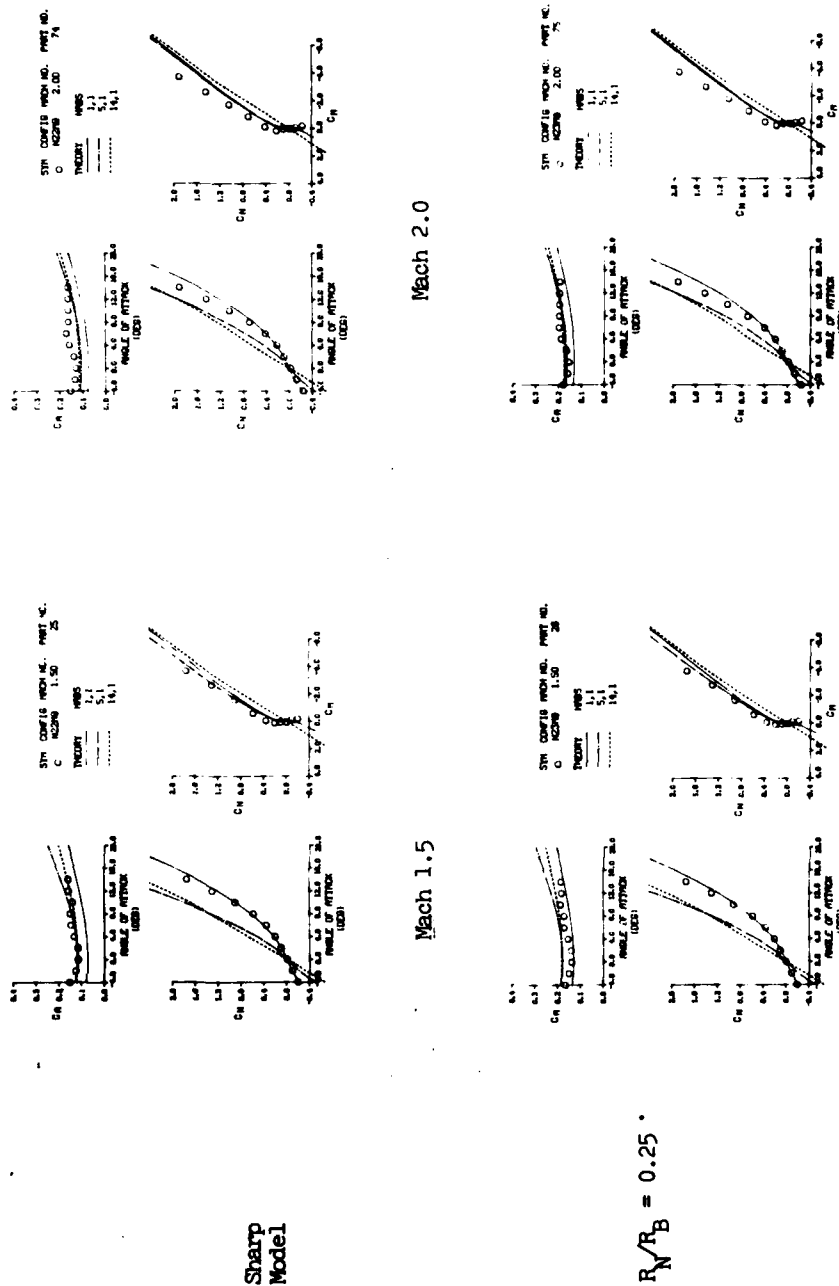


Figure 25. Continued



(f) $R_N/R_B = 0.0$ and 0.75 , $M = 3.0$ and 4.0

Figure 25. Concluded



(a) $R_N/R_B = 0.0$ and 0.25 , $M = 1.5$ and 2.0

Figure 26. HABP Force and Moment Comparisons for the 4.0 Fineness Ratio Nose.

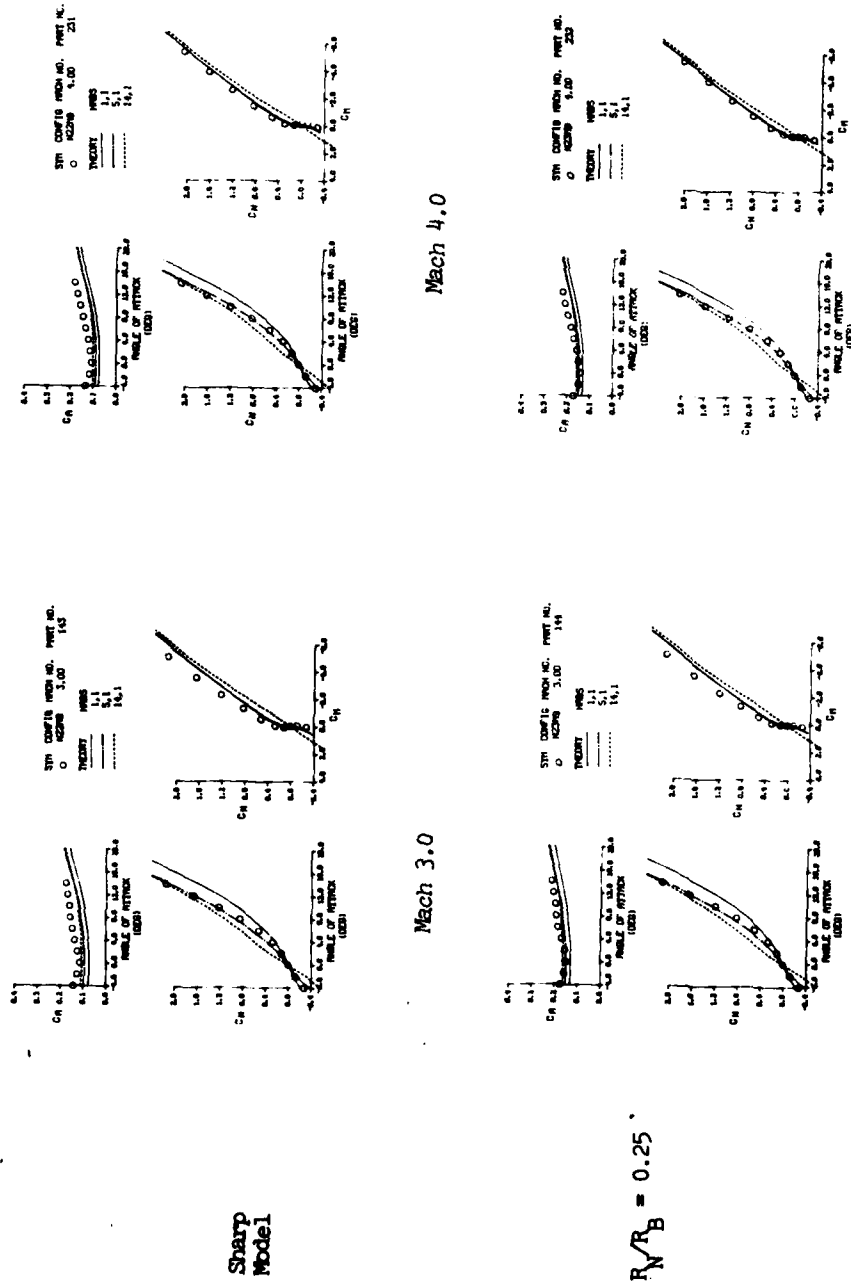


Figure 26. Continued

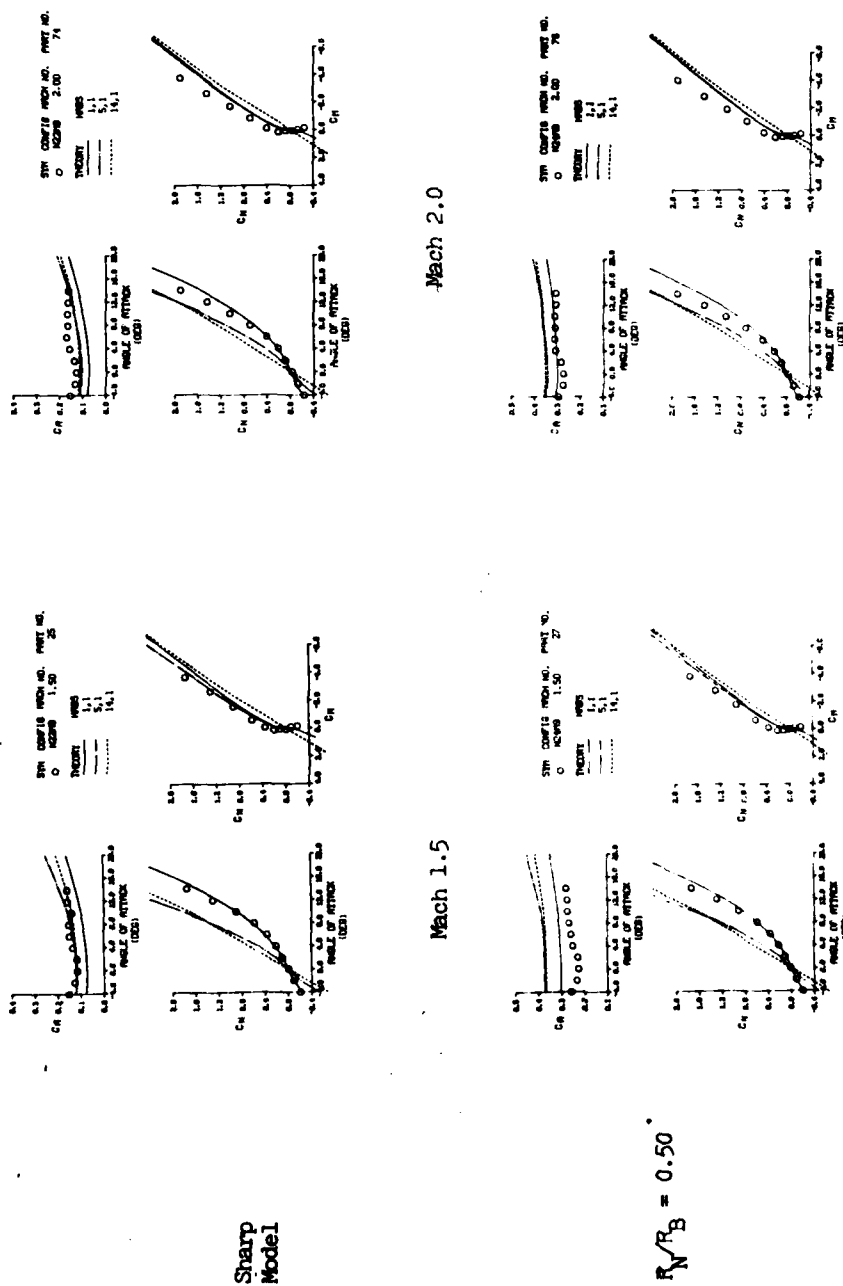


Figure 26. Continued

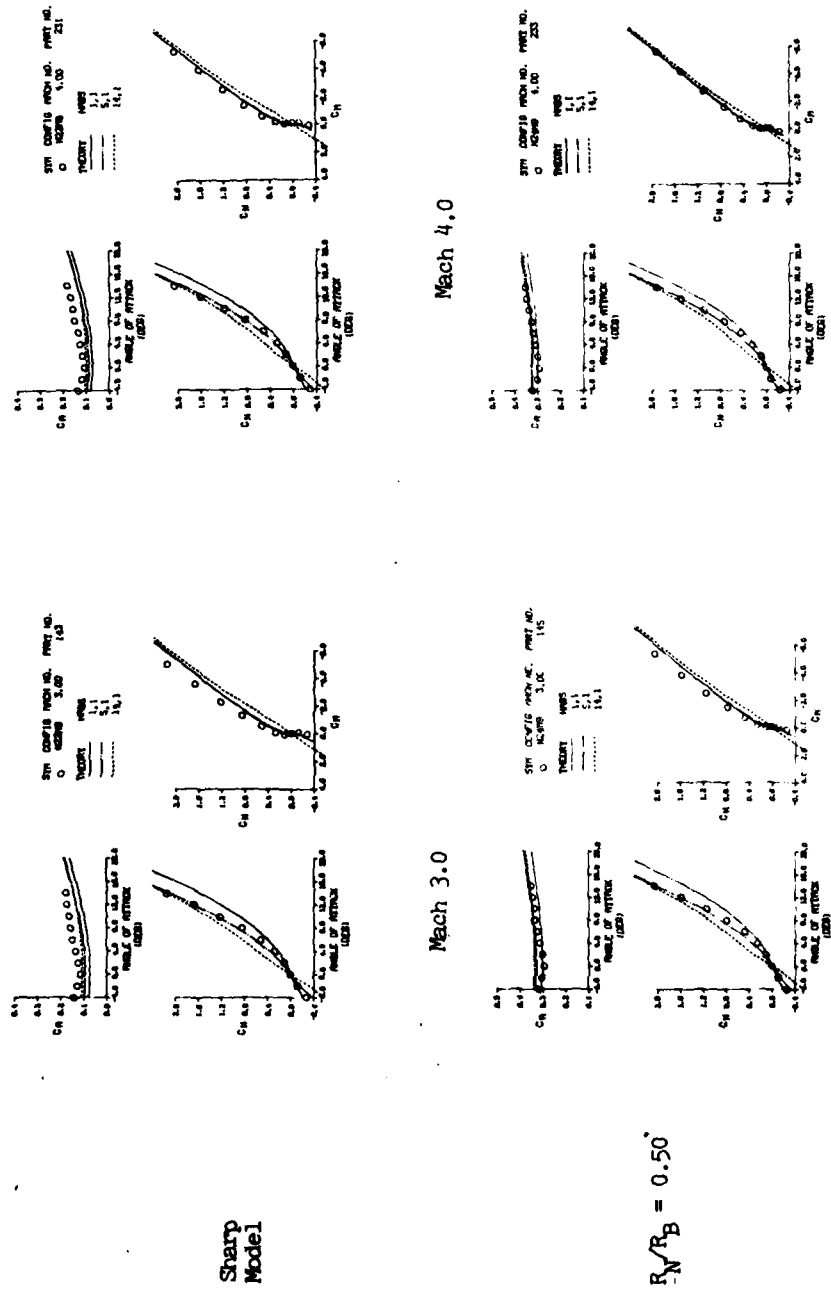
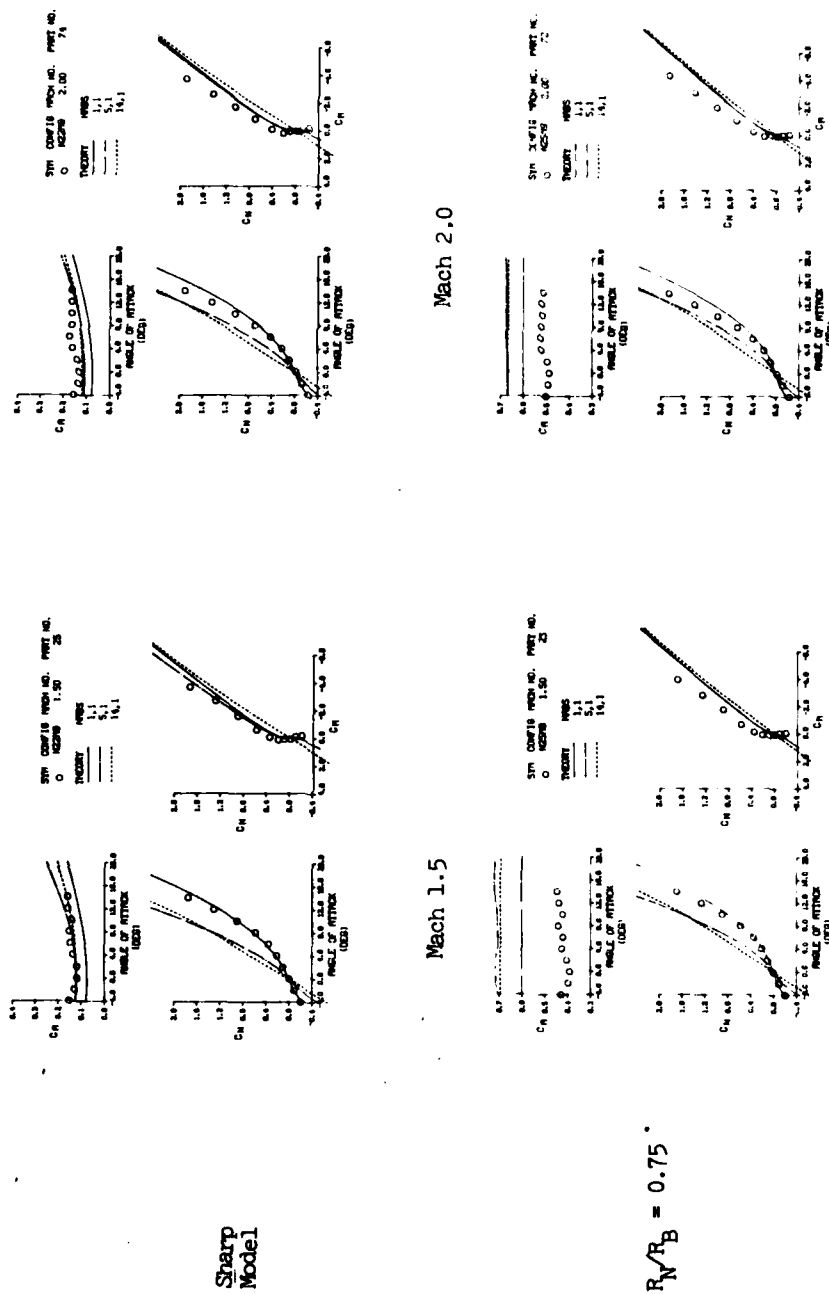
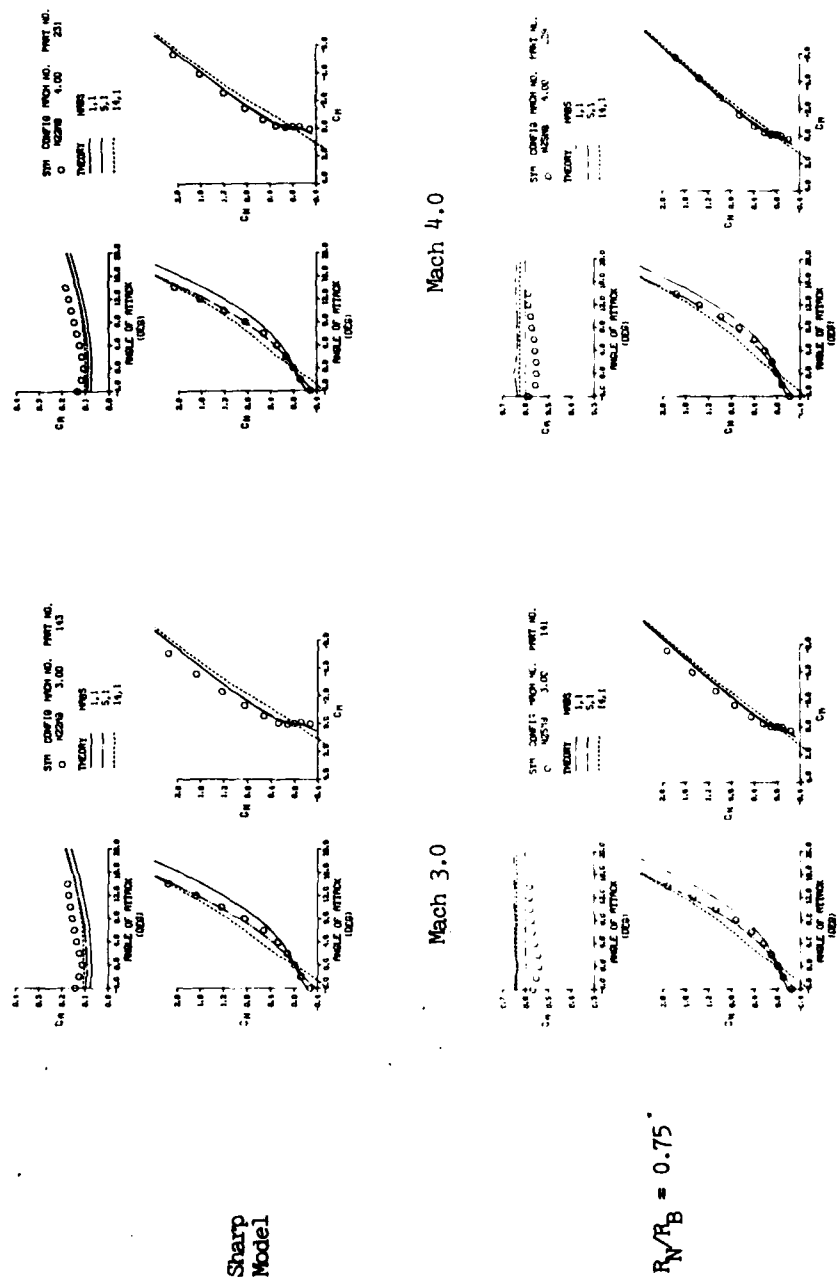


Figure 26. Continued



(e) $R_N/R_B = 0.0$ and 0.75 , $M = 1.5$ and 2.0

Figure 26. Continued



(f) $R_N/R_B = 0.0$ and 0.75 , $M = 3.0$ and 4.0

Figure 26. Concluded

